Department of Physics and Astronomy
Heidelberg University

Bachelor Thesis in Physics
submitted by

Victoria Leona Motsch

born in Wiesbaden (Germany)

2025

The Influence of Boundary Conditions on the Dynamics, Spectrum and Topology of Quantum Kicked Rotor Models

This Bachelor Thesis has been carried out by Victoria Leona Motsch at the
Institute for Theoretical Physics in Heidelberg
under the supervision of
Prof. Dr. Luca Amendola (Universtität Heidelberg)
and
Prof. Dr. Sandro Wimberger (Università di Parma)

Abstract

In this thesis, we study the Quantum Kicked Rotor (QKR) and the Spin-1/2 Double Kicked Rotor (DKRS). We examine the dynamics and Floquet spectra of these models under different boundary conditions (hard wall and periodic) with both infinitesimal and finite kicking duration τ_p.
For the QKR, the dynamics are mostly independent of the boundary conditions. Significant differences arise in the Floquet spectrum of the antiresonant QKR: under periodic boundary conditions discrete quasienergies deviating from the otherwise flat energy bands emerge. We show that the corresponding eigenvectors localize at the edge of the momentum basis.
We investigate the Floquet spectrum and Mean Chiral Displacement (MCD) of the DKRS. In resonance, our results confirm the bulk-edge correspondence, even under finite kicking. Open boundaries lead to the emergence of edge states. A novel insight is that the MCD under resonant conditions is only accurately predicting the number of edge states for open boundary conditions. Under periodic boundary conditions it does not match the theoretical prediction.
We realized two interpretations of the (anti)resonance condition by evolving the system over a free time $\tau - \tau_p$ and τ. The latter leads to spectra that are much more sensitive to the influence of τ_p.
Lastly, we conclude that a finite kick cannot be used to experimentally realize periodic boundary conditions.

In dieser Arbeit wurden zwei Modelle - der Quantum Kicked Rotor (QKR) und der Spin-1/2 Double Kicked Rotor (DKRS) - systematisch untersucht. Für beide Modelle betrachten wir jeweils die Dynamik und das Floquet-Spektrum unter dem Einfluss unterschiedlicher Randbedingungen (RBs). Wir wählen offene (hard wall) und periodische RBs je unter infinitesimaler und endlicher Kickdauer τ_p.
Für den QKR zeigt sich, dass die Dynamik weitgehend unabhängig von den RBs ist. Lediglich im Falle der Antiresonanz entstehen diskrete Punkte im Spektrum, an denen die Quasienergie von der allgemeinen Bandstruktur abweicht. Wir zeigen, dass die zugehörigen Eigenvektoren am Rand der Impulsbasis lokalisiert sind.
Im Falle des DKRS beschränken wir uns auf die Untersuchung des Floquet-Spektrums und des Mean Chiral Displacements (MCD). Im Resonanzfall können wir die Bulk-Edge Korrespondenz bestätigen - sie bleibt auch unter endlicher Kickdauer erhalten. Wir sehen, dass offene Randbedingungen zur Entstehung von Randzuständen führen. Eine neue Erkenntnis ist, dass das MCD nur unter offenen Randbedingungen die richtige Anzahl an Randzuständen vorhersagt. Für periodische Randbedingungen ist das MCD nicht mehr die angemessene experimentelle Messgröße.
Für beide Modelle haben wir je zwei Interpretationen der (Anti-)Resonanzbedingung realisiert: das System wurde je einmal über die Dauer $\tau - \tau_p$ und τ frei entwickelt. In letzterem Falle ist das Spektrum erheblich sensitiver gegenüber der Kickdauer.
Abschließend kommen wir zu dem Schluss, dass die endliche Kickdauer nicht genutzt werden kann, um experimentell periodische RBs zu realisieren.

Contents

1 Introduction

1.1 Motivation

Kicked Rotor Models, beginning with the Quantum Kicked Rotor (QKR), set up the theoretical basis for the exploration of chaotic systems [1–3] and their implications in various fields, such as atom-molecular physics [4]. Together with the Spin-1/2 Double Kicked Rotor (DKRS), which gives rise to rich topological properties [5], the two models provide insights into the dynamics of periodically driven quantum systems and have been used to understand phenomena like quantum chaos, dynamical localization and topological phases [5–7].

The Quantum Kicked Rotor has been studied in detail over the years (see Rev.s [1, 7]). The distinction between periodic and open (hard wall) boundary conditions is relevant especially in the context of experimental realizations. While theoretical works usually use periodic boundary conditions for their calculations, they have not yet been realized experimentally. Therefore, one main goal of this thesis is to understand how these different boundary conditions influence the dynamics and spectral properties of Kicked Rotor Systems. This work compares the influence of the boundary conditions and tries to find an explanation for how differences in the experimental data arise.

In the previous project work (see app. D), we have examined in detail how introducing a finite kicking duration to the Quantum Kicked Rotor gives rise to a "soft wall" in momentum space. This motivated the idea whether one can utilize a finite kicking duration purposely to influence boundary conditions experimentally [6].

The introduction of an internal spin-1/2 degree of freedom in the Double Kicked Rotor Model leads to the emergence of topological phases which entail edge states that are topologically protected against perturbations [5, 8]. The high stability of these edge states makes them promising to use for fault-tolerant quantum computation, as they can withstand local disturbances [5, 9], as well as ultrafast electronics [10] and quantum simulations [11]. It was proposed that the Mean Chiral Displacement (MCD) is a suitable experimental observable to determine topological invariants and topological phases [5]. We test whether this variable still proves to be suitable for those investigations under different boundary conditions.

1.2 Outline

This thesis deals with two Kicked Rotor models: the Quantum Kicked Rotor (QKR) and the Spin-1/2 Double Kicked Rotor (DKRS). Both systems have been subject to extensive studies (see theses [12–14], papers [5, 15] and Rev.s [1, 7], to name a few). The novelty of this work is to understand the influence of different boundary conditions on the dynamics, Floquet spectra, and MCD for the DKRS.

The theoretical background lays the framework for understanding the Kicked Rotor Models. We introduce the physical and mathematical groundwork as well as the numerical realization of the two systems. In order to understand the DKRS model, we then give a background on topological phases.

In chapter three we present our findings on the influence of boundary conditions on the dynamics in form of the probability distribution and the averaged energy as well as on the Floquet spectrum of the QKR. We explore possible reasons for the origin of the differences between the spectra under open and periodic boundary conditions both under infinitesimal and finite kicking duration.

The topic of chapter four is the DKRS. The spin degree of freedom introduces topological edge states and correlated topological phases [5]. We show how the bulk-edge-correspondence holds up when introducing different boundary conditions. To do so, we investigate the Floquet spectra as well as the Mean Chiral Displacement (MCD) that has been proven to be the experimentally accessible quantity for detecting topological invariants [5].

In the end, we give a brief summary and outlook for further theoretical and experimental investigations.

1.3 Abbreviations

- QKR: Quantum Kicked Rotor
- DKRS: Spin-$\frac{1}{2}$ Double Kicked Quantum Rotor
- ORDKRS: On-Resonance Spin-$\frac{1}{2}$ Double Kicked Rotor
- BCs: Boundary Conditions
- OBC: Open Boundary Condition
- PBC: Periodic Boundary Condition
- FFT: Fast Fourier Transformation
- MCD: Mean Chiral Displacement

2 Theoretical Background

2.1 Quantum Kicked Rotor

2.1.1 Hamiltonian & Floquet-Operator

The introduction on the Hamiltonian follows the reviews [1, 7]. In the Kicked Rotor Model, we consider a one-dimensional particle that is confined to a ring in a time-periodic spatial-dependent potential $V(\theta)$. The position can be described by the angle θ (modulo 2π), while its momentum is given by n (usually, one chooses a unit system in which $n \in \mathbb{Z}$ [12]). Notice, that the Hamiltonian is made dimensionless and that we chose $\hbar = 1$ for simplicity. We confine the angle to values $\theta \in [0, 2\pi)$. Therefore, the system shows a modulo 2π-periodicity in position space. The rotor is (time-)periodically kicked with strength k. The kick is made position-dependent by introducing the cosine of the angle. The Hamiltonian in these dimensionless variables for a periodically kicked rotor [7] is given by

$$H'(t') = \frac{n^2}{2} + k\,\cos(\theta) \sum_{m=0}^{\infty} \delta(t' - m\tau) \tag{1}$$

Here, τ is the time between two successive kicks, i.e. τ is the driving or kicking period. During this time, the system undergoes a free evolution.

In general, the momentum in the kinetic part of the Hamiltonian would be $p = n + \beta$ with an integer momentum part $n \in \mathbb{Z}$ and a fractional part β [12], called the quasimomentum. However, we will focus on the simple case with zero quasimomentum $\beta = 0$ for this thesis. The influence of different quasimomenta-distributions has been examined in [13].

The classical kicked rotor can be translated into the Quantum Kicked Rotor (QKR) by replacing position and momentum with their respective quantum operators:

$$\hat{H}' = \frac{\hat{n}^2}{2} + k\,\cos\left(\hat{\theta}\right) \sum_{m=0}^{\infty} \delta(t' - m\tau) \tag{2}$$

$$= \frac{\hat{n}^2}{2} + k\,\cos\left(\hat{\theta}\right) \frac{1}{|\tau|} \sum_{m=0}^{\infty} \delta\left(\frac{t'}{\tau} - m\right) \tag{3}$$

The second equation is the reparametrization of the Dirac-Delta-Distribution. This is necessary in order to be able to later write our Floquet-Operator, see eq. (13). We can rewrite the Hamiltonian in a form where the time is normalized to have measure τ. To do so, eq. (3) has to be multiplied by τ:

$$\hat{H}(t) = \frac{\hat{n}^2}{2}\tau + k\,\cos\left(\hat{\theta}\right) \sum_{m=0}^{\infty} \delta(t - m) \tag{4}$$

Here, t is the time in units of τ and therefore a dimensionless integer number.

Floquet-Operator As the Hamiltonian is time-periodic, $\hat{H}(t) = \hat{H}(t+1)$, solutions to its Schrödinger-Equation (SEQ) can be found using Floquet-Theory [12]: Solutions to the SEQ can be written in the form

$$|\psi(t)\rangle = \sum_{\epsilon} c_\epsilon e^{-i\epsilon t} |\epsilon(t)\rangle \tag{5}$$

with time-periodic eigenstates $|\epsilon(t)\rangle$. The corresponding ϵ is called quasienergy. Because of the structure of $|\psi(t)\rangle$, the quasienergies can only take values $[-\pi, \pi]$.

Using the Dyson-Series, we can compute the one-cycle Floquet-Operator, which gives us the time-evolution operator for one period τ. In units of eq. (4), the Floquet-Operator is given by

$$\hat{U}(M+1, M) = \hat{T}\,\exp\left(-i\int_{M}^{M+1}\hat{H}(t')dt'\right) \tag{6}$$

with $M \in \mathbb{Z}$. Here, $\hat{T}$ is the time-ordering operator.
Momentum $\hat{n}$ and position $\hat{\theta}$ do not commute with each other: $[\hat{\theta}, \hat{n}] = i$. Therefore, the integral has to be performed carefully. One can argue in two different ways.
The first derivation follows the idea of [13]. The ansatz here is to divide up the integration boundaries. For the infinitesimally short kick, we do not need this derivation. Nonetheless, it might be instructive to see to get an understanding for the derivation of the Floquet-Operator in the case of an finite kicking duration. We integrate over $t \in [M, M+1]$. To simplify, we choose $M = 0$ and assume that the kick itself occurs in the interval $[0,\, \delta M]$. We then perform the limit $\lim\limits_{\delta M \to 0}$, which corresponds to the kicking duration being infinitesimally short.

$$\begin{aligned}
\hat{U}(1,0) &= \hat{U}_{(\delta M,\,1]}\cdot\hat{U}_{[0,\,\delta M]} && (7)\\
&= \lim_{\delta M\to 0}\hat{U}_{(\delta M,\,1]}\cdot\hat{U}_{[0,\,\delta M]} && (8)\\
&= \lim_{\delta M\to 0}\hat{T}\,\exp\left(-i\int_{\delta M}^{1}H(t)dt\right)\cdot\lim_{\delta M\to 0}\hat{T}\,\exp\left(-i\int_{0}^{\delta M}H(t)dt\right) && (9)\\
&= \exp\left(-i\frac{\hat{n}^2}{2}\tau\right)\cdot\exp\left(-ik\,\cos\left(\hat{\theta}\right)\right) && (10)
\end{aligned}$$

From the second last to the last step, we used that the time-ordering operator commutes with the limit, as taking the limit does not change the order of events for our case, given that the kick is performed in the interval $[0,\, \delta M]$. Secondly, we used the structure of the Hamiltonian in that step: The second term of $\hat{H}$ only contributes to the integration when the kick acts. For the first factor, the potential term therefore drops out. By taking the limit $\delta M \to 0$, we can justify, that the system effectively does not undergo a free time evolution in the interval $[0, \delta M]$. As a result, we can cancel out the kinetic factor in the second integral. Altogether, this motivates how the free evolution part resulting from the kinetic term of the Hamiltonian and the kicking part of $\hat{U}$ resulting from the potential term of the Hamiltonian factorize in the limit of an infinitesimally short kicking duration.
The second method to motivate the factorization is to use the Baker-Campbell-Hausdorff Formula. It states the following:

$$e^A \cdot e^B = e^{A+B+\frac{1}{2}[A,B]+\frac{1}{12}([A,[A,B]]-[B,[A,B]])+\ldots} \tag{11}$$

Therefore, the exponential would only factorize if the operators commute. As we know, $[\hat{\theta}, \hat{n}] = i$. In general, the commutators do not commute and we would get a finite contribution of the commutator $[\hat{\theta}, \hat{n}]$. Now, we argument the same way as before: For an infinitesimally short kick, the system approximately does not undergo a free time evolution. $[\hat{\theta}, \hat{n}]$ therefore would only contribute for the time of the kick, and as a result only has an infinitesimally small contribution to eq. (11). The other terms are of even higher order and can be neglected as well.
Altogether, we get

$$\begin{aligned}
\hat{U}(1,0) &= \hat{T}\,\exp\left(-i\int_{0}^{1}\hat{H}(t')dt'\right) && (12)\\
&= \exp\left(-i\frac{\hat{n}^2}{2}\tau\right)\cdot\exp\left(-i\,k\,\cos\left(\hat{\theta}\right)\right) && (13)\\
&= \hat{U}_{free}\cdot\hat{U}_{kick} && (14)
\end{aligned}$$

Since the Floquet-States $|\epsilon(t)\rangle$ form an orthonormal basis, the periodicity of the quasienergy-states is passed on to the Floquet-Operator such that the time evolution of m successive kicks can be written as the product of m time evolutions $\hat{U}(m,0) = \hat{U}(1,0)^m$ [12].

2.1.2 Spectrum

The Floquet-Operator $\hat{U}$ can be written in spectral decomposition [12]

$$\hat{U} = \sum_n e^{-i\epsilon_n \tau} |n\rangle \langle n| \tag{15}$$

The spectrum is then given by the phases of the eigenvalues, namely ϵ_n.

2.1.3 Probability Distribution and Energy

We are interested in the probability distribution and averaged energy of the QKR in momentum space, as these give us an indication of what the quasienergy spectrum should look like. One has to take into account that $\hat{U}_{free}$ has a diagonal representation in momentum basis while $\hat{U}_{kick}$ takes diagonal form in position basis. There are two ways to calculate the probability distribution: either one Fourier transforms between the application of the two operators in their respective eigenbasis or one could rewrite the kicking operator $\hat{U}_{kick}$ in the momentum basis (see A.2). Either way, we apply the operators to an initial wavefunction such as $|\psi_0\rangle = \delta(n=0)$. The probability distribution is then obtained by calculating the absolute square of this wavefunction after applying the operators.

Moreover, the energy in dependence of the number of kicks helps us understand whether our system allows energy transport and in which regime the system behaves (i.e. resonant, antiresonant; cf. sections 2.1.4, 2.1.5).

The energy is given by

$$E(t) = \sum_n \frac{n^2}{2} P(n,t) \tag{16}$$

$P(n,t)$ is the probability distribution of the system in momentum space for a number of kicks t. One has to be careful to first calculate the energy at each momentum class n and then sum over all momenta classes.

As the energy fluctuates significantly for most quantum cases, we make use of the energy average over all applied kicks:

$$\bar{E}(t) = \frac{1}{t} \sum_{i=1}^{t} E(i) \tag{17}$$

2.1.4 Quantum Resonance

The kicked rotor (in forms as the QKR and as the DKRS) shows interesting behavior in two regimes - the resonant and the antiresonant regime. Review [1] covers a detailed examination of the resonance condition; the most simple case of quantum resonance is given by selecting a time-evolution period of $\tau = 4\pi$.

In the resonante case, the free evolution operator is identically equal unity, $\hat{U}_{free} = \mathbb{1}$. Therefore, the free evolution does not change the wavefunction describing the system and the Floquet-Operator simplifies to $\hat{U} = e^{-ik\cos(\hat{\theta})}$ [7].

For the resonant regime of the QKR, there is an analytical solution [1]. With that we can calculate the energy and show that the system evolves ballistically: We assume a plane wave as the initial state

$\psi(0,\theta) = \frac{1}{\sqrt{2\pi}} e^{-ip_0\theta}$ and calculate the energy as follows

$$E(t) = \langle \psi(t,\theta)| - \frac{1}{2}\frac{\partial^2}{\partial^2\theta} |\psi(t,\theta)\rangle = \frac{k^2\, t^2}{4} + \frac{n_0^2}{2}, \tag{18}$$

see [1, 12, 13]. The complete derivation is given in appendix A.1.
We see, that in the resonant regime, the energy is growing quadratically in time - the system evolves ballistically. The momentum distribution of the system spreads in momentum space. States do not localize. From this follows that the quasienergy spectrum is expected to be continuous.

2.1.5 Quantum Antiresonance

As written in [1], the antiresonant case is an exceptional case, as it is the only case where the plane wave solution to the Schrödinger equation of the QKR is 2π-periodic. The antiresonant regime is given by $\tau = 2\pi$. After an even number of kicks, the system returns to the preceding wavefunction - two successive kicks compensate each other: $\hat{U}_{free} = e^{-i\frac{\hat{n}^2}{2}\cdot 2\pi n}$ alternates between ± 1 [7].
As argued in [1], the quasienergy spectrum in the antiresonant case has completely flat energy bands with only two energy values: $\epsilon = 0, \pm\pi$. The reason for this lies within the specific cosine-form of the potential [1]. The flat energy bands agree with the momentum distribution staying localized as then the energy transport is suppressed. Any deviation from the flat structure should give rise to possible energy transport that would disturb the expected saturation of the averaged energy $\bar{E}(t)$.

2.2 Double Kicked Rotor with Spin

The Spin-1/2 Double Kicked Rotor is an experimentally realizable model [16, 17] that combines the quantum dynamics in periodically driven systems like the QKR with interesting topological properties, that arise by the introduction of the internal spin degree of freedom [5, 18]. As such, the DKRS is interesting for applications in quantum computation [5, 9], quantum simulations [11] and ultrafast electronics [10].
We follow the definition of the Spin-1/2 Double Kicked Rotor given in [5]. The Double Kicked Rotor with internal Spin (DKRS) is an extended version of the QKR, where a second kick and an internal spin-1/2 $S = \pm\frac{1}{2}$ is introduced. As in the QKR, the system is kicked periodically, now with two kicking strengths k_1 and k_2. The kick can be infinitesimally short or of a finite kicking duration τ_{p_1,p_2}. In between the two successive kicks, the system undergoes a free time evolution over $\tau_{1,2}$. In accordance with [5], the Hamiltonian can be written in a general form as

$$\hat{H} = \frac{\hat{n}^2 \otimes \mathbb{1}}{2} + k_1 \cos\left(\hat{\theta}\right) \otimes 2\hat{S}_x \cdot \sum_{n=0}^{\infty} \delta(t - n\tau_1) + k_2 \cos\left(\hat{\theta} + \beta\right) \otimes 2\hat{S}_y \cdot \sum_{n=0}^{\infty} \delta(t - n\tau_2) \tag{19}$$

$\hat{\theta}$ has the same meaning here as for the QKR. β is the phase shift between the two kicking potentials. For the sake of simplicity, the value of the phase shift is set to $\beta = \frac{\pi}{2}$ for all calculations. The Hamiltonian then simplifies to

$$\hat{H} = \frac{\hat{n}^2 \otimes \mathbb{1}}{2} + k_1 \cos\left(\hat{\theta}\right) \otimes 2\hat{S}_x \cdot \sum_{n=0}^{\infty} \delta(t - 2n\tau_1) + k_2 \sin\left(\hat{\theta}\right) \otimes 2\hat{S}_y \cdot \sum_{n=0}^{\infty} \delta(t - (2n+1)\tau_2) \tag{20}$$

After reparametrization and integration as for the QKR, eq. (4), sec. 2.1.1, we obtain the Floquet operator for the DKRS

$$\hat{U}_{DKRS} = e^{-i\frac{\hat{n}^2}{2}\tau_2}\, e^{-ik_2 \sin\left(\hat{\theta}\right)\sigma_y}\, e^{-i\frac{\hat{n}^2}{2}\tau_1}\, e^{-ik_1 \cos\left(\hat{\theta}\right)\sigma_x} \tag{21}$$

with $\sigma_{x,y,z}$ the Pauli matrices acting on the internal spin space of the rotor.
Following [5], we choose $\tau_1 = \tau_2$. This simplifies the investigation of the spectrum and MCD significantly, as we can compare our results to the known cases of [5] and the QKR. We say that the DKRS is in resonance for $\tau_1 = \tau_2 = 4\pi$ and that it is in antiresonance for $\tau_1 = \tau_2 = 2\pi$.

On Resonance Double Kicked Rotor with Spin (ORDKRS) One can also choose the rotor to be under resonance condition at all times: $\tau_1 = 4\pi = \tau_2$. Then, the Floquet operator reduces to [5]

$$\hat{U}_{ORDKRS} = e^{-ik_2 \sin(\hat{\theta})\, \sigma_y}\, e^{-ik_1 \cos(\hat{\theta})\, \sigma_x} \tag{22}$$

For the ORDKRS, ref. [5] offers a thorough examination of the topology and an in-depth discussion of the bulk-edge correspondence. We later confirm the validity of this in our parameter regime and with our boundary conditions.
For our studies of the DKRS, we need to introduce some concepts of topology. Paper [15] offers a comprehensive overview of the topological phenomena in quantum walks. Ref.s [13] and [14] may be consulted for another introduction of the topological properties of the DKRS, especially in regards to the study of the topological winding number. A brief presentation of the most important concepts of topology and topological phase transitions for our examination is found in sec. 2.5.

2.3 Boundary Conditions

In general, we distinguish between open and periodic boundary conditions. Moreover, in a previous project work, we have studied the effect of a finite pulse duration over which the potential $V(\hat{\theta})$ is switched on. This introduces a "soft wall" in momentum space [6]. To shortly summarize the main idea: the finite kicking duration has the effect, that the plane wave solution to the Schrödinger equation gets reflected. This effect is purely classical. However, the plane wave can only cross the "soft wall"-barrier in the quantum-mechanical picture due to tunneling. The exact positions of the soft walls in momentum space have been determined in the project work. A further explanation of the used methods and their results is given in app. D.

2.3.1 Open and Periodic Boundary Conditions

Classically, **open boundary conditions (OBCs)** mean that a system underlies either Dirichlet- or Neumann-Boundary Conditions. For Dirichlet BCs, the solution to the wavefunction at the boundary is known; for Neumann BCs, the gradient or derivative of the solution at the boundary is known.
In our case, we use open boundary conditions as commonly used in condensed matter physics. Here, OBCs mean that our system may only occupy a limited number of momenta classes, e.g. $n \in [-n_C, n_C]$, $n \in \mathbb{Z}$. At the edge of this basis $\pm n$, the system has a "hard cutoff".
This is easily implemented by limiting the size of the array for the momenta n. It is important to consider whether the system should see the boundary or not when investigating the spectrum and energy. To investigate the bulk of the system, one would choose a large basis to minimize the influence of the borders of the basis. For examining the influence of the hard cutoff of the basis, one would have to choose a rather short basis, such that the system effectively interacts with the boundary.
Periodic boundary conditions (PBCs) mean that after a given number N, the momentum returns to the starting value: $|n\rangle = |n + N\rangle$ [5]. Mathematically, the system is mapped onto a torus [13]. PBCs are often used in theoretical calculations as they allow the usage of e.g. Fourier transformations, and most often lead to additional symmetries within the system.
For the Hamiltonian of a system, we know how to realize periodic boundary conditions. To do so, we

add a coupling between the boundary elements. In our case, the Hamiltonian will always have either diagonal or band-diagonal form with one off-diagonal at each side. For that matrix representation of a Hamiltonian, we can implement the PBCs easily by adding the coupling terms to the corner-elements on the upper right and lower left as seen in Fig. 1. The off-diagonal elements on the right and left of the diagonal are complex conjugates of each other. Therefore, the added corner-elements also differ only by complex conjugation.

It is important to point out that we can only implement the PBCs by this trick on the basis of the Hamiltonian. Only the Hamiltonian has the (band)-diagonal structure and hermitian form. The Floquet-Operator as the matrix exponential of the Hamiltonian has a much more complex form and is not hermitian but unitary. Thus, for our later calculations we always write the Hamiltonians in their matrix representation, and implement the boundary conditions in that representation before we then obtain the Floquet-Operator out of the matrix exponential.

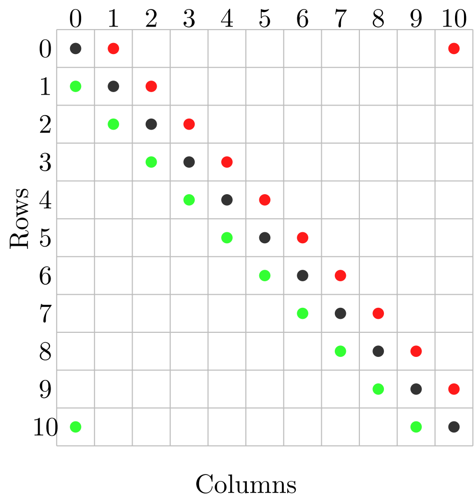

Figure 1: Schematic representation of the implementation of periodic boundary conditions for a band-diagonal matrix. We use two Hamiltonians - the free-time-evolution Hamiltonian $H_{free} = e^{-i\frac{n^2}{2}\tau}$ which is already diagonal in n-basis and therefore does not need to be adjusted for periodic boundary conditions. The second Hamiltonian we use is $H_{kick} = \frac{e^{i\theta}+e^{-i\theta}}{2}$ which only has entries on the first adjacent diagonal in n-basis. The derivation of this form is given in app. A.2.

2.3.2 Soft Wall by Finite Kicking Duration

QKR In a preceding project work, I studied the effect of a finite pulse duration, during which the potential acts on the rotor, on the dynamics of the QKR. For this case, the Hamiltonian is rewritten into the form

$$\hat{H}(t') = \frac{\hat{n}^2}{2} + k \cdot \cos\left(\hat{\theta}\right) \sum_{m=0}^{\infty} \delta(t' - m\tau) * rect\left(\frac{t'}{\tau_p}\right) \tag{23}$$

$$\hat{H}'(t) = \frac{\hat{n}^2}{2}\tau + k \cdot \cos\left(\hat{\theta}\right) \sum_{m=0}^{\infty} \delta(t - m) * rect\left(\frac{t}{\tau_p}\right) \tag{24}$$

We always assume the potential term to have a rectangular form, i.e. as the potential is "switched on" it directly acts on the rotor and is then switched off after a time τ_p and directly stops acting on it. It was shown that the specific shape of the pulse does not significantly affect the numerical results [6, 12].

Numerically, we implement this by generating a sequence of h δ-kicks with strength $\frac{1}{h} \cdot k$ each followed by a time evolution over $\frac{1}{h} \cdot \tau_p$ [2]. It is important to take into account that the kicking strength k and the duration of the free time evolution in between the h δ-kicks needs to be adjusted accordingly by multiplying with $\frac{1}{h}$. After the last application of the h δ-kicks, the system undergoes a free time evolution over $\tau - \tau_p$. The one-cycle Floquet-operator is given by

$$\hat{U}_{QKR,\,finite}(t+1,t) = e^{-i\frac{\hat{n}^2}{2}(\tau-\tau_p)} \cdot \prod_{a=1}^{h} e^{-i\frac{\hat{n}^2}{2}\frac{\tau_p}{h}} \cdot e^{-i\frac{k}{h}\cos(\hat{\theta})} \tag{25}$$

The parameter h, denoting the number of δ-kicks in which the finite kick is divided, is chosen based on numerical evidence. N. Bolik showed in a recent paper [19], that for an experimental realization with $\tau_p = 0.005$ and a basis $n_{max} \leq 100$, $h = 10$ is a sufficient choice to reach convergence while reducing computation time. In our regime, we have to use larger kicking durations up to $\tau_p = 10^{-2}$. We checked for some general cases, that with the choice of $h = 10$ we still achieve convergence in our parameter regime.

DKRS For the DKRS, the finite kicking duration can be implemented completely analogous to the QKR. It has to be taken into account, that we have two free time evolutions τ_1 and τ_2, two numbers of spacing for the δ-kicks h_1 and h_2 and two different kicking durations $\tau_{p,1}$ and $\tau_{p,2}$. As pointed out above, h has to be chosen under consideration of the kicking lengths and the basis length. For our purpose, $h_1 = h_2 = 10$ is sufficient. Moreover, we focus on the case $\tau_{p,1} = \tau_{p,2}$ for simplification. The Floquet operator for the DKRS under finite kicking duration is then given as the product of two Floquet operators of above form eq. (25) with adjusted free time evolutions τ_i and kicking durations $\tau_{p,i}$:

$$\hat{U}_{DKRS,\,finite}(t+T,t) = \hat{U}_{finite}(t+(\tau_1+\tau_{p,1}),t) \cdot \hat{U}_{finite}(t+(\tau_2+\tau_{p,2}),t) \tag{26}$$

$$= e^{-i\frac{\hat{n}^2}{2}(\tau_1-\tau_{p,1})} \cdot \prod_{a=1}^{h_1} e^{-i\frac{\hat{n}^2}{2}\frac{\tau_{p,1}}{h_1}} \cdot e^{-i\frac{k}{h_1}cos(\hat{\theta})} \cdot e^{-i\frac{\hat{n}^2}{2}(\tau_2-\tau_{p,2})} \cdot \prod_{b=1}^{h_2} e^{-i\frac{\hat{n}^2}{2}\frac{\tau_{p,2}}{h_2}} \cdot e^{-i\frac{k}{h_2}cos(\hat{\theta})} \tag{27}$$

with $T = \tau_1 + \tau_2$. We say that the DKRS is in resonance for $\tau_1 = \tau_2 = 4\pi$ and in antiresonance for $\tau_1 = \tau_2 = 2\pi$, see sec.s 2.1.4 and 2.1.5.

Position of the "Soft Walls" In the project work we derived different methods to estimate the momenta classes n_L at which the "soft walls" arose. Five different methods were used - the three with the most reliable outcomes gave the following results:

Table 1: Limiting momentum class n_L for different pulse durations τ_p

	τ_p			
Method	10^{-1}	10^{-2}	10^{-3}	10^{-4}
1	5	16	48	150
3	5	18	59	193
4	6	19	59	184

The differences in n_L arise from the fact that the threshold is not a single state n but rather a region in momentum space since the finite kicking duration introduces an effective filter in momentum space as described in [6]. Moreover, the n_L were determined via different methods that use different thresholds to determine the arise of the "soft wall", see app. D, which further leads to different values of n_L.
The limiting momenta classes n_L were determined only for the resonant regime $\tau = 4\pi$. For the antiresonant case, however, we do not need any limiting values of n_L, since the probability distribution in momentum space is highly localized nonetheless. Further details on the methods used for the calculation of n_L can be found in the appendix D.

In addition to open and periodic boundary conditions, we also want to explore the influence of a finite pulse duration on the dynamics of the QKR. It represents an intermediate regime in which we have neither a hard cutoff as in OBCs nor the coupling of boundary elements as in PBCs, but rather a soft reflecting wall. Implementing the finite kicking duration τ_p we then have to take into account that the basis length has to be chosen to be sufficiently larger than the corresponding n_L. If we do not consider this, the influence of the "soft wall reflection" might prevail the dynamics. For $\tau_p = 10^{-2}$ e.g., the basis length should not be chosen to be smaller than $n = 30$.

2.4 Numerical Methods for Determining the Floquet-Spectra

A main objective of this work is to examine the differences in the spectra of the Floquet operator under varying boundary conditions. Apart from the simplest case at quantum resonance, the spectrum will be determined numerically. Therefore, we will first explain the matrix representations and numerical tools employed.

Diagonalization & Calculation of the Eigenvalues The Floquet-Operator of the QKR $\hat{U} = e^{-i\frac{\hat{n}^2}{2}} e^{-ik\,cos(\hat{\theta})}$ does not have diagonal form: the first factor is diagonal in momentum basis $|n\rangle$, while the second factor is diagonal in position space $|\theta\rangle$. In order to calculate the eigenvalues of the Floquet operator, we rewrite it in a way that it is block-diagonal in momentum space. There are two ways to do this. One way is to rewrite the kicking part $\hat{U}_{kick}$ in terms of Bessel functions. Calculation shows that

$$\langle m|\, e^{-ik\,cos(\hat{\theta})}\, |n\rangle = (-i)^{m-n} J_{(m-n)}(k) \tag{28}$$

A thorough derivation can be found in [1, 7, 12].
The other way is to rewrite the cosine as $\cos\hat{\theta} = \frac{e^{i\hat{\theta}}+e^{-i\hat{\theta}}}{2}$ and to Fourier-transform between position and momentum space to determine the action of the operator on a momentum state $|n\rangle$ [5]:

$$\cos\hat{\theta} = \frac{1}{2}\sum_n |n\rangle\langle n+1| + |n+1\rangle\langle n|\,, \tag{29}$$

see A.2.
Either way, we get a block-diagonal form for the operator $\hat{U}_{kick}$ in momentum space. The advantage of representing the matrix in momentum space is that we get the eigenvectors from the diagonalization in momentum space as well. As we are later interested in the momentum space distribution of the eigenvectors, it is beneficial to proceed with this representation. For this thesis, we use the second method and rewrite the *cosine*-term in momentum space. The benefit is that we only have one off-diagonal right and left to the diagonal in the matrix. It is therefore easier to implement the periodic boundary conditions as explained in 2.3.1.
We then use the Python numpy-tool *np.linalg.eig(M)* (documentation see ref. [20]) to determine the eigenvalues of the matrix representation of $\hat{U}$. This diagonalization routine works for every square matrix independent of its form. This is crucial, as our Floquet operator is generally not hermitian, but unitary. Our **diagonalization routine** is the following:

- We define the Hamiltonians H_{free} and H_{kick} corresponding to $\hat{U}_{free}$ and $\hat{U}_{kick}$ and write them down in momentum space. If necessary, we implement PBCs by adding the corner-elements of the matrix on the level of the Hamiltonian. This is done "by hand".
- We then get the Floquet operator by using the matrix exponential $M_H = exp(-i \cdot H)$ where we plug in the representation in momentum space for H. We use the Python scipy-tool *expm* (documentation see ref. [21]) for this.

A note on *expm*: This tool uses an algorithm that approximates the matrix exponential. It is important that the matrix exponential is used here and that we do not just exponentiate the entries of the matrix, as our matrix does not possess diagonal form.

- We then multiply the matrix exponentials to obtain the full Floquet operator of the system.
- Using *np.linalg.eig(M)* (see ref. [20]), we calculate the eigenvalues and eigenvectors of the complete Floquet operator.
- We get the quasienergies ϵ_n as the phases of the eigenvalues of $\hat{U} = \sum_n e^{-i\epsilon_n \tau} |n\rangle \langle n|$, remembering the sign and τ in the exponential.
- For the graphical representation, we plot the quasienergies against the index. Note that the index is an arbitrary index associated with the eigenvalue. The index does not have any intrinsic physical meaning or connection to the momenta classes n. By convention, we sort the eigenvalues in ascending order.

For the DKRS, we can use the same diagonalization routine. The important difference is that the DKRS has an intrinsic spin degree of freedom. This means that the whole system has to be connected with the Hilbert space of the Spin-1/2, $\mathscr{H}_S \cong \mathbb{C}^2$. Practically this means that our system that has dimension $2n$ for the QKR now has dimension $2 \times 2n$ and all matrices have to be tensor-multiplied with spin matrices σ_i. Ref. [5], which is our main reference paper, uses a momentum basis $n \in [0, n]$ and not $n \in [-n, n]$. We use the latter for our calculations.

FFT-Method An alternative method would be to split the Floquet operator into the free time evolution $\hat{U}_{free}$ and the kick operator $\hat{U}_{kick}$ and to represent these parts diagonally in their base. In order to calculate the dynamics or the spectrum, the partial operators are then applied to the normalized unit vectors of the momentum basis ($|n_i\rangle = (0, ..., 0, 1, 0, ..., 0)$ where the 1 is at the i-th index). Between the application of the partial operators, the state vector to which the operators are applied is then Fourier transformed. The calculations in the project work were carried out using this method. The disadvantage of this method, though, is that we do not know the exact form of the Hamiltonian. If we want to implement periodic boundary conditions, the easiest way is to manipulate the matrix representation of the Hamiltonian operator as explained in section 2.3.1. This is the great advantage of writing the Floquet operator in one basis and the reason why we have chosen this method of the diagonal form instead of the Fourier transform method for the calculations.
However, what we found out during our studies was that when implementing the finite kicking duration, the FFT-Method lead to the exact same results as the combination of a finite kicking duration and periodic boundary conditions. To understand this, one has to understand the theory behind FFTs. Using a FFT on a discrete array results is a Discrete Fourier Transformation (DFT) (see [22]). For a DFT, it can be shown from the definition that it is always periodic

$$\mathcal{F}(x_{n+N}) = X_{k+N} = \sum_{n=0}^{N-1} x_n e^{-\frac{i2\pi}{N}(k+N)n} = \sum_{n=0}^{N-1} x_n e^{-\frac{i2\pi}{N}kn} e^{-i2\pi n} = \sum_{n=0}^{N-1} x_n e^{-\frac{i2\pi}{N}kn} = X_k = \mathcal{F}(x_n) \quad (30)$$

Therefore, by using the FFT-method, we indirectly assume periodic boundary conditions. As a result, the spectra and dynamics display equal behavior.

Finite Kicking Duration The finite kicking duration is used to mimic a "soft wall" as a boundary condition. Numerically, we mimic the finite kick by splitting it up into 10 δ-kicks, as explained in 2.3.2. We then use the same diagonalization routine as for the infinitesimal case. The only difference is, that we write a loop that repeats the application of the kick and the short free time evolution over $\frac{\tau_p}{h}$ h times and only then we multiply this result with the time evolution operator over the long free time evolution τ.

2.5 Topology and Topological Phase Transitions

A thorough general analysis of topological phenomena in quantum walks can be found in [15]. The thesis [13] as well as the paper by Zhou & Gong [5] explain the most important topological concepts for the DKRS.

Topology, in general, studies how systems behave under continuous deformations. Continuous means that the transformation does not allow "gluing" or "cutting" as well as "opening" or "closing holes". Two objects belong to the same topological class if they can be transformed into each other by a continuous deformation. Typically, the number characterizing the topological class is the number of holes in the system. In our context, the objects that are subject to topological analysis are gapped Hamiltonians. Instead of the number of holes, we define topological invariants based on the Hamiltonian and symmetries in the analyzed system. [23]

The transformations under consideration are required to satisfy the following criteria: 1. continuity; 2. preservation of the energy gap; 3. conservation of symmetry [24]. Assuming the transformations are continuous and symmetry-conserving, the corresponding topological invariant only changes if the energy gap closes [25]. For our further considerations, we assume that a closing energy gap is the only way to get a topological phase transition.

2.5.1 Gapped Hamiltonians

A gapped Hamiltonian is characterized by an energy gap in its spectrum, meaning e.g. between its ground state and the first excited state is a finite gap - it takes finite energy to excite the system. The Hamiltonian of the system does not have eigenvalues in a finite interval around the ground-state energy [13, 23].

Two Hamiltonians belong to the same topological class if they can be deformed into each other without closing this gap. The type of this deformation classifies the topological invariant [24]. A more thorough introduction to gapped Hamiltonians can be found in [13].

Chiral Symmetric Operators The symmetry of interest for our system is the chiral symmetry, also called sublattice symmetry in the context of solid state physics [15]. A Hamiltonian is chiral symmetric when

$$\hat{\Gamma}^{\dagger}\hat{H}\,\hat{\Gamma} = -\hat{H} \tag{31}$$

where we choose $\hat{\Gamma} = \mathbb{1} \otimes \hat{\sigma_z}$, following the convention in [5, 13, 15]. $\hat{\Gamma}$ has to be unitary and Hermitian, $\hat{\Gamma}^{\dagger} = \hat{\Gamma}$: $\hat{\Gamma}^{\dagger}\hat{\Gamma} = \hat{\Gamma}^2 = 1$ [25]. Chiral symmetry arises from a combination of particle-hole and time-reversal symmetry [24]. As shown in [13] and [15], chiral symmetry is directly linked to the energy spectrum being symmetric around zero. Each eigenvalue has a chiral symmetric partner with the same energy but opposite sign. Thus, the zero energy eigenstate plays a special role, as it is its own chiral symmetric partner - zero energy eigenstates are not only eigenstates of the Hamiltonian but for the operator $\hat{\Gamma}$ as well. Reference [13] shows that for the DKRS, π energy states are their own chiral symmetric partners as well.

2.5.2 Chiral Symmetric Floquet-Operators

The Floquet operator of the ORDKRS used so far (eq. (22)) is not chirally symmetric [5]. In order to define topological invariants, we have to transform $\hat{U}$ into two chiral symmetric time frames [5] that lead to

$$\hat{U}_{1,\,ORDKRS} = e^{-i\frac{k_1}{2}cos(\hat{\theta})\sigma_x}\, e^{-ik_2 sin(\hat{\theta})\sigma_y}\, e^{-i\frac{k_1}{2}cos(\hat{\theta})\sigma_x} \tag{32}$$

$$\hat{U}_{2,\,ORDKRS} = e^{-i\frac{k_2}{2}sin(\hat{\theta})\sigma_y}\, e^{-ik_1 cos(\hat{\theta})\sigma_x}\, e^{-i\frac{k_2}{2}sin(\hat{\theta})\sigma_y}. \tag{33}$$

Ref. [13] proves that these Floquet operator are the only chiral symmetric formulations of $\hat{U}_{ORDKRS}$. Moreover, the three Floquet operators are related via a unitary transformation such that they all share the same quasienergy spectrum. This has been tested also numerically in the course of this thesis, see app. C.1.

For the DKRS we can define the Floquet operators in the chiral symmetric time frames analogously, following the structure of the definition in [5]:

$$\begin{aligned}
\hat{U}_{1,DKRS} &= e^{-i\frac{\hat{n}^2}{2}\tau_1}\, e^{-i\frac{k_1}{2}\,cos(\hat{\theta})\sigma_x}\, e^{-i\frac{\hat{n}^2}{2}\tau_2}\, e^{-ik_2 sin(\hat{\theta})\sigma_y}\, e^{-i\frac{\hat{n}^2}{2}\tau_1}\, e^{-i\frac{k_1}{2}\,cos(\hat{\theta})\sigma_x} \\
&= \hat{U}_{\tau_1}\hat{U}_{k_1/2}\cdot\hat{U}_{\tau_2}\hat{U}_{k_2}\cdot\hat{U}_{\tau_1}\hat{U}_{k_1/2} \\
\hat{U}_{2,DKRS} &= e^{-i\frac{\hat{n}^2}{2}\tau_2}\, e^{-i\frac{k_2}{2}\,sin(\hat{\theta})\sigma_y}\, e^{-i\frac{\hat{n}^2}{2}\tau_1}\, e^{-ik_1 cos(\hat{\theta})\sigma_x}\, e^{-i\frac{\hat{n}^2}{2}\tau_2}\, e^{-i\frac{k_2}{2}\,sin(\hat{\theta})\sigma_y} \\
&= \hat{U}_{\tau_2}\hat{U}_{k_2/2}\cdot\hat{U}_{\tau_1}\hat{U}_{k_1}\cdot\hat{U}_{\tau_2}\hat{U}_{k_2/2}.
\end{aligned}$$

2.5.3 Energy Spectrum of the ORDKRS

For the ORDKRS, one can analytically derive the bulk quasienergy spectrum as shown in [5] and [13]. First, one has to rewrite the chiral symmetric Floquet operators

$$\hat{U}_l = \sum_{\theta} e^{-iE(\theta)\,\vec{n}_l\cdot\vec{\sigma}} \tag{34}$$

Then, one has to use the matrix representation of $\hat{U}_1$ and $\hat{U}_2$ as well as the identity

$$e^{-i\varphi\,\vec{n}\cdot\vec{\sigma}} = \cos(\varphi)\mathbb{1} - i\,\sin(\varphi)\,\vec{n}\cdot\vec{\sigma} \tag{35}$$

with $\varphi = E(\theta)$.

This leads to the quasienergy spectrum

$$E(\theta) = \arccos[\cos(\kappa_1)\cdot\cos(\kappa_2)] \tag{36}$$

where we introduced $\kappa_1 = k_1\,\cos(\theta)$ and $\kappa_2 = k_2\,\sin(\theta)$. The κ_l carry the dependence on θ. From this also follows an expression for the vectors $\vec{n}_1$, $\vec{n}_2$:

$$n_{1,x} = \frac{sin(\kappa_1)\cos(\kappa_2)}{\sin(E)} \qquad\qquad n_{1,y} = \frac{\sin(\kappa_2)}{\sin(E)} \tag{37}$$

$$n_{2,x} = \frac{\sin(\kappa_1)}{\sin(E)} \qquad\qquad n_{2,y} = \frac{\sin(\kappa_2)\cos(\kappa_1)}{\sin(E)}. \tag{38}$$

A thorough derivation of these explicit forms for $E(\theta)$, $\vec{n}_l$ is given in the appendix of [13].

As stated above, we assume that the topological invariant only changes if the energy gap closes. From the explicit expression for $E(\theta)$, we can read off the criterion for a closing in the energy gap:

$$E(\theta) \stackrel{!}{=} 0, \pm\pi \quad\Longrightarrow\quad \cos(\kappa_1)\cdot\cos(\kappa_2) \stackrel{!}{=} \pm 1 \tag{39}$$

$E(\theta) = 0$ corresponds to $\cos(\kappa_1)\cdot\cos(\kappa_2) = 1$ and $E(\theta) = \pm\pi$ to $\cos(\kappa_1)\cdot\cos(\kappa_2) = -1$ [5].

2.5.4 Winding Number and Mean Chiral Displacement

The topological invariant chosen for our kicked rotor models is the so called winding number ν. As shown in [13], the chiral symmetry of the Hamiltonians allows us to write

$$\hat{H} = \hat{H}_{ext} \otimes \hat{H}_{int} = \begin{pmatrix} 0 & H(x) \\ H^*(x) & 0 \end{pmatrix} = E(x)\vec{n}(x) \cdot \vec{\sigma}, \tag{40}$$

where $\vec{n}(x)$ is a normalized vector. The off-diagonal block form of the Hamiltonian is a direct consequence of the Hamiltonian anticommuting with the chiral symmetry operator [26]. The implication from eq. (40) is that $\vec{n}(x) \doteq (n_1(x), n_2(x), 0)^T$, meaning that $\vec{n}(x)$ is confined to a plane (see Fig. 3.5 in [13]). Moreover, because of the periodicity in position space, we get a periodicity in the energy: $E(x)\,\vec{n}(x) = E(x + 2\pi)\,\vec{n}(x + 2\pi)$.

Taking into account that the energy gap as well as the chiral symmetry have to be preserved, the winding number can be mathematically defined [27]. The winding number ν of $E(x)\,\vec{n}(x)$ is given [5] as

$$\nu = \int_0^{2\pi} \frac{dx}{2\pi} \left(\vec{n}(x) \times \frac{\partial \vec{n}(x)}{\partial x} \right)_3 \tag{41}$$

where the 3 denotes the 3-component of the vector. The winding numbers ν_1, ν_2 are used to determine the topological invariant winding numbers ν_0, ν_π for the DKRS. Note, however, that the winding numbers are undefined for the ORDKRS when the quasienergy gap closes.

The winding number is not an experimentally accessible observable. Therefore, ref. [5] proposes that instead of the winding number ν, one can determine the Mean Chiral Displacement (MCD). It is defined by

$$C_l(t) = \langle \psi_0 | \, \hat{U}_l^{-t} \, (\hat{n} \otimes \sigma_z) \hat{U}_l^t \, | \psi_0 \rangle \tag{42}$$

Ref.s [13] and [14] argue that the minus sign in front of σ_z has to be introduced as opposed to [5]. However, I found the my results in correspondence with the definition of Zhou & Gong and will therefore follow that definition. The Mean Chiral Displacement can be thought of as a measure for how much the momentum distribution shifts to the left or right [28].

Averaging the MCD over t steps in the time evolution gives us a quantity that converges to the winding number ν [5]

$$\overline{C_l}(t) = \frac{1}{t} \sum_{t'=1}^{t} C_l(t') \tag{43}$$

$$= \frac{\nu_l}{2} - \frac{1}{t} \sum_{t'=1}^{t} \int_{-\pi}^{\pi} \frac{d\theta}{2\pi} \frac{\cos[E(\theta)t]}{2} (\vec{n}_l \times \partial_\theta \vec{n}_l)_z \tag{44}$$

$$\xrightarrow{t \gg 1} \frac{\nu_l}{2}. \tag{45}$$

The integral does not contribute in the limit of many steps t, as $\cos(E(\theta))$ oscillates very fast on a scale where $(\vec{n}_l \times \partial_\theta \vec{n}_l)_z$ is approximately constant. As a result, the integral over a periodic expression vanishes [13].

With the MCD, we finally have an experimentally accessible quantity that provides us with a quantization of the topological invariants (ν_0, ν_π) [5].

In Chapter 4 of this thesis, we will only investigate the spectrum and MCD for the Floquet operator $\hat{U}_1$ since we know the spectrum is independent on the specific shape of Floquet operators that are connected via unitary transformations, which is the case here as stated in [5]. The MCD for $\hat{U}_1$ and the winding number ν_1 are shown in figure 2. We can see as derived in [5] and tested in [14], that the MCD approaches half the winding number.

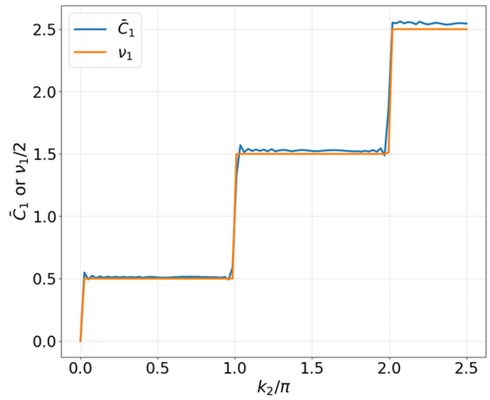

Figure 2: Mean Chiral Displacement $\bar{C}_1(t)$ and winding number ν_1 for the Floquet operator $\hat{U}_{1,ORDKRS}$ of the ORDKRS. The average was taken over $t = 20$ with a basis of $n \in [-75, 75]$. For the initial state in momentum space, we chose $\delta(n = 0)$. The time parameters are chosen as $\tau_1 = \tau_2 = 4\pi$ and $\tau_{p,1/2} = 0$.

Note, that for $\overline{C_1}(t)$ to converge to $\frac{\nu_1}{2}$, the number of kicks t as well as the basis length have to be chosen large enough. Reference [14] showed that for $t = 20$, the MCD and the winding number are in very good agreement while optimizing the numerical efficiency. For numerical calculations, it is faster to choose a large t and a smaller n. However, n cannot be chosen too small as the influence of the boundaries becomes to strong then. Therefore, one has to carefully tune n_{max} and τ in order to get good resolution of the graphs.

Later on we will choose a rather short momentum basis: $n_{max} = 30$. In this case, $t = 20$ does not work. The explanation for this is, that if $t \approx n$, we kick the system so often, that it is reflected several times at the edge of the basis. The reflected waves then interfere with each other, leading to a complicated decomposition in the momentum basis. To avoid this problem, one can follow the approximate rule that t should always be smaller than n. We account for this by choosing $t = 15$ for the DKRS.

2.5.5 Topological Invariants and Topological Phases of the ORDKRS

Topological phases of the ORDKRS are classified by a pair of integers ($\mathbb{Z} \times \mathbb{Z}$) [5]. The integers are defined in the two chiral symmetric time frames belonging to $\hat{U}_1$ and $\hat{U}_2$. Paper [28] shows that this pair of integers $(\nu_0, \nu_\pi) \in (\mathbb{Z}, \mathbb{Z})$ can be related to the winding numbers under our chiral symmetric Floquet operators ν_1, ν_2:

$$\nu_0 = \frac{\nu_1 + \nu_2}{2}, \quad \nu_\pi = \frac{\nu_1 - \nu_2}{2}. \tag{46}$$

These winding numbers (ν_0, ν_π) are the topological invariants of the DKRS and we can use them to completely classify the topological phases of $\hat{U}_R$. It is known that when the quasienergy bands $\pm|E(\theta)|$ become gapless, the winding number definition of $\nu_{1,2}$ and therefore the definition of $\nu_{0,\pi}$ is undefined [5, 13]. Since the points at which the gaps close are dependent only on κ_1 and κ_2, a plot can be created, that shows at which points the winding numbers are undefined. These boundaries are the topological phase boundaries. When such a boundary is crossed, a quasienergy gap closes - a topological phase transition occurs. In [5], the topological phase diagram of the ORDKRS against the kicking strengths (κ_1, κ_2)) is derived:

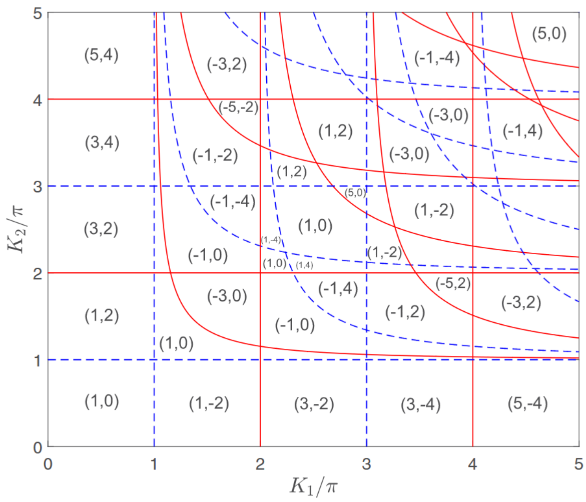

Figure 3: Topological Phase Diagram of the ORDKRS for the Floquet operator $\hat{U}_{ORDKRS}$ against the kicking strengths (κ_1, κ_2). (K_1, K_2) as labeled in the figure are defined in the same way as (κ_1, κ_2) here. The red solid (blue dashed) line represent the phase boundaries at which the quasienergy-spectrum gap closes at energy $\epsilon = 0\,(\pi)$. In the figure, the pair of winding numbers (ν_0, ν_π), characterizing each topological phase are marked. Every topological phase corresponds to a closed patch. The figure is taken from [5], with kind permission from the authors.

2.5.6 Bulk-Edge Correspondence

In systems with open boundary conditions, one has to distinguish between so called bulk and edge states. The bulk can be understood as the center portion of the system. It is defined as that part of the system that possesses translational symmetry [26]. A system under open boundary conditions always leads to edges. The edges are the "cutoff" of the system: here, translational symmetry is broken. Edges lead to the rise of edge states as seen later [8].

Subjecting a system to periodic boundary conditions means that we reduce it to its bulk [25]. The bulk-edge correspondence allows us to connect the number of edge states to the winding numbers, see [5] and [28]: The value of ν_0 (ν_π) equals the number of degenerate edge state pairs at quasienergy $\epsilon = 0$ ($\epsilon = \pi$) in the momentum space lattice. It is shown in [5], [28] that this set of integers predicts the number of degenerate 0- and π-quasienergy edge states of $\hat{U}_{ORDKRS}$. This bulk-edge correspondence is pictured in the following pictures, we generated based on Fig. 2 in [5]. They are shown here to explain the idea of how one can read off the number of edge states from the plots of the Floquet spectrum against the kicking strength k_2 and the quasienergy spectrum against the index at fixed kicking strength k_2.

The plots have to be read as follows: Avoided crossings or degenerate states in the Floquet spectrum (Fig. 4) mark topological phases. As denoted by the dashed lines, we can divide the spectrum in areas with fixed topological invariants that are given by the pair of winding numbers (ν_0, ν_π). Those are denoted in colors in Fig. 4 below.

One can then choose a kicking strength k_2 that belongs to one topological phase, e.g. $k_2 = 0.5\pi$ (Fig. 5a), $k_2 = 1.5\pi$ (Fig. 5b) or $k_2 = 2.5\pi$ (Fig. 5c). Plotting the quasienergy against the index (Fig. 5) is the same as taking a vertical cross-section of the Floquet spectrum against the kicking strength (Fig. 4).

The plots in Fig. 5 allow us to read of the number of edge states: In Fig. 5a, we can read off one pair of edge states at quasienergy $\epsilon = 0$. In Fig. 5b, we see one pair of $\epsilon = 0$ quasienergies and two pairs of $\epsilon = \pi$ edge states. Figure 5c shows three pairs of $\epsilon = 0$ edge states and two pairs of $\epsilon = \pi$ edge states.

The bulk-edge correspondence is now the following: If we compare the pair of winding numbers (ν_0, ν_π) of the topological phases that we wrote down in Fig. 4 to the number of edge states that we can read off Fig. 5, we see that the winding numbers match the numbers of degenerate edge states. This is the bulk-edge

correspondence: From the topological phases, for which we have an analytical and graphical prediction given by eq. (38) and Fig. 3, we can predict the number of edge states that arise under open boundary conditions for fixed kicking strengths k_1 and k_2 [5].
In this thesis, we want to test whether a similar correspondence can be found for the antiresonant case as well, and whether the correspondence holds when introducing a finite kicking duration impacting the boundaries.

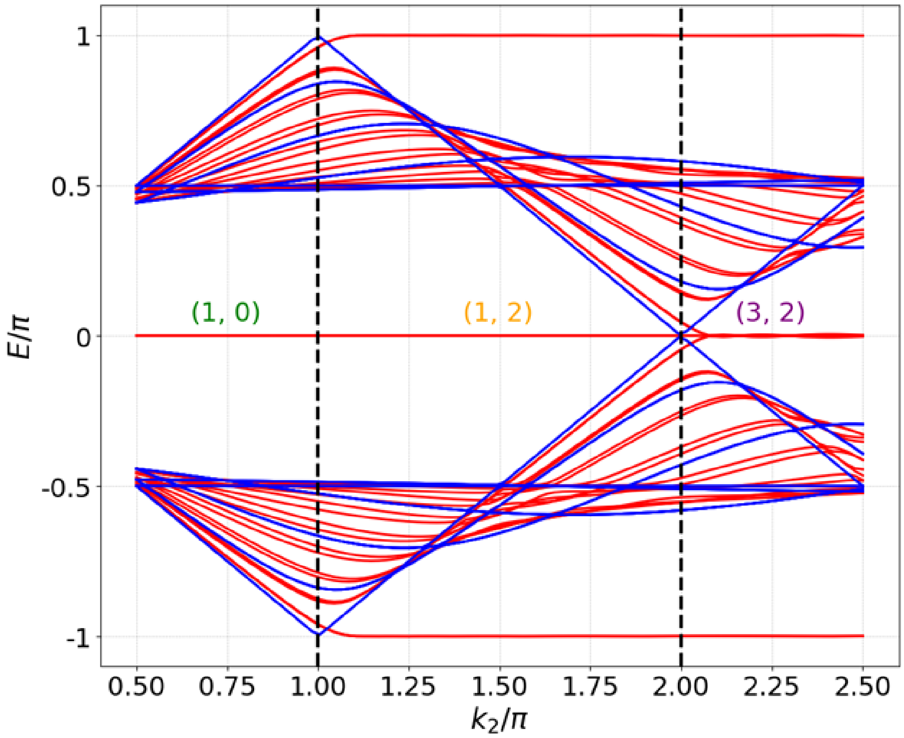

Figure 4: Floquet spectrum of $\hat{U}_{ORDKRS}$ against the kicking strength k_2. The momentum basis has length $n = 20$ and we choose $k_1 = \frac{\pi}{2}$. Open boundary conditions are shown in red, PBCs in blue. For open boundary conditions, the quasienergies are degenerate at $\epsilon = 0, \pm\pi$. Periodic boundary conditions show no degeneracy. Three different topological phases emerge; their winding numbers are $(\nu_0, \nu_\pi) = (1, 0)$, $(1, 2)$ and $(3, 2)$ as written in the plot. They are separated by the transitions at $k_2 = \pi$ and $k_2 = 2\pi$.

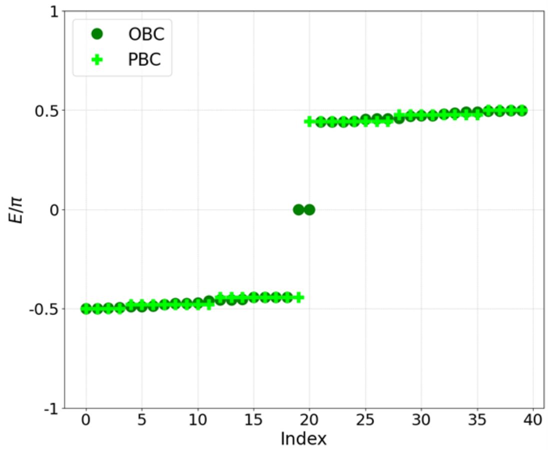

(a) Quasienergy spectrum at $k_2 = 0.5\pi$. OBCs show a pair of $\epsilon = 0$ edge states as given by $\nu_0 = 1$.

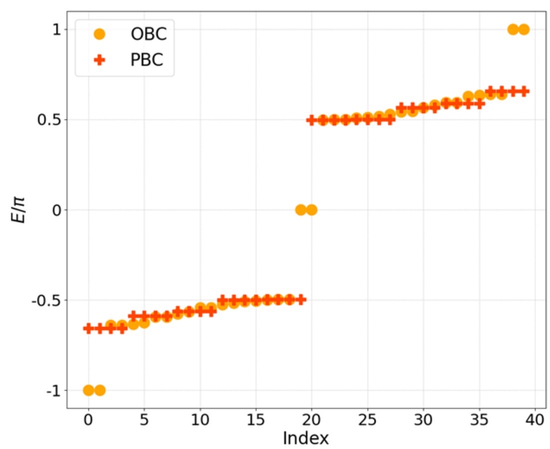

(b) Quasienergy spectrum at $k_2 = 1.5\pi$. OBCs show a pair of $\epsilon = 0$ and two pairs of $\epsilon = \pm\pi$ edge states corresponding to $(\nu_0, \nu_\pi) = (1, 2)$.

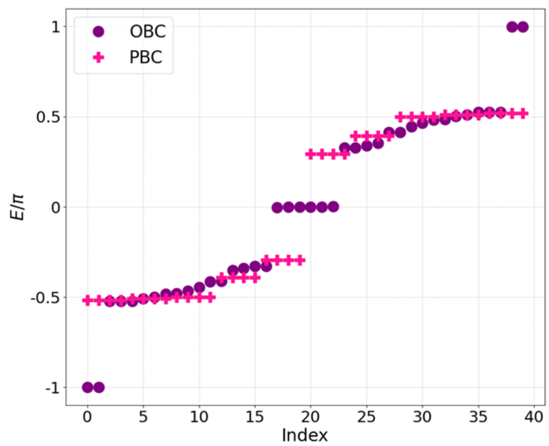

(c) Quasienergy spectrum at $k_2 = 2.5\pi$. OBCs show three pairs of $\epsilon = 0$ and two pairs of $\epsilon = \pm\pi$ edge states corresponding to $(\nu_0, \nu_\pi) = (3, 2)$.

Figure 5: Floquet spectra of $\hat{U}_{ORDKRS}$ at fixed kicking strengths k_2. The bulk-edge correspondence is visible: The number of quasienergy edge states equals the pair of winding numbers (ν_0, ν_π). The states at quasienergies 0 and $\pm\pi$ are always double degenerate: their number is twice the winding number ν.

This section concludes the overview on the theoretical fundamentals of the Quantum Kicked Rotor (QKR) and the Spin-1/2 Double Kicked Rotor (DKRS). We outlined the background on the Hamiltonian and Spectra and introduced the boundary conditions that were used for the numerical simulations. The numerical tools for these simulations were presented. Finally, we gave a thorough summary of the topological properties and invariants the DKRS displays.
Based on this theoretical framework, we now want to study our research hypotheses. The main goal of the following two chapters is to answer how open and periodic boundary conditions both under infinitesimal (δ-like) and finite kicking duration, influence the dynamics and Floquet quasienergy spectrum of both the QKR and the DKRS. Additionally, for the DKRS, we want to comment on whether the MCD is a meaningful experimental observable, as proposed.
The third chapter relates to the Quantum Kicked Rotor (QKR). In the fourth chapter, the Spin-1/2 Double Kicked Rotor (DKRS) is discussed.

3 Quantum Kicked Rotor

For this part, we investigated the influence of different boundary conditions on the spectrum and dynamics of the QKR. The novel insight that has been found is that under open and periodic boundary conditions, as well as when implementing a finite kicking time τ_p, the quasienergy spectra show discrete points at which the quasienergies differ depending on the boundary conditions. In the antiresonant case, we could even show that the eigenvectors corresponding to those discrete deviating quasienergies localize at the edge of the momentum basis. The following section will present the form of these deviating spectra and an explanatory approach for the origin of these deviations.

3.1 Dynamic Calculations

The motivation for looking at the dynamics is the following: the probability distribution shows us how the system moves. It is directly correlated to the mean energy as $\bar{E} \sim \langle n^2 \rangle$. The mean energy can then be compared to the spectrum. Gaps and deviating points in the spectrum can support or impede the energy transport which would cause the energy to increase or saturate. The dynamic calculations, i.e. the probability distribution $|\psi(n,t)|^2$ against the momenta n as well as the mean energy $\bar{E}(t)$ against the number of kicks t has been performed before in [12] and was part of the preceding project work (appendix D). However, these calculations can also be made under the different boundary conditions. We implement periodic boundary conditions and a finite kicking duration $\tau_p \in [10^{-4}, 10^{-3}, 10^{-2}]$. For the finite kicking duration, we then use both open and periodic boundary conditions. The probability distribution for these four cases (OBC and PBC; finite kick with OBC and finite kick with PBC) as well as the averaged energy can then be compared, see Fig.s 6 and 7.

Antiresonance As stated in [1], the antiresonance is special to the QKR. The reason for that is, that the antiresonant case is the only case in which the plane wave solution ψ to the Schrödinger equation is periodic with a periodicity of two kicks. To look at the antiresonant case, we choose $\tau = 2\pi$. It shows, that the probability distribution is slightly wider for a finite kicking duration, e.g. $\tau_p = 10^{-2}$, compared to the infinitesimal case. The use of open or closed boundary conditions does not influence the probability distribution.
It is indicated by the saturation of the average energy $\bar{E}(t)$ that in the antiresonant case, energy transport is impeded. The slight rise of the averaged energy for finite kicking duration compared to infinitesimal kicks (Fig. 6b) agrees with the probability distribution being slightly wider.
The dynamic calculations confirm our expectations. As explained in sec. 2.1.5, two successive kicks compensate each other. Because of that, the probability distribution strongly localizes in momentum space, and only shows two distinct curves: the initial probability distribution showing a probability of 1 at $n = 0$ and the probability after one kick, before it is compensated again by the second kick.
The compensation of the kicks also explains the saturation of the averaged energy. $\bar{E}(t)$ becomes constant as the system effectively self-compensates its motion and stays localized.
In the case of finite kicking duration, i.e. the soft-wall boundary conditions, the antiresonance condition for the free time evolution $\tau = 2\pi$ is not perfectly fulfilled anymore, as we chose to evolve the system freely over $\tau - \tau_p$. This causes the probability distribution as well as the averaged energy to be slightly different from the infinitesimal case. To get a further understanding for the origin of these deviations and the general influence of boundary conditions to the system, we investigate the spectra of the QKR under the four combinations of boundary conditions.

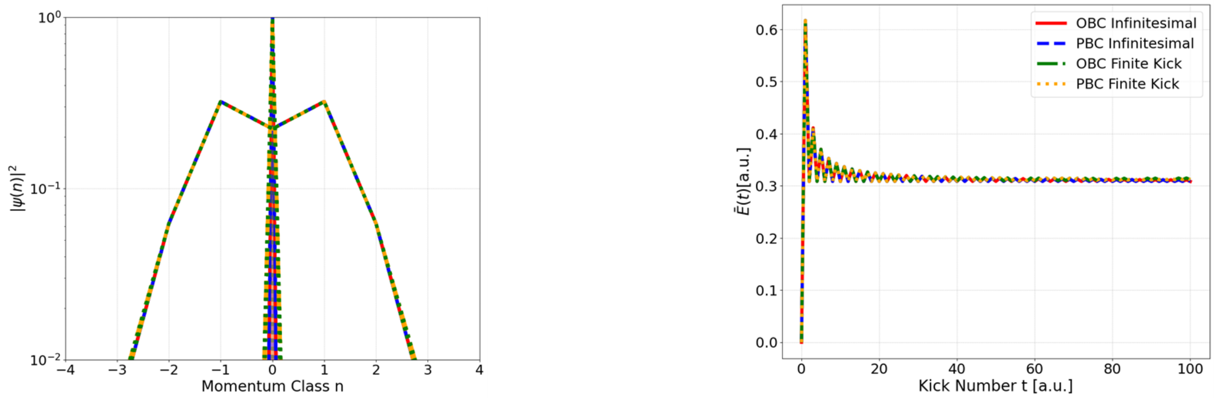

(a) Comparison of the probability distributions (OBC infinit. in red, PBC infinit. in blue; OBC finite in green, PBC finite in orange). The probability distribution is slightly wider under finite kicking duration compared to infinitesimal kicking.

(b) Comparison of the averaged energies. $\bar{E}(t)$ is almost identical for all combinations of different boundary conditions: under finite kicking, $\bar{E}(t)$ is marginally larger compared to the infinitesimal case.

Figure 6: Comparison of $|\psi(n,t)|^2$ and $\bar{E}(t)$ under the influence of different BCs and kicking durations in the antiresonant case - The cases of an infinitesimal kicking duration are shown in red for open and in blue for periodic boundary conditions. The probability distribution and averaged energy under a finite kicking duration of $\tau_p = 10^{-2}$ are shown in green for OBCs and in orange for PBCs.

We choose a basis of length $n_{max} = 200$ which will prove to be advantageous later on. The kicking strength is chosen to be $k = \pi/2$, while the kicking duration is $\tau_p = 10^{-2}$. As the initial wave, we chose $\psi_0 = \delta(n = 0)$, meaning that we start with the system being prepared only in state with momentum $n = 0$.

Resonance In the resonant case, $\tau = 4\pi$, the probability distribution and mean energy are examined as previously. In order to maintain clarity, the probability distribution is only depicted for a limited number of performed kicks t.

For investigating the spectrum in resonance, we had to choose a short momentum basis with $n_{max} = 15$. By choosing such a short basis, we effectively "move the edges" of the numerical box further to the middle of the system and therefore intensify the influence of the boundary conditions on the dynamics of the system. However, one has to be careful when making the basis shorter, that the "soft wall" we achieve by introducing a finite kicking duration, still has to lie within the numerical box in order for the system to "see" and interact with the "soft wall". Based on the results of the preceding project work, we know, that we have to choose a kicking duration of $\tau_p = 10^{-1}$ (see table 1). That way, the "soft wall" is around momenta $n \approx 5 - 6$ which is within the numerical box limited by $n_{max} = 15$.

Figure 7a confirms that the probability distribution spreads ballistically as expected (see sec. 2.1.4). This is also demonstrated by the mean energy, which initially increases quadratically. This quadratic increase provides a theoretical basis for the potential energy transport in the resonant case of the QKR. However, the averaged energy then saturates. The reason for that is, that the system dynamically evolves and spreads out in momentum space towards the edges of our numerical box. At the edges of this box, the system is then reflected and self-interferes. This leads to the saturation of the energy. We see in Fig. 7b that the averaged energy is larger under open boundary conditions (both under infinitesimal and finite kicking duration) when compared to the averaged energy under periodic boundary conditions. We can explain this the following: under OBCs, the system progresses towards the edge. There it then reflects. However, PBCs force the system to "wrap around" at the edge of the numerical box. This effectively makes the box one momentum class smaller. If we, e.g., choose $n_{max} = 15$, for OBCs, the momenta can take 31 values. For PBCs, on the other hand, we identify the momentum class $n = 15$ with $n = -15$. Effectively, the basis with $n_{max} = 15$ then takes only 30 values. We tested this statement and could see that changing the value of n_{max} by one leads to a difference of the averaged energy in the same order as the discrepancy between $\bar{E}(t)$ under OBCs and PBCs in Fig. 7b. This is shown in app. B.1.

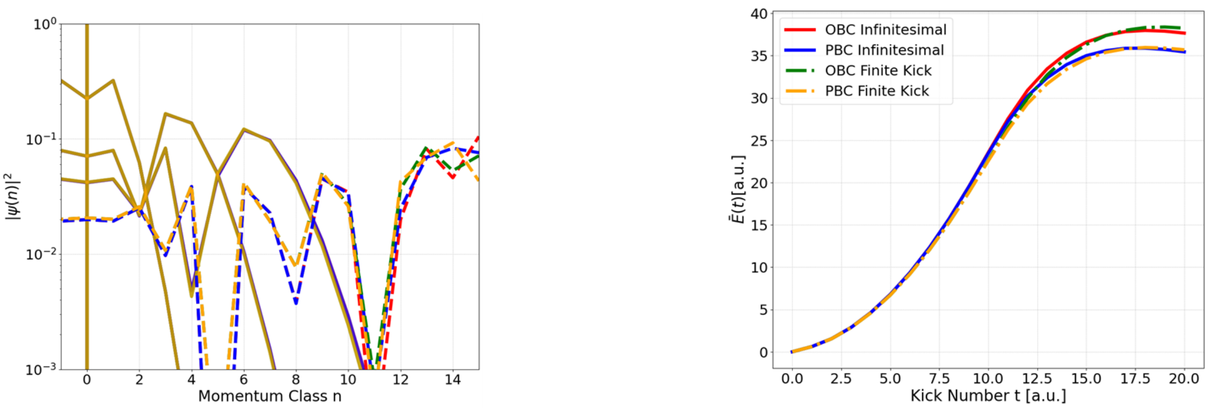

(a) Comparison of the probability distributions. The colors are chosen according to Fig. 7b. We show only the probability distribution for $[0, 1, 5, 10]$ performed kicks for all combinations of boundary conditions. The probability distributions shows the expected ballistic spreading. The curve after $t = 10$ kicks is shown in dotted lines - we can see that the system is reflected at the edge of the momentum basis.

(b) Comparison of the averaged energy. $\bar{E}(t)$ is larger under open boundary conditions for both durations of the kick, compared to the averaged energy under periodic BCs.

Figure 7: Comparison of $|\psi(n,t)|^2$ and $\bar{E}(t)$ under the influence of BCs and the kicking duration in the resonant case. - The cases of an infinitesimal kicking duration are shown in red for open and in blue for periodic boundary conditions. The probability distribution and averaged energy under a finite kicking duration of $\tau_p = 10^{-1}$ are shown in green for OBCs and in orange for PBCs.
The probability distribution is only shown for positive momenta n as it is symmetric around $n = 0$.
As the initial state, we chose $\psi_0 = \delta(n = 0)$, and for the kicking strength $k = \pi/2$, as before. The maximum momentum is $n_{max} = 15$; the finite kicking duration is $\tau_p = 10^{-1}$.

A direct comparison (open and periodic boundary conditions, each under infinitesimal or finite pulse duration) reveals that while the probability distributions are very similar under the different BCs, see Fig. 7a, the averaged energy is visibly higher under open BCs compared to periodic BCs, Fig. 7b. The probability distributions show the ballistic spreading in momentum space that we expect, albeit the curve is not as smooth, as the basis length is very short ($n_{max} = 15$).
The results from the resonant case cannot be directly compared to those in the antiresonant case, as the length of the numerical box differs significantly. However, investigations that are not shown here, but have been performed in the course of this work, showed that the observations under both resonance conditions are consistent with each other.

3.2 Spectrum

Besides the dynamic calculations of the probability distribution $|\psi(n)|^2$ and the averaged energy $\bar{E}(t)$ we can also investigate the spectrum of the QKR in the above cases. Plotting the quasienergy spectrum of the Floquet operator $\hat{U}$ directly displays differences caused by the choice of boundary conditions.
As further discussed below, in the antiresonant case, the spectra under open and periodic boundary conditions deviate in a few discrete points. For further investigation, we plotted the distribution of the eigenvectors, which correspond to the deviating points in the spectrum, looks like among the different momenta classes n. It shows that the eigenvectors correlating to the deviating quasienergies are highly

localized at the edges of the momentum basis. Moreover, those eigenvectors are not plane waves anymore.

3.2.1 Antiresonance

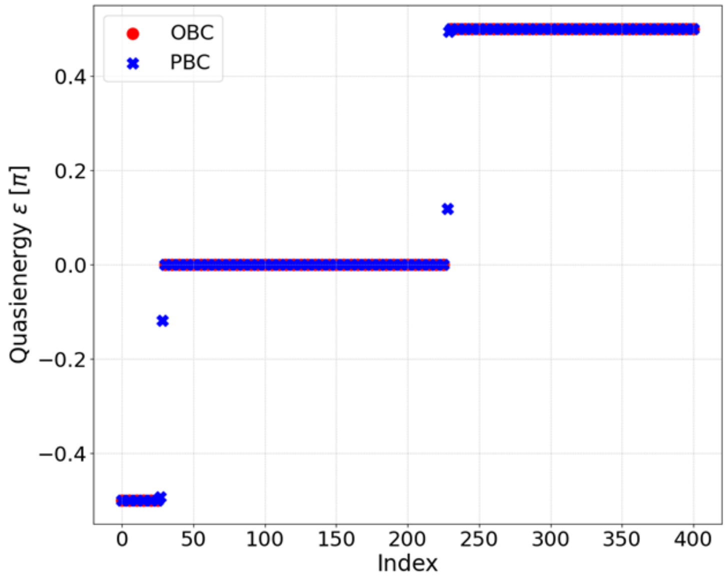

(a) Spectrum of the QKR in antiresonance. PBCs show four deviating quasienergies when compared to the spectrum under OBCs. To maintain visual clarity, only every second point is shown. However, all points that deviate between the spectrum under OBCs and PBCs are plotted.

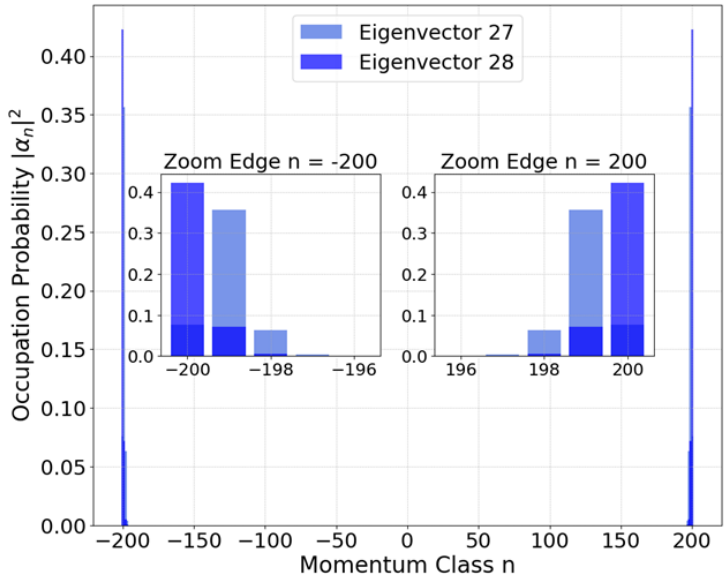

(b) Zoom into the quasienergies that deviate in the spectrum under PBCs from the spectrum under OBCs: Occupation probability $|\alpha_n|^2$ of the momenta classes n for the eigenvectors corresponding to the deviating quasienergies. The zoom into the edges of the numerical box shows that the eigenvectors localize around the edges.

Figure 8: Investigation of the deviating quasienergies and their eigenvectors of the QKR under PBCs when compared to OBCs. The spectrum under PBCs shows four deviating points. Examining the eigenvectors corresponding to the deviating quasienergies shows a localization around the edges of the momentum basis.
As parameters, we used $n_{max} = 200$, $k = \pi/2$ and $\tau_p = 10^{-2}$.

In the spectrum of the QKR under periodic boundary conditions, with a parameter choice of $k = \frac{\pi}{2}$, there are four points at which the quasienergy under PBCs deviates from the spectrum of the QKR under open boundary conditions. The number of these points depends only on the choice of kick strength k. A systematic variation of the basis length $n \in \{40, 100, 200, 400\}$ was performed, confirming that the basis length has no influence on the number of "deviating" points in the spectrum under PBCs.
Looking at the occupation probability $|\alpha_n|^2$ of the momenta classes n for the eigenvectors belonging to the deviating quasienergies, shows that those eigenvectors localize around the edges of the momentum basis $\{|n\rangle\}_n$. Moreover, the momenta classes are occupied symmetrically as can be seen in Fig. 8b. It should be noted here, that the plot of the occupation probabilities was only made for the eigenvectors no. 17 and 18. The spectrum of the QKR is symmetric around $\epsilon = 0$ due to the symmetry of the Floquet operator. Therefore, it is sufficient to examine only the eigenvectors of the quasienergies in the negative part of the spectrum. In order to be certain, it was also numerically verified that the eigenvectors of the positive deviating quasienergies possess equivalent occupation probabilities.

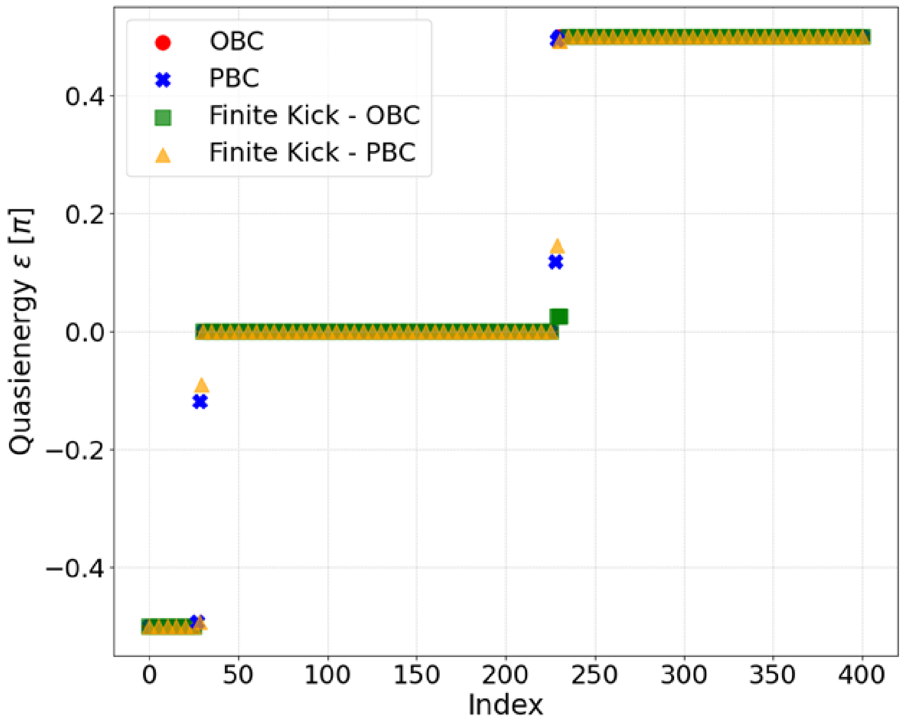

Figure 9: Spectrum of the QKR in antiresonance and with a finite kick duration of $\tau_p = 10^{-2}$. Only every second quasienergy is plotted in the bulk.
For OBCs under finite τ_p, two points in the spectrum are taking different quasienergies than $\epsilon = 0, \pm\pi$. PBCs show four deviating quasienergies both for the infinitesimal and finite kicking duration.

Introducing the finite kicking duration τ_p, the general structure of the spectrum does not change. Periodic boundary conditions again lead to four deviating quasienergies.
It is interesting to note here, that for a kicking duration of $\tau_p = 10^{-2}$, open BCs lead to deviating quasienergies, see Fig. 9.
Examining the eigenvectors to the deviating quasienergies under OBCs and $\tau_p = 10^{-2}$ we see that, again, only momentum classes at the edge of the numerical box are occupied: the eigenvectors localize strongly at the edge of the momentum basis. Only three momentum classes are occupied. However, here the eigenvectors do not symmetrically occupy the momentum basis, but localize at only on edge (Fig. 10) in contrast to e.g. Fig. 8b, where the eigenvectors are symmetrically localized equally at both edges. The explanation for this is that under periodic boundary conditions, the edge of the momentum basis at one

end is connected with the other edge of the basis by the boundary conditions. Therefore in the periodic case, the edge momenta classes are the same: $n = 200 \hat{=} n = -200$.
It should be noted, that the deviating two points under OBCs and finite kicking duration are only showing for $\tau_p = 10^{-3}$, $\tau_p = 10^{-2}$ and $\tau_p = 10^{-1}$. Yet, for $\tau_p = 10^{-4}$ the soft walls still lie within the numerical box, as $n_L = 150 - 184$. So the soft wall should still affect the dynamics of the QKR even for $\tau_p = 10^{-4}$. Examining the occupation probability $|\alpha_n|^2$ of the momenta classes for the eigenvectors of what should be deviating quasienergies, we find that those eigenvectors still localize. That we nevertheless do not see deviating quasienergies for OBCs and finite kicking at $\tau_p \geq 10^{-4}$ can be argued the following: for $\tau_p = 10^{-4}$, the system does not accumulate as much phase during the finite kick. Additionally, the effective coupling between edge and bulk states becomes weaker. Together, both effects are not significant enough anymore, such that the quasienergies of those localized states do not differ from the overall band structure.

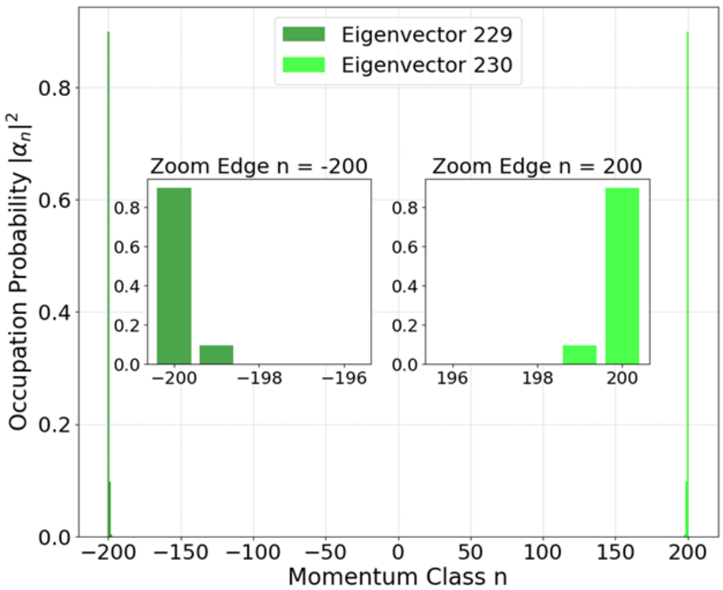

Figure 10: Occupation probability $|\alpha_n|^2$ of the momenta classes n for the eigenvectors of the deviant quasienergies under open boundary conditions and a finite kick duration of $\tau_p = 10^{-2}$.
The eigenvectors are localized at the edges of the momentum basis. They are not symmetrical, but localized at only one edge.

Again, we take a look at the eigenvectors corresponding to the quasienergies that take values different than $0, \pm\pi$, now under finite kicking duration and PBCs. We see that there are four deviating quasienergies. Their eigenvectors localize around the edges of the momentum basis. This once more points to the conclusion that the deviating quasienergies are exclusively caused by the influence of the edge of the base. We decided to show only the eigenvectors 229 and 230. Eigenvectors 28 and 29 that also lead to deviating quasienergies show the same behavior but differ slightly in the occupation probabilities. We show a comparison of the occupation probabilities for the four eigenvectors in app. B.5.

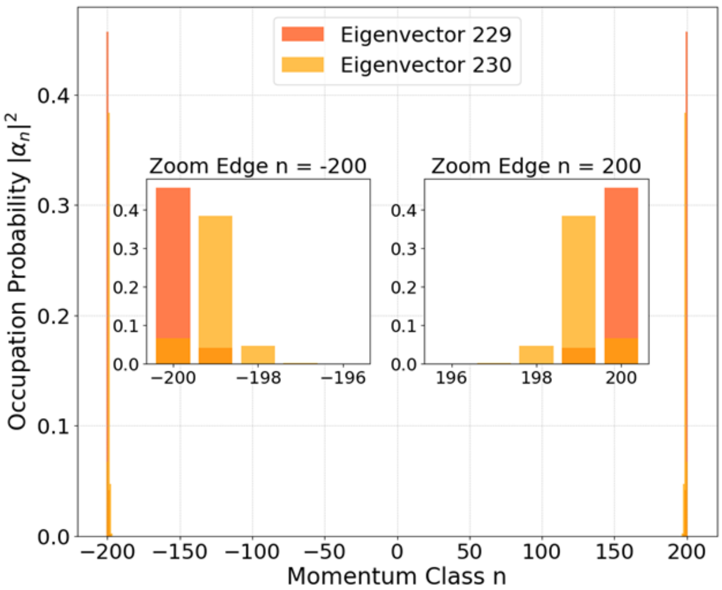

Figure 11: Occupation probability $|\alpha_n|^2$ of the momenta classes n for the eigenvectors of the deviating quasienergies under PBCs and a finite kick duration of $\tau_p = 10^{-2}$. The eigenvectors localize around the edges of the momentum basis.

One might try to understand the influence of the soft wall that arises under a finite kicking duration better. We can test whether we see direct localization at this n_L for the eigenvectors. To do so, one idea is to investigate the occupation probability of the momentum classes. Form the preceding project work, we know the position of the soft wall (see table 1). In the case of $\tau_p = 10^{-2}$ it is $n_L \approx \pm(16-19)$. Our ansatz was to determine those eigenvectors that had the highest combined probability to occupy the momenta classes $n_L = [15, ..., 20]$. Then, we plotted the occupation probability $|\alpha_n|^2$ for these eigenvectors. This study is performed in appendix B.2. What we can conclude from the occupation probability in Fig. 22a is that we do not see a direct influence of the soft wall in a form that it leads to the localization of eigenvectors.

Summary In antiresonance, the boundary conditions give rise to a finite number of deviating quasienergies between the spectra. Choosing the spectrum under open boundaries as a reference, there arise four deviating quasienergies for periodic boundary conditions (under the choice of $k = \frac{\pi}{2}$, see discussion around Fig. 5). This number stays the same when alternating the basis length n and even when we introduce the finite kicking duration τ_p.

Plotting the occupation probability of the momenta classes for the eigenvectors generating the deviating energies, we see that the deviations are caused solely by the influence of the edge of the momentum basis. Surprisingly, the spectrum under a kicking duration of $\tau_p = 10^{-2}$ and OBCs shows two deviating quasienergies. Their eigenvectors also localize around the edges of the momentum basis.

In a try to further understand the influence of the soft wall, we tested whether eigenvectors localize at the momentum classes of the soft wall n_L. The result was, however, that we could not detect such a localization.

The form of the spectrum can be explained considering the form of the average energy. We saw in sec. 3.1, that the averaged energy saturates. This makes it plausible, that the spectrum shows only flat energy bands. The four quasienergies arising from PBCs are not significant enough to show their influence on the averaged energy.

3.2.2 Resonance

In resonance, the system is very stable against changes in the boundary conditions: Choosing a large basis ($n_{max} = 100$, such that the numerical box size is $N = 201$), there is no visible deviation between the spectra under open and periodic boundary conditions. However, if we choose the momentum basis to be small enough, the quasienergies differ pairwise as shown in Fig. 12. Therefore, we focus on the case of a small basis with $n_{max} = 15$ ($N = 31$). One has to be careful when choosing the kicking duration here: As we know from the project work, a kicking duration of $\tau_p = 10^{-2}$ places the soft wall around momenta of order $n \approx 15 - 20$. Choosing this kicking duration would mean, that the rotor effectively would not see the soft wall as it would be reflected by the edge of the momentum basis, before it could reach the soft wall. Therefore, we have to choose a kicking duration of $\tau_p = 10^{-1}$ in order for the soft wall to lie within the size of the numerical box.

In the resonant case, the Floquet operator $\hat{U}$ reduces to the kicking part: $\hat{U}_{kick} = e^{-ik\cos\hat{\theta}}$. This operator is diagonal in the position basis $\{\theta\}$ with eigenvalues $k\cos\theta$ [1]. Comparing the spectra under different boundary conditions to this analytical solution (Fig. 12), we see that none identically match the analytical solution. However, the reason for that must be found in the way of the presentation: We calculate the quasienergies as the eigenvalues of the Floquet operator. A priori, those eigenvalues have arbitrary order. To be able to compare and analyze the spectra, we have to give those eigenvalues some order. The order we choose is in ascending size. By this, we rule out the expected cosine form. A reordering of the indices and their respective eigenvalues has been performed, confirming that the spectrum does in fact match the form we would expect. Now, the combination of reordering the eigenvalues together with choosing a rather small numerical box (which leads to the discretization in "rough" steps), causes the discrepancy between the quasienergies under different boundary conditions compared to each other and to the analytical solution.

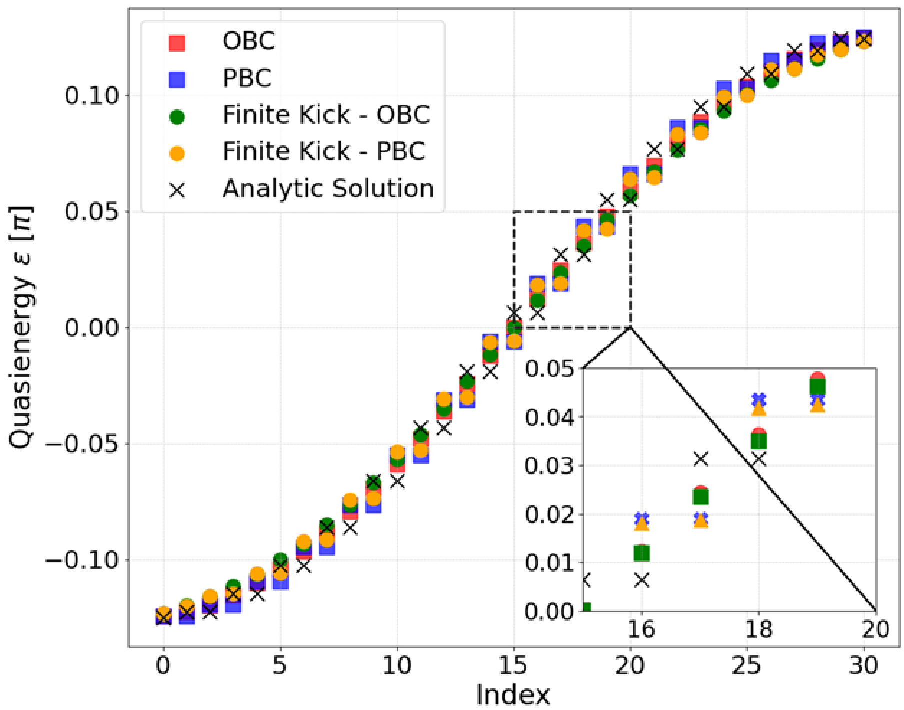

Figure 12: Spectrum of the QKR in resonance with a finite kicking duration of $\tau_p = 10^{-1}$. The spectra generally agree with each other for all different boundary conditions and kick durations. However, we see pairwise deviations in the spectrum under periodic BCs.
The parameters for this picture are: $n_{max} = 15$, $k = \pi/2$ and $\tau_p = 10^{-1}$.

We see that in resonance, the boundary conditions do not change the spectrum in the way that it is changed in antiresonance. We see some slight "pairwise" deviation of quasienergies for OBCs and PBCs compared to one another and compared to the analytical solution. Nevertheless, the source of these deviations lies rather within the discretization of an, anyhow, short momentum basis as well as how exactly the system is able to fulfill the reflection condition at the edge of the numerical box, than in some sort of localization at the edges.
As there are no specific deviating points, we cannot investigate the occupation probabilities like in the antiresonant case. However, one idea to further examine and understand the spectrum under resonance conditions is to determine those eigenvectors that have the largest occupation probability around the edge of the momentum basis. Then one can study the distribution of the occupation probabilities of those eigenvectors.
This study was performed for the cases $\tau_p = 10^{-1}$, $\tau_p = 10^{-2}$, and $\tau_p = 10^{-3}$ where we tested the overlap of the occupation probabilities for the first three edge momenta classes each. The result was, that we did not find localized eigenvector distributions but rather plane waves that had their maximum at the edges of the numerical box. The corresponding figures for $\tau_p = 10^{-1}$ can be found in appendix B.3.

Summary To recap, in the resonant case, the spectra under all boundary conditions overall match, even when introducing a finite kicking duration τ_p. The spectra under OBCs differ from those under PBCs pairwise. Both BCs are no identical match to the analytical solution. Nonetheless, those discrepancies are most likely cause by numerical relicts. We can also confirm how the size of the numerical box (momentum basis) influences the appearance of the spectrum: the shorter the basis, the greater is the influence of the BCs.
Investigating the occupation probability distributions of the eigenvectors, we can affirm that the eigenvectors are plane waves. Comparing the associated eigenvectors e.g. under PBCs with infinitesimal and finite kicking duration, we see that for an infinitesimal kicking duration, the amplitudes of the waves stay constant while for τ_p finite, they grow towards the edges of the momentum basis, see Fig. 23. Under OBCs the same behavior is found, Fig.s 24 and 25.

Influence of the kicking duration and basis length To complete the analysis of the QKR under a free time evolution of $\tau - \tau_p$, we should point out how the kicking duration τ_p and the basis length n_{max} (or N) influence the look of the spectrum.
The kicking duration τ_p determines, where in momentum space the "soft wall" arises. Table 1 gives an overview over the position for the relevant magnitudes of τ_p. The longer the kicking duration, the smaller the momentum at which the soft wall arises. The smaller the momentum at which the soft wall arises, the more likely the rotor interacts with the wall. This also means that some phenomena like the emergence of the two deviating points under OBCs in the antiresonant case, see Fig. 9, can only be seen for a long kicking duration, as only then the system interacts strongly enough with the soft wall. The effect of localization at edge momenta classes is enhanced the longer the kicking duration is. Selecting a short kicking duration ($\tau_p = 10^{-5}$ turns out to be sufficient for the QKR with a free evolution over $\tau - \tau_p$), the dynamics and spectrum that were observed under the condition of infinitesimal kicking duration will be restored. In the limit case of $\tau_p \to 0$, the dynamics and spectrum match identically again. In the project work, we have seen that the rotor interacts with the soft wall in a way that it reflects off of it but not as strongly as off the edge of the numerical box. The soft wall has to be thought off rather like a potential wall in quantum mechanics, into which a particle can tunnel over some momenta. That is why we call the wall a "soft wall". Connecting to the basis length, having a short basis means that we have to choose a rather large kicking duration (see table 1).
In general, the length of the momentum basis n_{max} determines how much the boundary conditions

influence the dynamics of the system. A short basis means that the system effectively has more edge as compared to bulk. Differences in the behavior of the system around the edge are therefore more visible for a small n_{max}. However, as long as the basis is chosen in a way, that the system reaches the edge of the numerical box, the exact length of the basis does not influence the number of deviating points in the spectrum in the antiresonant case. This number is then only dependent on the kicking strength k. We confirm this also in the case of the DKRS.

3.3 Free time evolution over τ

Up until now, all our analyses for a finite kicking duration τ_p were performed under the condition that the system freely evolves after the last kick over a time $\tau - \tau_p$. This has the experimental advantage, that we can shorten the time over which the system has to be stable, which can be advantageous especially for long kicking durations τ_p. However, it might be reasonable to also consider the case in which we always evolve over the time τ after the last kick of a kicking sequence. That way, the resonance (antiresonance) condition is precisely fulfilled, while before it was only approximately fulfilled with a larger difference for longer kicking durations. Choosing the free time evolution over τ instead of $\tau - \tau_p$, however, also means that the total time for one kicking cycle is $\tau + \tau_p$. Again, the difference becomes more relevant, the longer the kicking duration. The consequence of this is that the results from the preceding studies cannot be compared precisely, as there the one-kick cycle has a total time of τ.
We only show the spectra here. The figures for the probability distributions $|\psi(n,t)|^2$ as well as the averaged energy $\bar{E}(t)$ can be found in app. B.6.

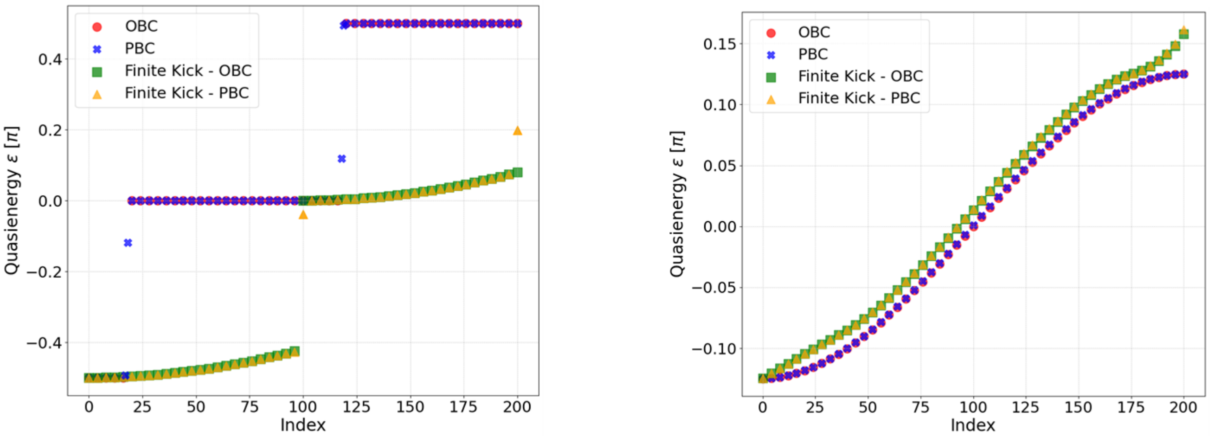

(a) Quasienergy spectrum of the QKR in antiresonance under a free time evolution over $\tau = 2\pi$. The previously flat energy bands acquire negative curvature that reminds of a cosine form (for finite kicking duration).

(b) Quasienergy spectrum of the QKR in resonance under a free time evolution over $\tau = 4\pi$. The quasienergy spectrum does not follow the shape of that under infinitesimal kicking duration anymore; it has a stronger curvature.

Figure 13: Quasienergy spectra for the QKR under a free time evolution over τ instead of $\tau - \tau_p$. The used parameters are $n_{max} = 100$, $k = \pi/2$ and $\tau_p = 10^{-4}$ for both plots.
The free time evolution over τ leads to a stronger curvature of the spectra under finite kicking duration, both in the antiresonant and the resonant case.

There are two main insights we find by evolving the system over τ instead of $\tau - \tau_p$. Firstly, we find out that the system is much more sensitive to the duration of the finite kick τ_p. Before, we saw significant changes in the spectrum for $\tau_p = 10^{-2}$. Now, at $\tau_p = 10^{-4}$ we already see the strong difference in the curvature of the quasienergy bands compared to the case of infinitesimal kicking or even the case of finite kicking but with the time evolution over $\tau - \tau_p$, see Fig.s 8a and 12. As we know, the case of resonance or antiresonance in a quantum mechanical system is very susceptible to disorders. Therefore, it is not surprising, that we do see a change of structure caused by a change of this magnitude in the period of the free time evolution.

The second and obvious observation is that the energy bands under finite kicking acquire a stronger curvature than before: the previously flat energy bands in the antiresonant case now remind of a cosine structure. In the resonant case, the energy structure still partly agrees with that under infinitesimal kicking, but differs strongly for small and high indices. Here, one has to keep in mind that the way we produce this quasienergy spectrum makes it hard to directly draw a conclusion from the shape of the spectrum: as we get the quasienergies as eigenvalues with random order and then sort them in ascending order by convention, we cannot see any underlying structure that the quasienergies would have.

One ansatz I tried to find an underlying structure was the following: As we are still in the resonant case, we do have an analytical solution to the ideal case of infinitesimal kicking duration. In resonance, the Floquet operator simplifies to $\hat{U}_{res} = e^{-ik\cos(\hat{\theta})}$ where we can simply read off the eigenvalues and quasienergies: $\epsilon_{U_{res}} = \frac{k\cos(\theta)}{\tau}$. One can then try and allocate the eigenvalues of the numerical simulation for the finite kicking case to the quasienergies we get from the analytical solution. However, different attempts to create an order in the spectrum under finite kicking duration, based on this reassigning did not lead to further insights on the structure of the quasienergy-spectrum.

Therefore, we have to rely on Fig.s 13a and 13b. A trained eye could make the hypothesis that the quasienergy spectrum in the resonant case reminds of the convolution of multiple cosine-form solutions of the tight-binding Hamiltonian. This hypothesis can be justified by the argumentation that the finite kicking duration leads to a soft wall, at which the plane-wave solutions to the QKR-Schrödinger equation reflect. Each of those plane waves would lead to a cosine form. As there are overlapping plane- wave solutions, the total solution to the Schrödinger equation might be the superposition of several cosine solutions, which could explain the form of the quasienergy spectrum in the resonant case, see Fig. 13b.

4 Double Kicked Rotor & Topology

The DKRS is particularly interesting as it is an experimentally realizable model [16, 17] combining the dynamics of periodically driven systems like the QKR with the topological properties that arise by introducing the internal spin degree of freedom [5, 18].
For this model, we again studied how different boundary conditions influence the quasienergy-spectrum. In [5], the Mean Chiral Displacement (MCD) was proposed as the experimental observable.
The focus of this second part is, whether the results of the QKR can be generalized to the DKRS and especially whether we can see differences in the MCD caused by different boundary conditions. Experimental realizations [16, 17] have motivated an interest in the resonant case in particular, such that we focus on understanding latter.

4.1 Resonance

Choosing an infinitesimal or very short kick duration $\tau_{p,i} = 10^{-4}$ in combination with a basis array of $n \in [-75, 75]$, we can confirm the results of [5]: The plot of the quasienergy against the kicking strength shows degenerate energy states at $\epsilon = 0, \pm\pi$ under open boundary conditions. Under periodic boundary conditions, the spectra are identical with that under OBCs, except for precisely these degenerate quasienergies. The finite kicking duration of $\tau_{p,i} = 10^{-4}$ does not change that behavior. Based on the project work, we expect this result, as the soft wall caused by the finite kicking duration is placed around the momentum class $\approx 150 - 193$. This means that for the chosen basis of $n \in [-75, 75]$, a kicking duration of $\tau_{p,i} = 10^{-4}$ is not long enough to show the influence in the basis length: The rotor would be reflected at the edge of the momentum basis before it could even get to the "soft wall". However, we can use this result to argument that our numerical calculations are valid in the boundary case of very short kick durations.
To assess the influence of the boundary conditions on the spectrum, we want the DKRS to "see" the edge of the numerical box. This means we have to chose a relatively short momentum basis. The shorter the momentum basis, the more the influence of the boundary conditions on the dynamics and the spectrum becomes apparent. Therefore, we choose $n \in [-30, 30]$, so that the influence of periodic boundary conditions should be clearly visible. In order for the rotor to be influenced by the soft wall, it has to lie within the basis that is restricted by $n_{max} = 30$. From table 1, we can read off, that we have to choose a kicking duration of $\tau_{p,i} = 10^{-2}$ to fulfill this criterion.
In order to be able to decide, whether the MCD is a good measuring variable, we have to make sure that our system actually expands so far that it interacts with the edge of the numerical box. This is influenced by three parameters: the basis length n_{max}, the kicking strength k_2 and the number of kicks t. For a fixed basis length, the system expands the stronger the higher k_2 and t. A systematic variation of t while keeping n_{max} and k_2 constant lead to the choice of $t = 15$, see Fig.s 31a and 31b in app. C.2. The following plots are generated with $n \in [-30, 30]$, $\tau_{p,i} = 10^{-2}$ and $t = 15$.

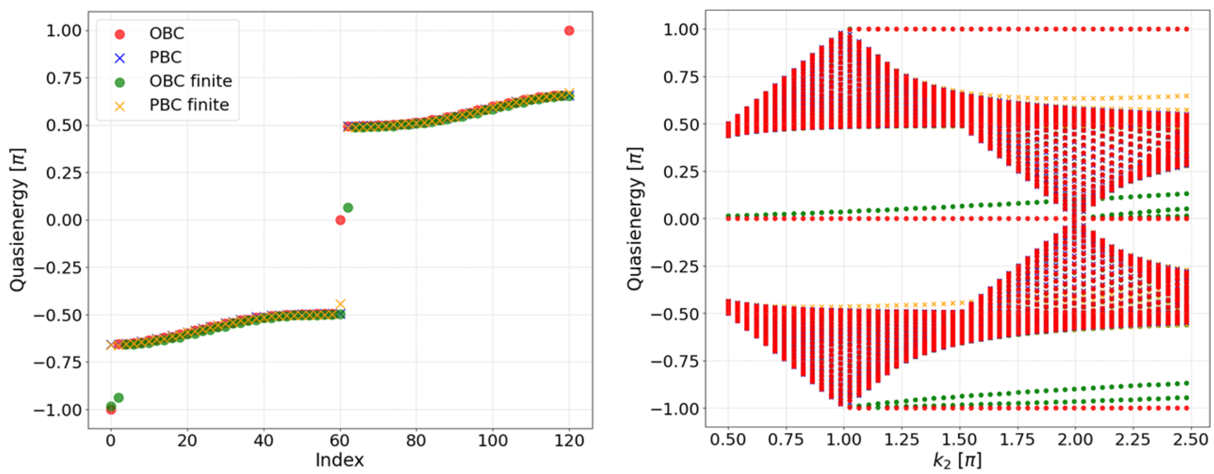

(a) Quasienergy spectrum at $k_2 = 1.5\pi$. Open boundary conditions with infinitesimal (finite) kicking duration are shown as red (green) circles. Periodic boundary conditions with infinitesimal (finite) kicking duration are shown as blue (yellow) crosses. For the sake of clarity, only every second quasienergy is plotted.
We see that under open BCs and infinitesimal kicking duration (red), there are degenerate quasienergy-states at 0 and $\pm\pi$. Under finite kicking duration, the degeneracy is lifted - still there are three pairs (only three points visible because only every second point is plotted) of quasienergies that lie within the gap of the spectral structure that is given by the rest of the points. For a finite kicking duration and periodic BCs, there exists one quasienergy at index 60 that does not follow the overall band structure.

(b) Quasienergy spectrum against kicking strength k_2. Again, only every second point is shown. The markers and colors are chosen in accordance with Fig. 14a. The red spectrum shows how the degenerate quasienergies arise at $\epsilon = 0, \pm\pi$. The green spectrum explains how the degeneracy is lifted: the bands that were completely horizontal in the case of OBCs and infinitesimal kicking duration, now have a slight curvature. As 14a is a cross section of this spectrum, this explains why for $k_2 = 1.5\pi$, we see one pair of states with quasienergy $\epsilon \approx 0.15$ in the band-gap.

Figure 14: Quasienergy spectra of the DKRS in resonance ($\tau_1 = \tau_2 = 4\pi$). The parameters are $k_1 = \pi/2$, $n \in [-30, 30]$ and $\tau_{p,1/2} = 10^{-2}$.
The upper figure shows the spectra against index, sorted in ascending order. Under OBCs, we see a discrete number of quasienergies taking values differing from the overall band-structure. Under finite kicking duration and periodic BCs, also one deviating quasienergy arises around index 60.
The lower figure shows the quasienergy-spectra of the DKRS plotted against varying kicking strength $k_2 \in [0, 2.5\pi]$. The upper figure is a cross-section of the lower picture at $k_2 = 1.5\pi$.

Figure 14a shows that under OBCs, so-called edge states arise in the quasienergy spectrum of the DKRS. The reason for that is the bulk-boundary correspondence as explained in [5] and [13]. The important part for our research question is, how the implementation of periodic BCs and the "soft wall" BCs influence the development of those degenerate edge states and especially whether we can see this in the MCD.
The first insight is, that the implementation of the finite kicking duration leads to a reversal of the degeneracy of the edge states: Figure 14b shows that especially for large kicking strengths k_2, the bands that were completely horizontal at $\epsilon = 0, \pm\pi$ under OBCs and infinitesimal kicking have negative curvature when introducing finite kicking duration (see green points in Fig. 14b). For periodic BCs and finite τ_p, the energy-bands also acquire negative curvature which leads to the emergence of the quasienergy at index ≈ 60 in Fig. 14a.
However, we cannot confirm the idea that the introduction of a finite kicking duration in combination with open BCs might reproduce the scenario of periodic BCs. This means that our results do not affirm the hypothesis, that implementing a finite kicking duration allows us to experimentally create periodic boundary conditions.
To test our second research question whether we can see the influence of different BCs in the suggested

experimental observable, the MCD, we calculate the MCD for all combinations of BCs:

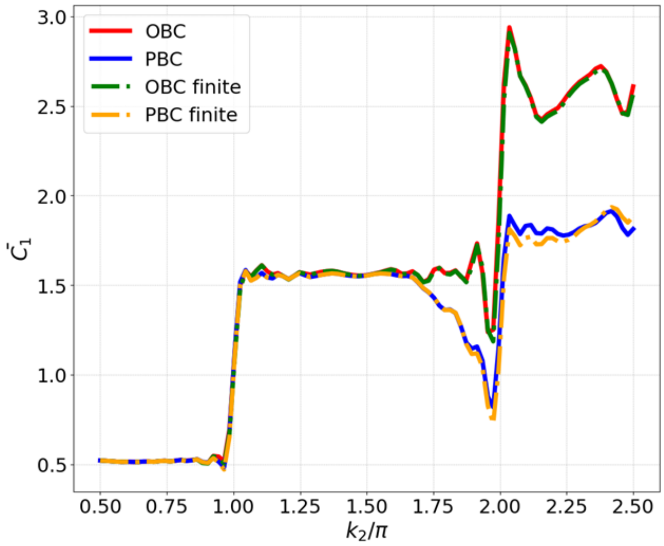

Figure 15: MCD for the DKRS in resonance with parameters $k_1 = 0.5\pi$ with varying k_2, $\tau_{p,i} = 10^{-2}$ and $t = 15$. Open BCs are shown in a red solid (green dashed) line for infinitesimal (finite) kicking duration. Periodic BCs are given as a blue solid (yellow dashed) line for infinitesimal (finite) kicking duration.
The MCD up to a kicking strength of $k_2 = 1 - 5\pi$ is the same under all BCs. Above $k_2 = 1 - 5\pi$, the MCD under open and periodic BCs deviates significantly. However, the kicking duration τ_p does not influence the MCD much.

Our numerical simulations show that for kicking strengths up to $k_2 \approx 1.5\pi$, the MCD is identical under all combinations of BCs. Beginning at about $k_2 = 1.5\pi$, the MCDs deviate: while the MCD is the same under OBCs for infinitesimal and finite $\tau_{p,i}$ (as well as for PBCs), the MCD under OBCs differs from that under PBCs. As mentioned before, the k_2 at which the MCD starts to differ between the BCs is dependent on the basis length n_{max} and the number of kicks t. The explanation for this is, that the combination of n_{max}, k_2 and t decides whether the rotor "sees" the edge of the numerical box. For fixed n_{max}, the larger k_2 and t, the faster the system expands. Fig. 15 then tells us, that for $n_{max} = 30$ and $t = 15$, the system starts to "see" the edge at $k_2 = 1.5\pi$. Moreover, we can conclude from the figure, that the choice of boundary condition does in fact influence the MCD. Only for OBCs, we get a MCD that converges to half the winding number as predicted by the bulk-edge correspondence (see discussion in sec. 2.5.6).
In the appendix, the MCD has been calculated for other choices of t, n_{max} and k_2. The systematic variation lead to the choice of $t = 15$ for the above Fig. 15 as we can already see the influence of the boundary conditions there, but also have the convergence to half the winding number for smaller k_2. However, in total, we again do not see the same result for periodic BCs and open BCs with finite kicking duration which once more suggest, that we cannot reproduce PBCs experimentally by introducing a finite kicking duration in a system with otherwise OBCs.

Localization of the Eigenvectors at the Edge It is stated [5], that the "deviating" quasienergies in the Floquet spectra on resonance are edge states. To convince ourselves whether this really means that these states are localized at the edge of the momentum basis, we plotted the occupation probability distribution of the eigenvectors against the momentum class, similar to the analysis of the QKR. The results for a kicking strength of $k_2 = 1.5\pi$ are shown here; the other figures are shown in appendix C.3. The result of this analysis is that the eigenvectors to the edge states under open boundary conditions are indeed localized at the edges of the momentum basis. Under periodic boundary conditions with a finite pulse duration ($\tau_p = 10^{-2}$), quasi-energies occur that do not follow the general band structure. The corresponding eigenvectors are also localized at the edge of the numerical box - just as in the case of the QKR.

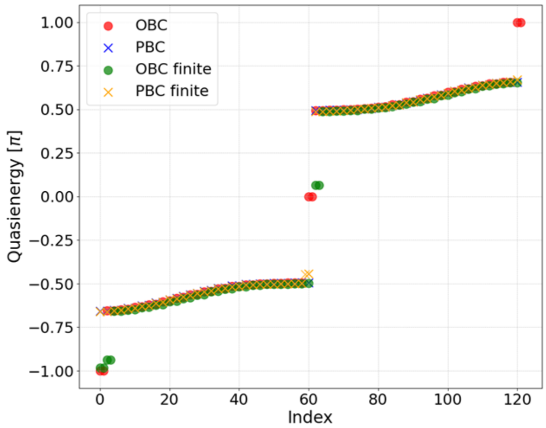

(a) Quasienergy spectrum of the resonant DKRS with parameters $n_{max} = 30$, $\tau_{p,1/2} = 10^{-2}$, $k_1 = 0.5\pi$ and $k_2 = 1.5\pi$.
Only every second quasienergy is plotted, yet all "deviating" quasienergies are shown. We see six edge states for open BCs (each under infinitesimal and finite kicking durations); for finite kicking and PBCs, there are two quasienergies that do not follow the overall band structure.

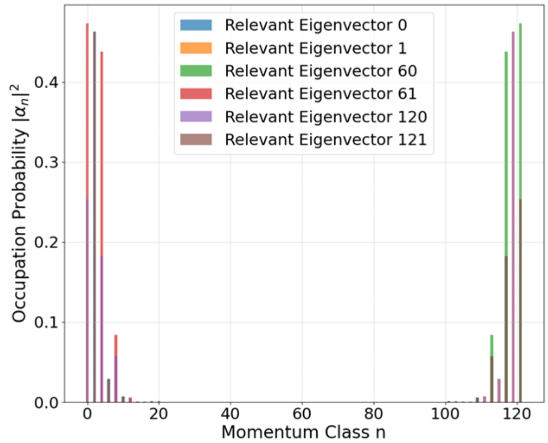

(b) Occupation probability distribution $|\alpha_n|^2$ against the momentum classes n for OBCs with infinitesimal kicking.

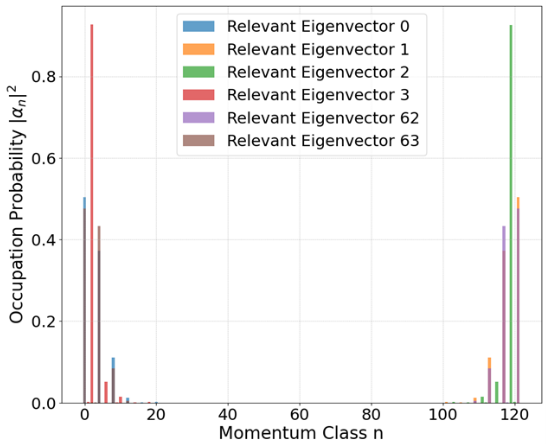

(c) Occupation probability distribution $|\alpha_n|^2$ against the momentum classes n for OBCs with kicking duration of $\tau_p = 10^{-2}$.

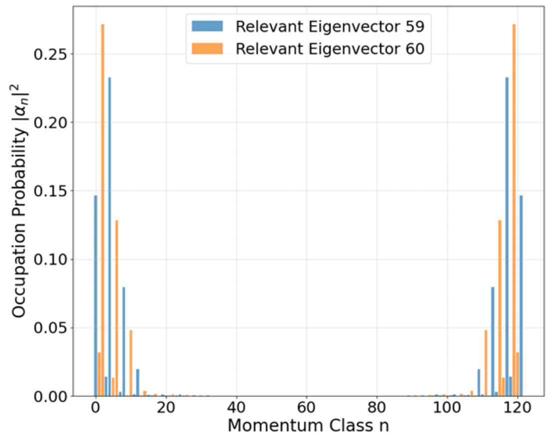

(d) Occupation probability distribution $|\alpha_n|^2$ against the momentum classes n for PBCs with kicking duration of $\tau_p = 10^{-2}$.

Figure 16: Investigation of the eigenvectors of the edge states and deviating quasienergies for the resonant DKRS. The parameters are $n_{max} = 30$, $\tau_{p,1/2} = 10^{-2}$, $k_1 = 0.5\pi$ and $k_2 = 1.5\pi$.
For all edge states (under OBCs) and the two quasienergies that do not follow the overall band-structure under PBCs with finite kicking, we plot the distribution of the corresponding eigenvectors against the momentum classes n. We see that in all cases, the eigenvectors do localize at the edges of the momentum basis.

Summary In the resonant case, we can confirm the bulk-edge correspondence shown in [5]. Moreover, we see that it still holds under finite kicking durations. The difference between infinitesimal and finite τ_p can be well seen in the quasienergy spectrum against the kicking duration (Fig. 14b). We see that under a finite kicking duration, the energy-bands acquire some curvature.
A novel insight is that the MCD is dependent on the boundary conditions. Figure 18 showed that when

the parameters are chosen in a way, such that the rotor expands up to the edge of the momentum basis, the MCD under PBCs does not take the value of half the winding number, as predicted by the bulk-edge correspondence. However, the duration of the kick τ_p does not influence the MCD significantly.

4.2 Antiresonance

For the sake of completeness, one can also look at the antiresonant case. Here, we do not have results like [5] with which we can compare our findings. However, we can compare the spectrum with what we know from the QKR.
As for the resonant case, we choose $n \in [-30, 30]$ and $\tau_{p,i} = 10^{-2}$. This leads to the following figures:

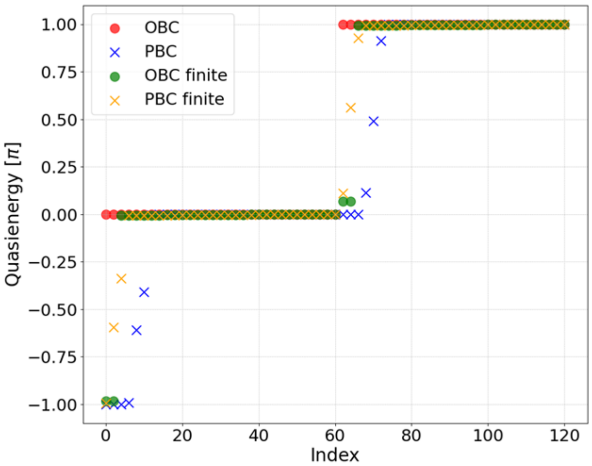

(a) Quasienergy spectrum at $k_2 = 1.5\pi$ in antiresonance ($\tau_1 = \tau_2 = 2\pi$). Open boundary conditions with infinitesimal (finite) kicking duration are shown as red (green) circles. Periodic boundary conditions with infinitesimal (finite) kicking duration are shown as blue (yellow) crosses. For the sake of clarity, only every second quasienergy is plotted.
Periodic BCs (infinitesimal & finite) lead to the rise of quasienergies in the gaps between $\epsilon = 0, \pm\pi$. Under OBCs with finite kicking duration, two points at quasienergies slightly larger than $-\pi$ and two slightly larger than 0 arise. OBCs with infinitesimal kicking show completely flat quasienergy bands.

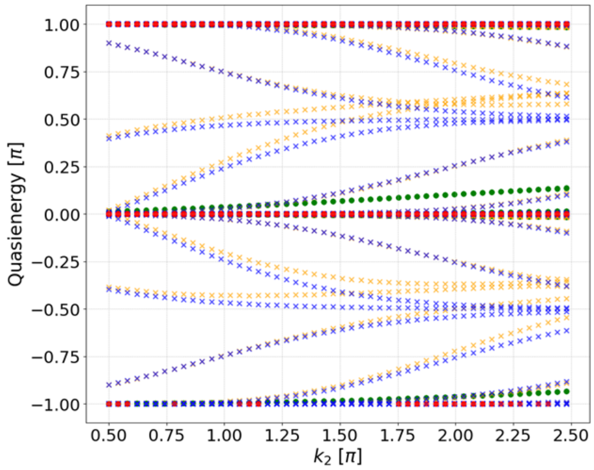

(b) Quasienergy spectrum in antiresonance against kicking strength k_2. The colors are chosen according to Fig. 17a.
We see that the quasienergies are taking only two discrete values $\epsilon = 0, \pm\pi$ under OBCs. The finite kicking duration causes the energies to get slightly larger (the stronger a effect, the larger the kicking strength k_2): the horizontal red lines turn to negatively curved green lines. PBCs show multiple different quasienergies. The finite kicking duration also leads to a negative curvature of those lines.

Figure 17: Quasienergy spectra of the DKRS in antiresonance ($\tau_1 = \tau_2 = 4\pi$). The parameters are $k_1 = \pi/2$, $n_{max} = 30$ and $\tau_{p,1/2} = 10^{-2}$.
While for open BCs we see almost only flat energy bands (see left figure), under PBCs, there are multiple quasienergies that take values different from $\epsilon = 0, \pm\pi$. Looking at the quasienergy-spectrum plotted against different kicking strengths k_2 (Fig. 17b), we see that for OBCs, the spectrum takes only two different energies while under PBCs, it takes multiple values $\epsilon \neq 0, \pi$ as well. Introducing a finite kicking duration leads to the curvature of those lines in the spectrum against k_2. In the spectrum against the index this shows as discrete points, at which the quasienergies take (multiple) values different from $\epsilon = 0, \pm\pi$.

The analysis of the quasienergy spectra under antiresonant conditions shows us that like for the QKR, periodic BCs give rise to discrete quasienergies that differ from the flat bands at $\epsilon = 0, \pm\pi$. However, as in the QKR, the combination of a finite kicking duration and open boundary conditions does not recreate the same spectrum as PBCs.
For the second research question, we again take a look at the corresponding MCD in antiresonance. Our numerical simulations show that in antiresonance, different boundary conditions show an identical MCD, see Fig. 18. In contrast to the resonant case, where at least for strong kicking $k_2 \geq 1.5\pi$ we could see

differences in the MCD under different BCs, in antiresonance the MCD stays the exact same for all BCs. The explanation of this is simple: in antiresonance, the system does not expand in momentum space, as every second kick cancels the effect of the preceding one. Therefore, in antiresonance, the rotor does not interact with the edge of the momentum basis and as a result does not show differences in the MCD depending on the choice of BCs. Hence, the MCD is not a good experimental observable for investigating the influence of boundary conditions on the spectrum and dynamics of the DKRS in antiresonance.

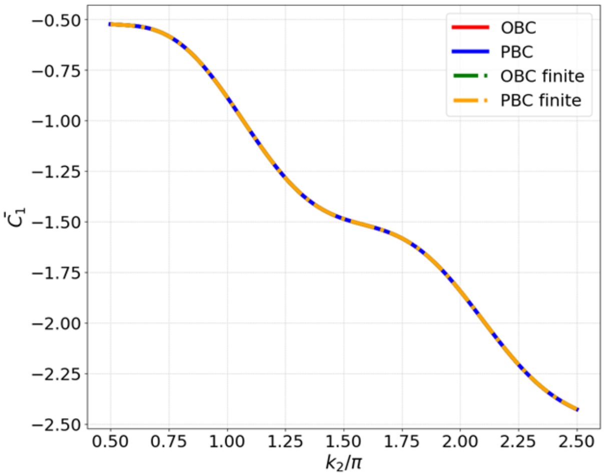

Figure 18: MCD for the DKRS in antiresonance with parameters $k_1 = 0.5\pi$, varying k_2, $\tau_{p,i} = 10^{-2}$ and $t = 15$. The MCD is the same under all different combinations of boundary conditions.

Summary In antiresonance, the DKRS shows an analogous behavior of the quasienergy spectrum against the index as the QKR. We again see discrete quasienergies that take values different from the expected $\epsilon = 0, \pm\pi$. Under a finite kick duration and OBCs, we see two quasienergies that lie above $\epsilon = 0$ (Fig. 17a). The spectrum against the kicking strength k_2, Fig. 17b, is in accordance with the resonant case: we again see the increase in the slope of the quasienergy bands for finite kicks. However, the MCD displays a different result than in the resonant case: as the system does not expand far in momentum space in the antiresonant case, it does not interact with the edge of the momentum basis. Because of that, we do not see a difference in the MCD, as the system does not ”see” the different boundary conditions at the edge of the numerical box.

4.3 Free Time Evolution over τ instead of $\tau - \tau_p$

As for the QKR, there are two ways in which we can define the fulfillment of the resonance (antiresonance) condition: either we let the system evolve freely over time periods $\tau_1 - \tau_{p,1}$ and $\tau_2 - \tau_{p,2}$ after the respective kicks, or we let it evolve over τ_1 and τ_2. The figures shown so far, are all generated in the first case. We now show the pictures for a free time evolution over τ_i.
The pictures have all been generated under the same choice of parameters as before with the only two differences being the Hamiltonian that is changed to $H_{free} = e^{-i\frac{n^2}{2}(\tau-\tau_p)} \longmapsto H_{free} = e^{-i\frac{n^2}{2}\tau}$ and an adapted kicking duration $\tau_{p,i}$. It showed that the system is much more sensitive to the finite kicking duration, in a way that we see significant changes in the spectrum around an order of 10 earlier than in the case of the free time evolution over $\tau_i - \tau_{p,i}$: Before, the differences were highly visible for $\tau_{p,i} = 10^{-2}$; now they are already relevant for $\tau_{p,i} = 10^{-3}$. Therefore, the following figures are all created under a finite kicking duration of $\tau_{p,i} = 10^{-3}$.

Resonance The first main difference we see is in the spectrum plotted against the index: Under finite kicking duration, the energy bands acquire a strong curvature. In an attempt to understand this, one can look at the tight-binding model. There the solution to the simple next-neighbor interaction Hamiltonian is a cosine. The spectrum under finite kicking duration here looks like a combination of different cosine solutions. One attempt at an explanation is that the soft wall that arises causes the plane wave solutions to reflect. Therefore, instead of the one plane wave solution that leads to the cosine solution of the tight-binding Hamiltonian, we have several interfering plane waves that together lead to the superposition of several cosine solutions. Together those solutions create the form of the energy bands we see in Fig. 19a.

The first thing we see in the MCD under the adjusted free time evolution is, that the MCD under a finite kick deviates from that under an infinitesimal kick around the values of k_2 where the winding number has a "step". However, the MCD is almost identical even for large k_2 under finite kicking for both BCs. Additionally, we again see that the MCD under PBCs differs from that under OBCs significantly for $k_2 \gtrsim 1.5\pi$ for infinitesimal kicks. Together that means, the finite kick in combination with periodic boundary conditions leads to a MCD that matches that under OBCs better than that under PBCs with infinitesimal kicking. Therefore, if one would again try to predict the number of degenerate edge states based on the numerical results for the MCD, the error that one would make under the ideal case of PBCs with infinitesimal kicks or under a finite kick with a free time evolution over $\tau - \tau_p$ - see discussion in sec. 4.1 - would be compensated by the introduction of a finite kick and time evolution over τ (see Fig. 19b). However, the MCD is only a good prediction for the winding number around the middle between the kicking strengths k_2, where a topological phase transition takes place (e.g. at $k_2 = 1.5\pi$, that is far enough from $k_2 = \pi$ and $k_2 = 2\pi$).

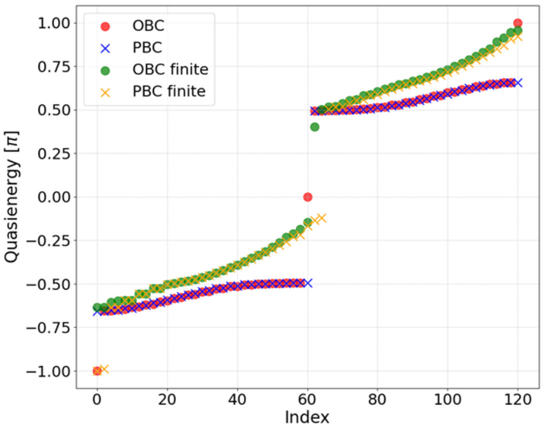

(a) Quasienergy spectrum at $k_2 = 1.5\pi$ in resonance with a free time evolution over $\tau_{1,2}$.
As expected, the qualitative and quantitative shape of the spectra under infinitesimal kicking duration do not change. For a finite kicking duration of $\tau_{p,i} = 10^{-3}$, the energy-bands acquire stronger curvature.

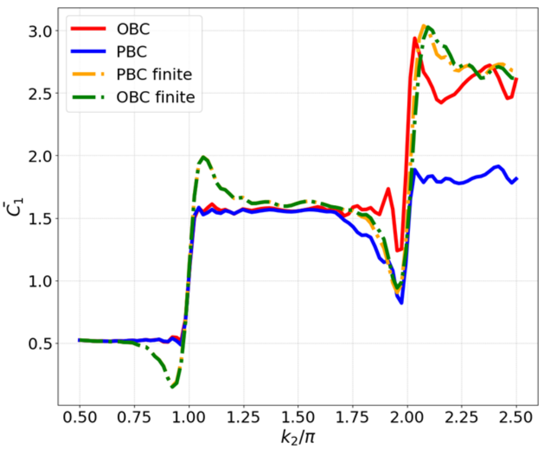

(b) MCD for $k_2 = 1.5\pi$ and $t = 15$ in resonance with a free time evolution over $\tau_{1,2}$.
The MCD under finite kicking almost matches that under OBCs with infinitesimal kicking duration, even for periodic BCs.

Figure 19: Quasienergy spectrum and MCD in resonance for a free time evolution over τ_i. The chosen parameters are $k_2 = 1.5\pi$ in the left picture; $n_{max} = 30$, $\tau_{p,i} = 10^{-3}$.
We see a quantitatively different behavior for both the spectrum and the MCD when compared to the results under a free-time evolution over $\tau_i - \tau_{p,i}$ (cf. Fig.s 14a and 15).

Antiresonance The spectra of the DKRS in the antiresonant case can be explained based on the previous discussions. Periodic BCs (infinitesimal τ_p) give rise to "deviating" energies. Additionally, the finite kicking duration causes the formerly flat energy bands to acquire negative curvature (see Fig. 20a).

The form of the energy bands now is strongly reminiscent of a cosine form. This can be explained by the following: in antiresonance, ideally every second kick destroys the effect of the preceding one. This has the effect, that we now do not have the superposition of many plane waves that each have a cosine solution, but we only have two superposed plane waves with cosine tight-binding solutions, which finally leads to the form of the curved energy bands under finite kicking duration.
The MCD on the other hand, displays the same values for all combinations of boundary conditions (see Fig. 18). Only at very strong kicking $k_2 \approx 2.5\pi$, the MCD under finite kicks marginally deviates from that under infinitesimal kicking duration. We can argue that for such k_2, the tiny difference to the ideal antiresonance condition leads to the system slightly expanding in momentum space. Then, an asymmetry in the momentum distribution on the left and right of the central momentum can accumulate, such that the MCD under finite kicks does not match that under infinitesimal kicking duration identically anymore. However, as we do not have a theory on how the MCD behaves in the antiresonant case, it is hard to argue why we see this exact profile of the MCD. The motivation for the MCD was that it converges to half the winding number in the resonant case. The winding number then gives us the connection from the MCD as the numerical observable to the physical reality that open boundary conditions lead to the emergence of a discrete number of degenerate edge states, which are completely characterized by the set of winding numbers. For the antiresonant case, we do not know about such a connection between the MCD and the topological properties of the system. The only knowledge we have about the MCD is its form in the case of a free time-evolution over $\tau_i - \tau_{p,i}$ (Fig. 18). Comparing both figures, we see that the MCD is identical. This makes sense because, once again, the system is staying close to the initial momentum class and does not interact with the edge of the momentum basis.

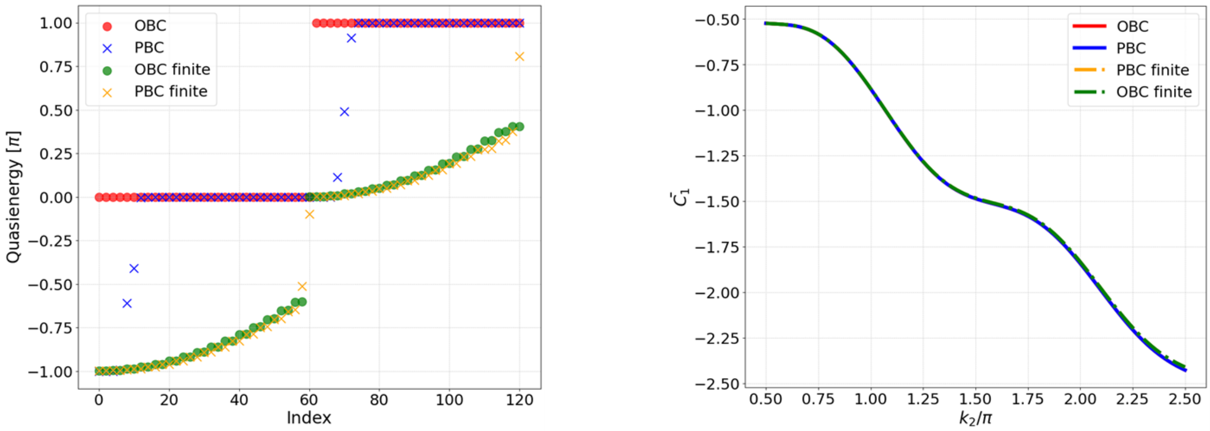

(a) Quasienergy spectrum at $k_2 = 1.5\pi$ in antiresonance with a free-time evolution over $\tau_{1,2} = 10^{-3}$. The energy bands for finite kicking duration that were completely flat before, now display a negative curvature that is reminiscent of a cosine form. There is a number of discrete quasienergies that do not follow the overall band structure under periodic boundary conditions and finite kicking duration.

(b) MCD for $k_2 = 1.5\pi$ and $t = 15$ in antiresonance with a free-time evolution over $\tau_{1,2} = 10^{-3}$. The MCD is almost the same for all used boundary conditions. Only for large k_2 the MCD under finite τ_p marginally deviates from that for $\tau_p = 0$. Overall, the MCD displays the same qualitatively and quantitative behavior as in the antiresonant case for a free time evolution over $\tau_i - \tau_{p,i}$.

Figure 20: Quasienergy spectrum and MCD in antiresonance for a free time evolution over τ_i. The used parameters are $k_2 = 1.5\pi$ in the left picture; $n_{max} = 30$, $\tau_{p,i} = 10^{-3}$.
The quasienergy spectra under finite kicking durations display curved bands instead of flat bands. The combination of periodic BCs together with finite kicking leads to a discrete number of quasienergies that do not follow a band-structure as before. The MCD overall shows the same shape for all combinations of boundary conditions and kicking durations.

5 Conclusion

Within this thesis, we studied two Kicked Rotor Models: the Quantum Kicked Rotor and the Spin-1/2 Double Kicked Rotor. We had three central questions we strove to answer in the course of this work. Firstly, we wanted to study how the dynamics and spectra of both models behaved under the influence of different boundary conditions. The boundary conditions we considered were open (hard wall) and periodic boundaries. For both, we assumed an infinitesimally short as well as a finite kicking duration. The second topic of interest was to understand the bulk-edge correspondence, given in the topological extension due to the internal spin degree of freedom in the DKRS. Thirdly, we wanted to test whether the proposed experimental observable, the MCD, is still a meaningful quantity under the different boundary conditions. Lastly, we want to comment on the hypothesis whether one can intentionally use a finite kicking duration to mimic periodic boundary conditions in experimental realizations.

QKR The dynamics, studied in form of the probability distribution and averaged energy, behave the same under all BCs. The differences due to the implementation of a finite kicking duration lead only to insignificant variances. The investigation of the spectra however, showed some novel insights: for the antiresonant case, we find that under periodic BCs, there are discrete quasienergies that take values different from the otherwise flat energies at $\epsilon = 0, \pm\pi$. We showed that these points are the result of the localization of the otherwise plane waves at the edges of the momentum basis. In the resonant case, the examination of the spectrum is not as simple. Here, we only see differences in the spectra under the different BCs, when we chose a short momentum basis. Then, one sees, that the quasienergies deviated pairwise from the corresponding ones under different BCs. However, the cause of this effect lies rather in the numerical imprecision and the quantization of the position and momentum basis, than in the influence of the boundary conditions.

DKRS For the DKRS, we only examined the spectra and the Mean Chiral Displacement. Motivated by experimental realizations, we specifically studied the resonant case. We can confirm the bulk-edge correspondence described by Zhou & Gong in [5]. Additionally, we conclude that it still holds under the implementation of a finite kicking duration. Moreover, we showed that the edge states under OBCs are corresponding to eigenvectors that localize at the edges of the momentum basis. In the case of finite kicking together with periodic BCs, one has to be careful, as the quasienergy spectrum shows the effect of the deviating quasienergies due to the PBCs, which are however not topological edge states. Still, the eigenvectors corresponding to those deviating quasienergies localize at the edge of the numerical box. For a free time evolution over $\tau - \tau_p$, the MCD is only able to predict the number of edge states accurately under OBCs. Under PBCs, it deviates significantly from the theoretical prediction. However, this means that we can use the MCD to determine whether the system is subject to open or periodic boundary conditions.
In antiresonance, we see the same qualitative behavior as for the QKR. There, the MCD does not show a significant distinction for the different BCs.

Time Period of Free Evolution Lastly, for both models, we performed the examinations in two different interpretations of the resonance and antiresonance condition. The different interpretations arise when implementing the finite kicking duration. Firstly, we defined the long free-time evolution to be over $\tau - \tau_p$ (for the DKRS analogously $\tau_i - \tau_{p,i}$). In a second pass, we then defined the time period to be τ. The second method showed three main differences. For once, the spectra and dynamics were a factor $10 - 100$ of the kicking duration more sensitive to the kicking duration. Secondly, the curvature of the quasienergy bands in both models increased. Lastly, under a free time evolution over τ instead of

$\tau - \tau_p$, the combination of periodic BCs with the finite kick lead to a MCD that agrees to the theoretical prediction we can make based on the bulk-edge correspondence.

Finite Kicking Duration for PBCs Overall, we could not confirm the hypothesis that a finite kicking duration could be used intentionally for the purpose of experimentally realizing periodic boundary conditions. The spectra always show similar behavior under open and periodic boundary conditions and finite kicks.

The only exception to this is the MCD under PBCs with a finite kick in combination with a free time evolution over $\tau - \tau_p$. There, the MCD takes the same value for the different boundary conditions for a free time evolution over τ and finite kicking durations.

However, one should test the hypothesis in a systematic way to either prove it or rule it out completely.

6 Outlook

In the course of this thesis, we examined the most simple cases of resonance and antiresonance of the QKR and DKRS. However, [1] gives a much more general condition that allows for higher order resonances. The behavior of the two Kicked Rotor Systems under those resonances and different boundary conditions is yet to be studied.

In 2015, J. Floß and I. S. Averbukh presented the edge localization in angular momentum space for periodically kicked three-dimensional rotors [29]. Their model, using molecules, has an actual realization of hard wall boundary conditions. However, their studies focused on the third order resonance with a kicking period of $\tau = \frac{t_{rev}}{3}$ (with t_{rev} the revival time). They observed that for a fractional resonance $\tau = \left(\frac{p}{q}\right)t_{rev}$, the quasienergy spectrum consists of up to q bands that broaden when increasing the kicking strength. Yet, they could not find a rule for the number of edge states.

Based on this, it could be of particular interest to test the bulk-edge-correspondence and the connection between the MCD $C_l(t)$ and the pair of winding numbers (ν_0, ν_π) for fractional resonances of the DKRS as well. A promising goal would be to try and draw a connection between the findings on 3D kicked rotor systems and the DKRS.

Recently (2023), V. Karle et al. proposed another experimental realization of periodically kicked molecules [30], where they showed, that the localized edge states are topologically protected. The novelty of their work was that they could connect it directly to condensed matter systems by introducing quasimomenta of periodically driven molecular states. One could try and perform an analysis similar to theirs on the DKRS.

Another question that could not be answered in this study is, how we can experimentally realize periodic boundary conditions. The hypothesis was, that tuning the finite kicking duration of a Kicked Rotor Model might reproduce the conditions of periodicity. The motivation of this idea is, that the finite kicking duration has shown to introduce a "soft wall" in momentum space, at which the wave function of the system reflects. However, our results did not show that the combination of open boundary conditions with a selected finite kicking duration reproduced the same spectra and dynamics under periodic boundary conditions. One could try to find a specific choice of the kicking duration by systematically varying τ_p and comparing the spectral properties.

A Derivations and Mathematical Formulation

A.1 Full Derivation of the Energy in the Resonant QKR

The energy $E(t)$ of the system can be calculated via the expected value of the kinetic energy operator $E(t) = \langle\psi|\, T\, |\psi\rangle$ with $T = -\frac{1}{2}\frac{\partial^2}{\partial\theta^2}$. We write the time in terms of the period τ: $t = s \cdot \tau$.

$$\begin{aligned}
E(t) &= E(s\cdot\tau) && (47)\\
&= \langle\psi(s\cdot\tau)| - \frac{1}{2}\frac{\partial^2}{\partial\theta^2}\,|\psi(s\cdot\tau)\rangle && (48)\\
&= \langle\psi(0,\theta)\,\hat{U}^\dagger(s\cdot\tau)| - \frac{1}{2}\frac{\partial^2}{\partial\theta^2}\,|\hat{U}(s\cdot\tau)\,\psi(0,\theta)\rangle && (49)\\
&= \langle\psi(0,\theta)\,(\hat{U}^\dagger)^s(\tau)| - \frac{1}{2}\frac{\partial^2}{\partial\theta^2}\,|(\hat{U}(\tau))^s\,\psi(0,\theta)\rangle\,, && (50)
\end{aligned}$$

where we used that we can write the Floquet-Operator for $s\cdot\tau$ as a product of s time evolutions with τ in the last step. Now, we can use the explicit form of the Floquet-Operator in resonance $\hat{U}_{\tau=4\pi} = e^{-i\,k\,\cos(\theta)}$. Plugging in the form of the initial wave function $\psi(0,\theta) = \frac{1}{\sqrt{2\pi}}e^{-ip_0\theta}$ and approximating the sum over all θ as an integral over θ, we get

$$E(t) = -\frac{1}{2}\int_0^{2\pi} d\theta\,\frac{1}{2\pi}\,e^{ip_0\theta}(e^{i\,k\,\cos(\theta)})^s\,\frac{\partial^2}{\partial\theta^2}(e^{-i\,k\,\cos(\theta)})^s e^{-ip_0\theta} \tag{51}$$

Calculating the second derivative w.r.t. θ and combining the exponentials leaves us with

$$\begin{aligned}
E(s\cdot\tau) &= -\frac{1}{2\cdot 2\pi}\int_0^{2\pi} d\theta\,[p - k\,s\,\sin(\theta)]^2 - i\,k\,s\,\cos(\theta) && (52)\\
&= \frac{1}{4\pi}\int_0^{2\pi} d\theta\,p^2 + k^2\,s^2\,\sin(\theta)^2 && (53)\\
&= \frac{1}{4\pi}\cdot[2\pi\,p^2 + \pi\,k^2\,s^2] && (54)\\
&= \frac{p^2}{2} + \frac{k^2\,s^2}{4} && (55)
\end{aligned}$$

For the integration of the trigonometric functions, their symmetry in combination with the integration interval was used:

$$\begin{aligned}
\int_0^{2\pi} d\theta\,\cos(\theta) &= 0\\
\int_0^{2\pi} d\theta\,\sin(\theta) &= 0\\
\int_0^{2\pi} d\theta\,\sin(\theta)^2 &= \pi
\end{aligned}$$

A.2 Rewriting the Kicking-Operator in Momentum Basis

It has been found that it is beneficial to transform the kick operator $\hat{U}_{kick}$, which is diagonal in the angle basis $\{\theta|\theta \in [0, 2\pi)\}$ but not in the momentum basis $\{n\}$, into the momentum basis. This is due to the fact that we can straightforwardly implement periodic boundary conditions for a closed matrix representation of the total Hamiltonian. The subsequent calculation demonstrates the method by which the kick operator $\hat{U}_{kick}$ can be represented in the momentum basis. The inspiration for this reformulation is drawn from section 3.C of [5].

The kick operator is given by

$$\hat{U}_{kick} = e^{-i\,k\,\cos(\hat{\theta})} \tag{56}$$

Firstly, the alternative expression of the cosine is used:

$$\cos\left(\hat{\theta}\right) = \sum_{\hat{\theta}} \frac{e^{i\hat{\theta}} + e^{-i\hat{\theta}}}{2} \left|\theta\right\rangle \left\langle\theta\right| \tag{57}$$

We know that the position and momentum basis are connected via a Fourier Transformation:

$$\langle\theta|n\rangle = \frac{1}{\sqrt{2\pi}} e^{i\theta n} \tag{58}$$

That means we can perform a Fourier Transformation from position to momentum representation

$$\left|\theta\right\rangle = \sum_{n=-\infty}^{\infty} e^{i\hat{n}\hat{\theta}} \left|n\right\rangle \tag{59}$$

Under periodic boundary conditions, this can also be written as

$$\left|\theta\right\rangle = \frac{1}{\sqrt{N}} \sum_{n=-\frac{N}{2}}^{\frac{N}{2}-1} e^{in\theta} \left|n\right\rangle \tag{60}$$

From this follows

$$\begin{aligned}
cos(\hat{\theta}) &= \sum_{\theta} \frac{e^{i\theta} + e^{-i\theta}}{2} \left|\theta\right\rangle \left\langle\theta\right| && (61)\\
&= \sum_{\theta} \sum_{n,\,m} \left(\frac{e^{i\theta} + e^{-i\theta}}{2}\right) \cdot e^{in\theta} \left|n\right\rangle e^{-im\theta} \left\langle m\right| && (62)\\
&= \sum_{\theta} \sum_{n,\,m} \left(\frac{e^{i\theta} + e^{-i\theta}}{2}\right) \cdot e^{i\theta(n-m)} \left|n\right\rangle \left\langle m\right| && (63)\\
&= \sum_{\theta} \sum_{n,\,m} \frac{e^{i\theta(n-m+1)} + e^{-i\theta(m-n+1)}}{2} \left|n\right\rangle \left\langle m\right| && (64)\\
&= \frac{1}{2} \sum_{n\,m} (\delta_{m,\,n+1} + \delta_{m+1,\,n}) \left|n\right\rangle \left\langle m\right| && (65)\\
&= \frac{1}{2} \sum_{n} \left|n\right\rangle \left\langle n+1\right| + \left|n+1\right\rangle \left\langle n\right| && (66)
\end{aligned}$$

Where we used from the third to second last step

$$\sum_{\hat{\theta}} e^{i\hat{\theta}(x-y)} = \delta_{x,\,y} \tag{67}$$

The derivation is analogous in the case of PBCs, using the fact

$$\frac{1}{N} \sum_{\hat{\theta}} e^{i\hat{\theta}(x-y)} = \delta_{x,\,y} \tag{68}$$

as we take into account that number of values θ can take equals the number of different momenta N. Using this instead of (67), we get the same result.

B Study of the QKR

B.1 Discrepancy between the Averaged Energy under OBCs and PBCs

We saw in Fig. 7b that the averaged energy under OBCs is always higher than under PBCs. We argued that this discrepancy is caused by the fact that under PBCs, the length of the momentum basis is effectively reduced by one, compared to that under OBCs. To test this statement, we again calculate the averaged energy, now with $n_{max} = 16$ instead of $n_{max} = 15$. Additionally, we take away the lowest momentum class, s.t. the momentum array is given by $n \in [-15, -14, ..., 14, 15, 16]$. For this, the length of the momentum array is $N = 32$, but for PBCs effectively $N_{PBC} = 31$ (under the choice of $n_{max} = 16$). So then, for $n_{max} = 15$ we have $N = 31$ and for PBCs effectively $N = 30$. For $n_{max} = 16$ and by cutting out the lowest momentum class, we have $N = 32$ for OBCs and $N_{PBC} = 31$ for PBCs. We now plot the averaged energy. It should be noted, that we only considered the case of an infinitesimal kick. However, this is sufficient for the validation of our argument.

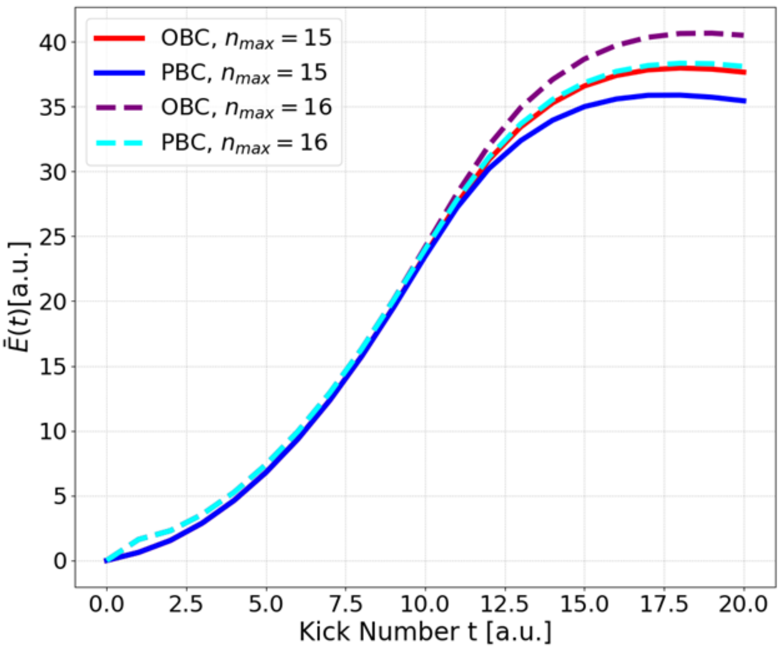

Figure 21: Comparison of the averaged energy under different lengths of the momentum basis. The colors are chosen as labeled in the legend. Note that the length of the momentum basis is only one greater for $n_{max} = 16$ compared to $n_{max} = 15$ and not two, as we manipulated the momentum array. We see that $\bar{E}(t)$ is almost identical for OBCs with $n_{max} = 15$ and PBCs with $n_{max} = 16$.

We see that for the adjusted momentum basis, the averaged energy under PBCs (cyan) almost identically matches that under OBCs (red) with the non-manipulated momentum basis. This underlines our argument that the discrepancy in the averaged energy between OBCs and PBCs is caused by the effect that PBCs take away one momentum class by identifying $+n_{max}$ with the momentum class $-n_{max}$.
We see a slight kink of the averaged energy in the manipulated momentum basis for small kick numbers t. This is caused by the fact that taking away the lowest momentum class $-n_{max} = -16$ makes the momentum array asymmetrical. This effect becomes insignificant for larger kick numbers t.

B.2 Testing for a Localization of the Eigenvectors at n_L

Trying to understand the influence of the soft wall on the spectrum of the QKR (in the antiresonant case), we want to test for localization of eigenvectors at the position of the soft wall n_L. To check whether we see a direct localization effect in momentum space at the previously calculated n_L, we can calculate those eigenvectors that have a maximum occupation probability in the momenta classes around n_L. We determine the first five eigenvalues with the highest sum of occupation probability in the momentum classes $n_L = [15, ..., 20]$.

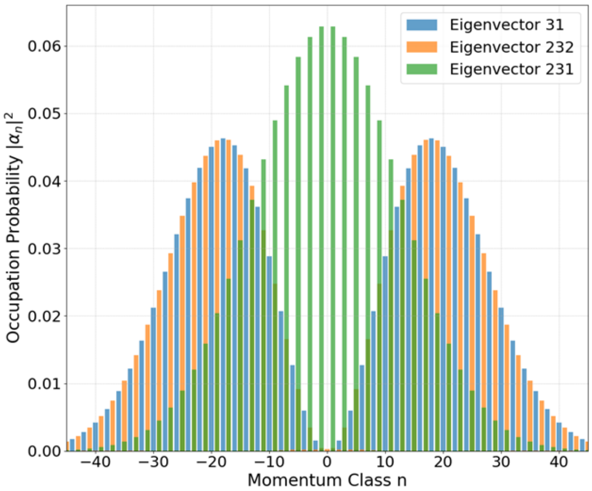

(a) Maximization of the occupation probability $|\alpha_n|^2$ at the momentum classes $n_L = [15, ..., 20]$ under $\tau_p = 10^{-2}$ and open boundary conditions of the antiresonant QKR. We see that there is no eigenvector that localizes around n_L. All pictured eigenvectors still show the structure of a plane wave.

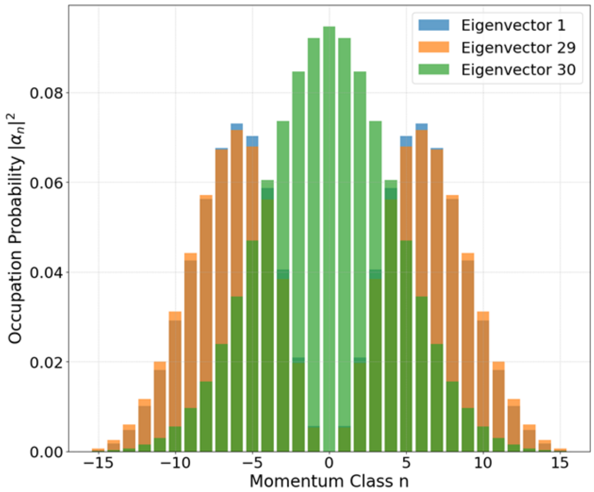

(b) Maximization of the occupation probability $|\alpha_n|^2$ at the momentum classes $n_L = [4, ..., 7]$ under $\tau_p = 10^{-1}$ and open boundary conditions of the resonant QKR. Again, there is no localization of the eigenvectors. They are plane waves.

Figure 22: Investigation of localization of eigenvectors at the position of the soft wall n_L in the antiresonant (left) and resonant case(right) of the QKR. The occupation probability $|\alpha_n|^2$ is maximized in an interval around n_L. Both plots are acquired under OBCs with finite kicking duration. All other BCs lead to the same qualitative result.

However, we do not see any localization of eigenvectors around the momentum classes n_L where the soft wall should be positioned. Therefore, we cannot confirm our hypothesis, that the two quasienergies at $\tau_p = 10^{-2}$ (and $\tau_p = 10^{-1}$) are caused by their eigenvectors (wave functions) localizing at the soft wall in momentum space.
A similar study has been performed in the resonant case with adapted parameters, see Fig. 22b. The result was the same: no localization at the momenta classes n_L could be found.
The above pictures (Fig. 22) were acquired under OBCs with finite kicking duration. The same study under the other boundary conditions gave the same qualitative result.

B.3 Study of the Occupation Probability Distribution of the Eigenvectors in the Resonant Case of the QKR

As explained in section 3.2.2, in the resonant case it might be of interest to take a look at the distribution of the occupation probability of those eigenvectors with the highest overlap at the edges of the momentum basis.
Here, we want to show the distributions for periodic boundary conditions under infinitesimal kicking duration as well as $\tau_p = 10^{-1}$ for the three eigenvectors with the highest occupation probability at $n = 15$.

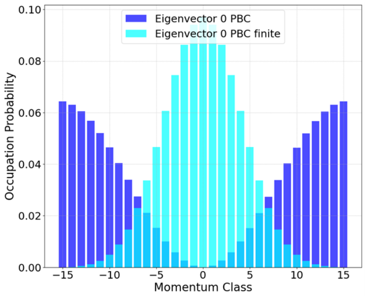

(a) Maximization $|\alpha_{15}|^2$ PBC Infinitesimal - Highest Occ. Prob.

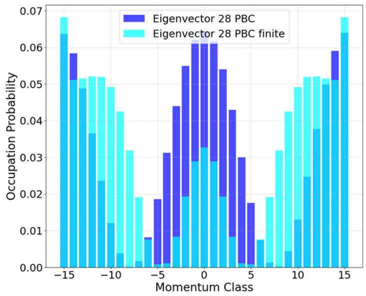

(b) Maximization $|\alpha_{15}|^2$ PBC Infinitesimal - Second Highest Occ. Prob.

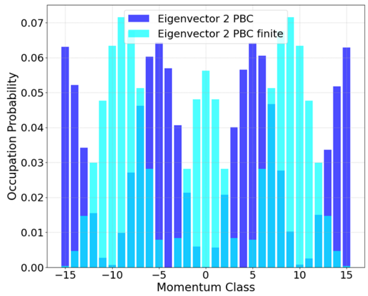

(c) Maximization $|\alpha_{15}|^2$ PBC Infinitesimal - Third Highest Occ. Prob.

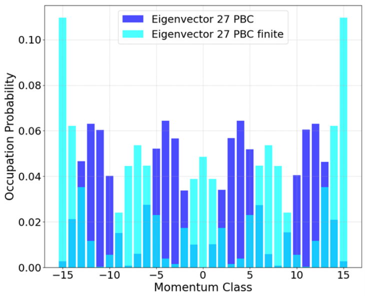

(d) Maximization $|\alpha_{15}|^2$ PBC finite $\tau_p = 10^{-1}$ - Highest Occ. Prob.

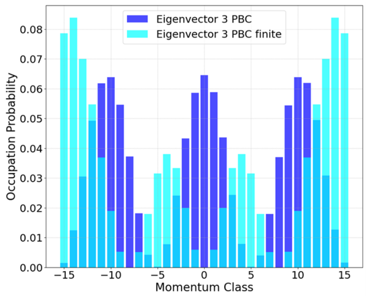

(e) Maximization $|\alpha_{15}|^2$ PBC finite $\tau_p = 10^{-1}$ - Second Highest Occ. Prob.

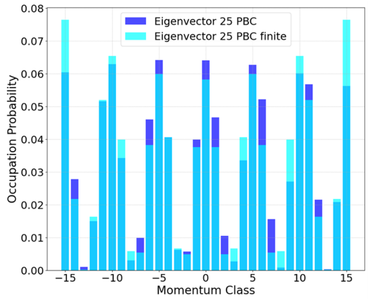

(f) Maximization $|\alpha_{15}|^2$ PBC finite $\tau_p = 10^{-1}$ - Third Highest Occ. Prob.

Figure 23: Comparison of the eigenvectors under PBCs with the highest occupation probability in the edge momentum classes. Periodic boundary conditions with infinitesimal kicking duration are shown in blue; PBCs with $\tau_p = 10^{-1}$ are plotted in cyan. For the upper row the occupation probabilities at n = 15 for PBCs under infinitesimal τ_p were maximized. In the lower row, $|\alpha_n|^2$ was maximized for the eigenvectors under PBCs and $\tau_p = 10^{-1}$. We see that the eigenvectors are plane waves. In the infinitesimal case, their amplitudes stay constant while for $\tau_p = 10^{-1}$, the amplitudes are changing. We do not see a clear localization of the eigenvectors; they all still have plane-wave structure.

The first thing we see is that the number (index) of the eigenvectors is not the same under infinitesimal and finite kicking duration. That means the eigenvectors belong to different quasienergies in the spectrum. Secondly, we notice that under infinitesimal τ_p, the distributions show plane waves with constant amplitude. For $\tau_p = 10^{-1}$, the distribution still shows periodic waves but now with changing amplitudes.
We do not see a localization like we did in the antiresonant case (see Fig.s 11 and 26). In general, we cannot determine any structure of the eigenvectors occupying the outermost momenta classes.

One can also investigate the eigenvector occupation distributions for the case of open boundary conditions to get a general feeling on how the implementation of a finite kicking duration influences the eigenvectors. We do this for two cases: firstly, we plot some eigenvectors for the parameters we used in the third section ($\tau_p = 10^{-1}$, $n_{max} = 15$). Secondly, to get a more general picture, we also plot the eigenvector occupation distributions for the case of a large n_{max} (parameters: $\tau_p = 10^{-2}$, $n_{max} = 100$).
Comparing the eigenvectors shows the same behavior as for PBCs:

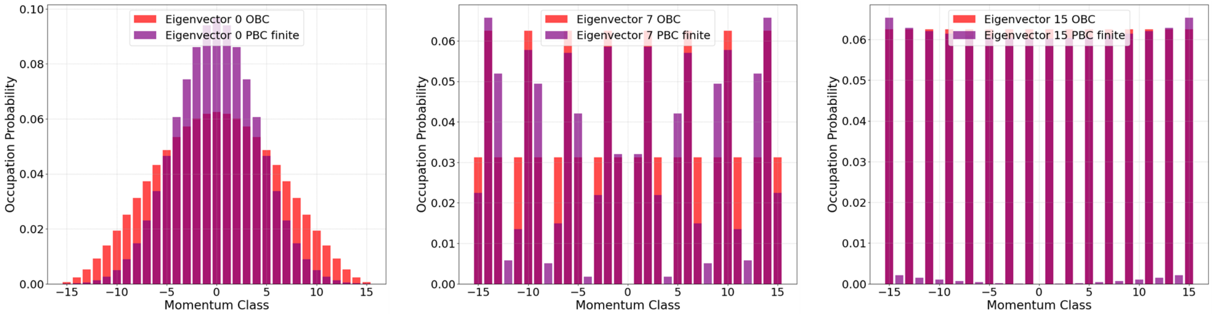

(a) Occup. Prob. Distrib. for the eigenvector 0 and OBCs.

(b) Occup. Prob. Distrib. for the eigenvector 7 and OBCs.

(c) Occup. Prob. Distrib. for the eigenvector 15 and OBCs.

Figure 24: Comparison of the eigenvector distribution against the momentum classes n under OBCs. The basis has maximum momentum class $n_{max} = 15$. We plot the eigenvectors 0, 7 and 15. Open boundary conditions with infinitesimal kicking duration are shown in red; OBCs with $\tau_p = 10^{-2}$ are plotted in purple.

We see here, that for the low index (eigenvector 0), the distribution is a plane wave in momentum space. Whether the kicking duration is finite or not influences the magnitude of the occupation probabilities. However, the distributions still are qualitatively similar. The eigenvectors 7 and 15 show distributions that do not directly look like plane wave solutions. However, again, the duration of the kick does not seem to be too relevant for the distributions. This fits our results from section 3 - the quasienergies are almost identical under infinitesimal and finite τ_p.

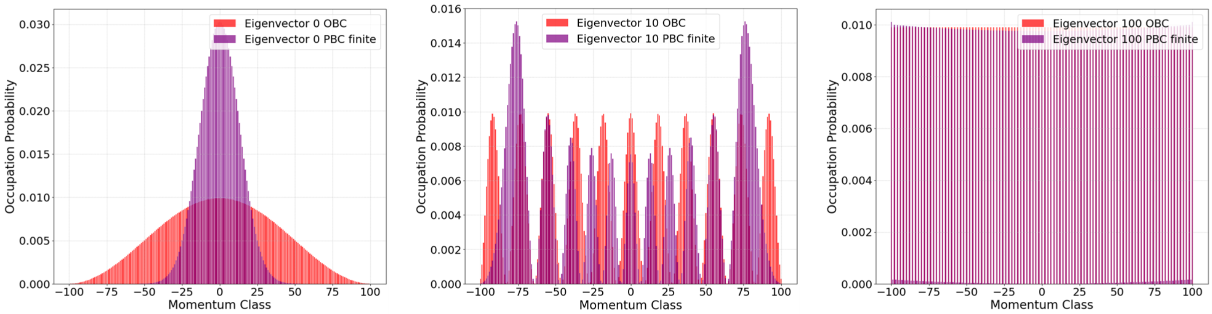

(a) Occup. Prob. Distrib. for the eigenvector 0 and OBCs.

(b) Occup. Prob. Distrib. for the eigenvector 10 and OBCs.

(c) Occup. Prob. Distrib. for the eigenvector 100 and OBCs.

Figure 25: Comparison of the eigenvector distribution against the momentum classes n under OBCs. The basis has maximum momentum class $n_{max} = 100$. We plot the eigenvectors No. 0, 10 and 100. Open boundary conditions with infinitesimal kicking duration are shown in red; OBCs with $\tau_p = 10^{-2}$ are plotted in purple.

Plotting the occupation probability distribution for the eigenvectors of the resonant QKR with a basislength of $n_{max} = 100$ shows the following: both eigenvectors No. 0 are plane waves. However, their amplitudes and spreading in the momentum space differ significantly. For an infinitesimal kicking duration, the amplitude is much less focused around $n = 0$ compared to the case of finite τ_p, but spreads out to more momentum classes, almost up to $|n| = 100$. The eigenvectors No. 10 again both show plane waves. Yet, while the amplitude under infinitesimal kicking stays the same along the wave, for the finite case, the amplitude increases around higher absolute momenta $|n|$. Finally, eigenvector No. 100 shows an almost flat distribution of the occupation probabilities. The distributions do not differ much between infinitesimal and finite kicking; for finite kicking, the amplitudes are slightly growing towards larger $|n|$, while for infinitesimal τ_p the are the same along all momenta classes.
However, considering that the quasienergy-spectrum was about the same for both the infinitesimal and

the finite case, the differences in the occupation probability distributions do not seem to influence the corresponding eigenvalues, that is the quasienergies, much.

B.4 Deviating Spectrum under the FFT-Method

Using the FFT-Method, explained in section 2.4, we also find deviating points in the spectrum. The number and position of the deviations match those under periodic boundary conditions and the matrix method (compare Fig.s 11 and 26). The investigation of the eigenvector distribution confirms this. The result should not be surprising. After all, the FFT method implicitly assumes that our system is subject to periodicity.

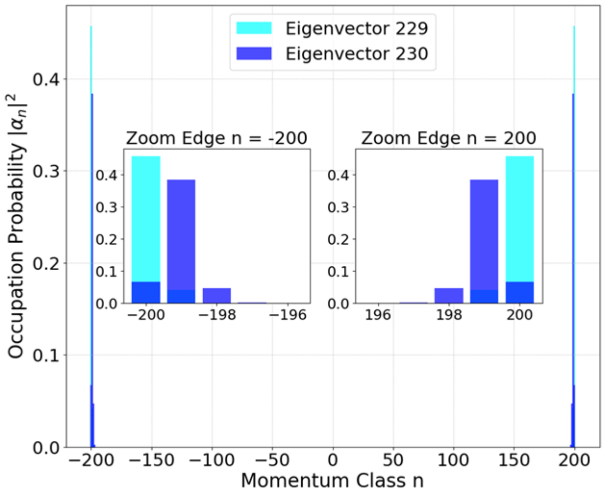

Figure 26: Occupation probability $|\alpha_n|^2$ of the momenta classes n for the eigenvectors of the deviating quasienergies under the FFT-method and a finite kick duration of $\tau_p = 10^{-2}$.
Comparing the distribution of the occupation probability of the eigenvectors for the PBC under the matrix-method and under the FFT-method, both show the exact same eigenvectors with the same occupation probabilities. The eigenvectors localize around the edges of the momentum basis.

B.5 Comparison Eigenvectors 28, 29 and 229, 230 PBC finite

As mentioned in section three, we have a total of four quasienergies in the antiresonant QKR under finite kicking duration and PBCs that are not taking the values $\epsilon = 0, \pm\pi$. In the main part, we showed only the occupation probability distributions $|\alpha_n|^2$ for the eigenvectors No. 229 and 230, belonging to the quasienergies with indices 229 and 230. We argued that the quasienergy-spectrum has to be symmetric around $\epsilon = 0$ due to the symmetry of the Floquet operator. To confirm this, we here show the comparison of the eigenvector distributions between eigenvector No. 28 and 230, and No. 29 and 229, respectively.

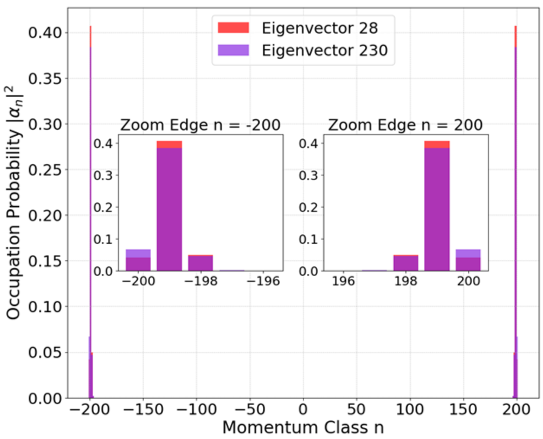

(a) Comparison of the occupation probabilities $|\alpha_n|^2$ for eigenvector 28 and 230. The parameters for the QKR are $n_{max} = 200$, $\tau = 2\pi$ (antiresonance), and $\tau_p = 10^{-2}$. We see that the distributions almost match identically.

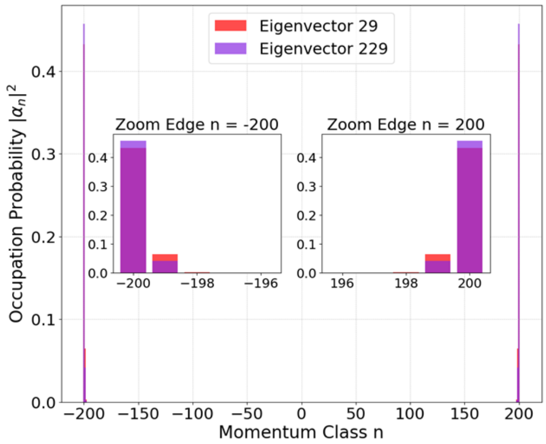

(b) Comparison of the occupation probabilities $|\alpha_n|^2$ for eigenvector 29 and 229. The parameters for the QKR are $n_{max} = 200$, $\tau = 2\pi$ (antiresonance), and $\tau_p = 10^{-2}$. We see that the distributions almost match identically.

Figure 27: Comparison of the occupation probabilities $|\alpha_n|^2$ of the momenta classes n for the eigenvectors of the deviating quasienergies under PBCs and finite kicking duration of $\tau_p = 10^{-2}$.

The slight mismatch of the occupation probabilities is most probable just a numerical artifact caused by the discretization of the system. Overall, the symmetry of the quasienergy spectrum around $\epsilon = 0$ is obeyed.

B.6 Probability Distribution and Averaged Energy for a Free-Time Evolution over τ

In section 3.3 we showed the Floquet spectra under a free-time evolution over τ instead of $\tau - \tau_p$ for both the resonant and the antiresonant case. We had two main findings: the spectra were a factor 10 more sensitive to the kicking duration τ_p and the quasienergy-bands acquired curvature.
Now, we want to show the probability distributions and time-averaged energies for the adjusted evolution time as well.
Starting with the antiresonant case, we see that the probability distribution for a finite kicking duration is slightly wider than that under infinitesimal kicking (Fig. 28a). However, the averaged energy is the same under all combinations of boundary conditions and kicking durations (Fig. 28b).

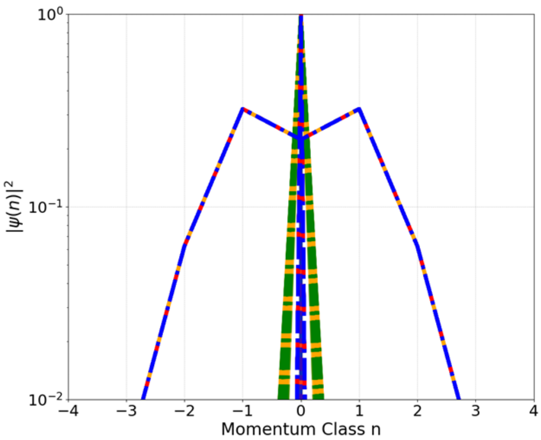

(a) Probability distribution of the antiresonant QKR under a free-time evolution over τ. The colors are chosen in accordance to Fig. 28b.
Under finite kicking, the probability distribution is slightly wider around the central momentum class $n = 0$.

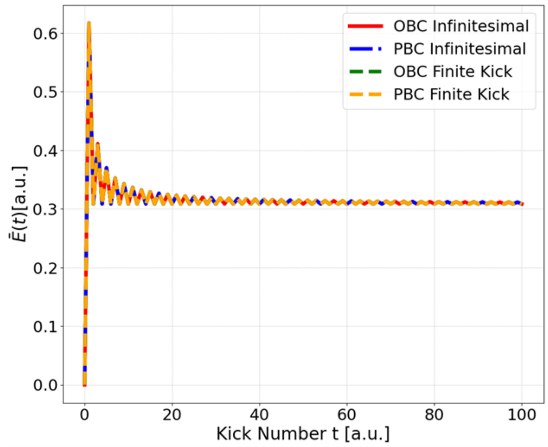

(b) Averaged energy $\bar{E}(t)$ of the antiresonant QKR under a free-time evolution over τ.
The averaged energy is the same under all combinations of BCs and kicking durations.

Figure 28: Dynamics of the antiresonant QKR under free-time evolution over τ instead of $\tau - \tau_p$. The parameters are $n_{max} = 100$, $\tau = 2\pi$ and $\tau_p = 10^{-4}$.

At resonance, the probability distribution is the same under all BCs until it is reflected at the edge of the numerical box. Then, the probability distributions start to differ. The averaged energies are almost identical for all boundary conditions.

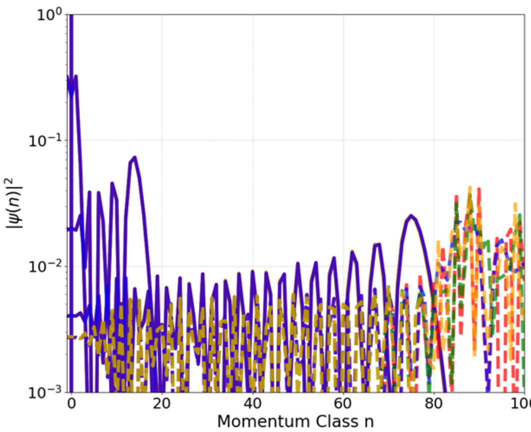

(a) Probability distribution of the resonant QKR under a free-time evolution over τ. The colors are chosen in accordance with Fig. 29b.
Until the system is reflected at the edge of the momentum basis, the probability distribution is identical for all BCs. After reflection, the distributions differ slightly. However, the ballistic structure still remains.

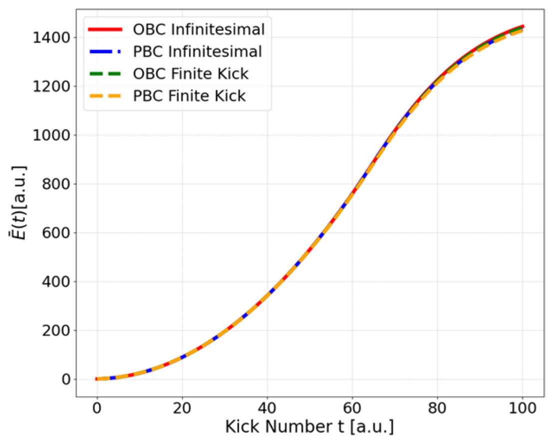

(b) Averaged energy $\bar{E}(t)$ of the antiresonant QKR under a free-time evolution over τ.
The averaged energy is approximately the same under all combinations of BCs and kicking durations.

Figure 29: Dynamics of the resonant QKR under free-time evolution over τ instead of $\tau - \tau_p$. The parameters are $n_{max} = 100$, $\tau = 4\pi$ and $\tau_p = 10^{-4}$.

C Study of the DKRS

C.1 Floquet Spectra of $\hat{U}_{ORDKRS}$, $\hat{U}_{1,ORDKRS}$ and $\hat{U}_{2,ORDKRS}$

As the Floquet operators $\hat{U}_{ORDKRS}$, $\hat{U}_{1,ORDKRS}$ and $\hat{U}_{2,ORDKRS}$ are connected via a unitary transformation, they must have the same quasienergy spectra. We confirmed this numerically, as shown in the following Fig. 30. To generate this plot, we followed the convention of [5] and chose the parameters $n_{max} = 20$, $k_1 = 0.5\pi$ and $k_2 \in [0.5\pi, 2.5\pi]$.

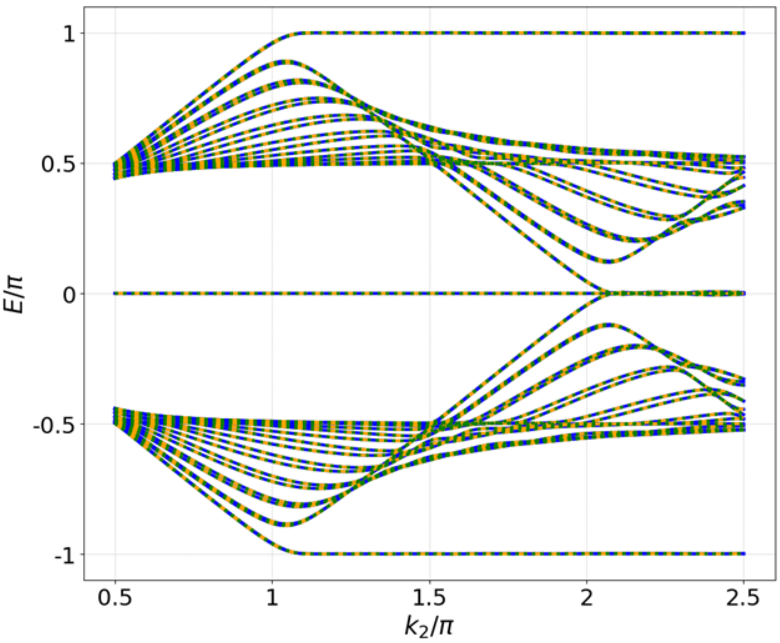

Figure 30: Quasienergy spectra of the Floquet operators U_{ORDKRS} (blue solid line), $U_{1,ORDKRS}$ (orange dashed line) and $U_{2,ORDKRS}$ (green dotted line).
The parameters are $n_{max} = 20$ and $k_1 = 0.5\pi$.
As expected, the spectra are identical independent of the chosen reference frame.

C.2 Choice of t for Studying the MCD

In sec. 4, we saw discrepancies between the MCD under different boundary conditions for $t = 15$ and $k_2 \geq 1.5\pi$. To justify the choice of the number of kicks t, we performed a systematic variation of t with fixed n_{max}. Moreover, we also plotted the MCD for $t = 10$ and stronger kicking k_2.
Doing so, we showed the importance of the choice of t and k_2 for fixed n_{max}: t has to be chosen in a way, such that in the interval of k_2, the rotor evolves so far in momentum space that it interacts with the edge of the numerical box. Only then, the edge of the impulse basis can be resolved, so that we see the influence of the boundary conditions on the MCD.

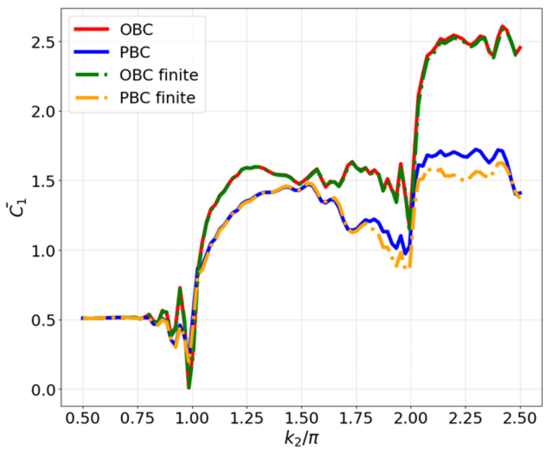

(a) MCD of the resonant DKRS under $t = 20$ and $k_2 \in [0.5\pi, 2.5\pi]$.

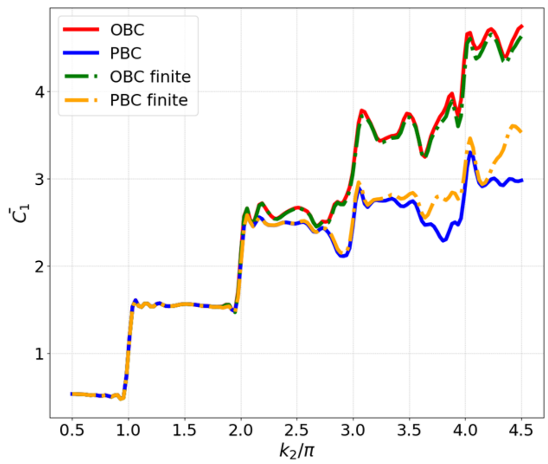

(b) MCD of the resonant DKRS under $t = 10$ and $k_2 \in [0.5\pi, 4.5\pi]$.

Figure 31: MCD of the resonant DKRS with parameters $n_{max} = 30$, $\tau_{p,1/2} = 10^{-2}$, $k_1 = 0.5\pi$. On the left, we choose $t = 20$ instead of $t = 10$, and on the right, we have $t = 10$ and a larger interval for k_2. We see that the choice of both t and k_2 strongly influences the convergence of the MCD to half the winding number.

C.3 Investigation of the Localization of the Edge-States

We already showed in sec. 4, that the edge states in the Floquet spectrum that arise under open boundary conditions localize for a choice of the kicking strength $k_2 = 1.5\pi$. Here, we want to show the figures for the cases of $k_2 = 0.5\pi$ and $k_2 = 2.5\pi$ as well. Especially in the case of $k_2 = 0.5\pi$, we see a very strong localization at the edges of the numerical box. In this case, the combination of a finite kicking duration of $\tau_p = 10^{-2}$ with periodic boundary conditions also does not lead to quasienergies that take values different from the expectation based on the overall band structure.

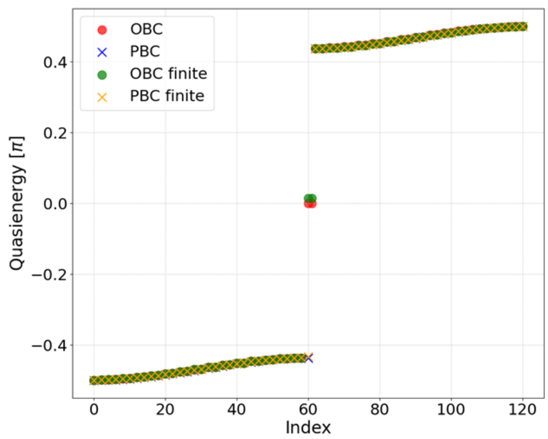

(a) Quasienergy spectrum of the resonant DKRS with parameters $n_{max} = 30$, $\tau_{p,1/2} = 10^{-2}$, $k_1 = 0.5\pi$ and $k_2 = 0.5\pi$.
We plot only every second quasienergy. Still, all "deviating" quasienergies are shown. We see two edge states for open BCs (each under infinitesimal and finite kicking).

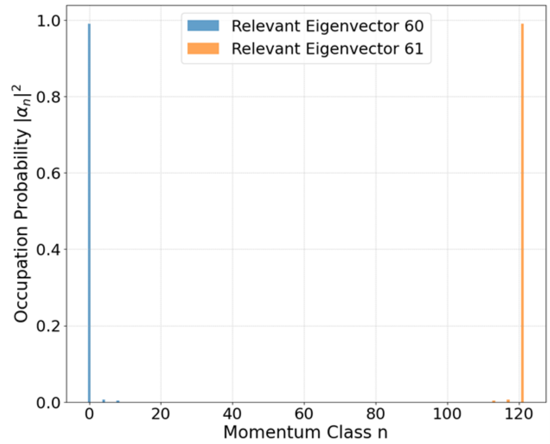

(b) Occupation probability distribution $|\alpha_n|^2$ against the momentum classes n for OBCs with infinitesimal kicking.

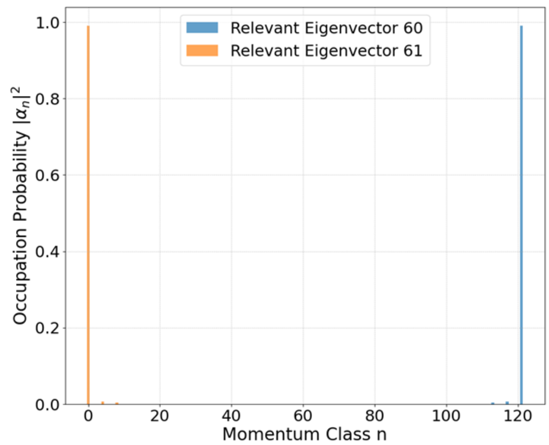

(c) Occupation probability distribution $|\alpha_n|^2$ against the momenta classes n for OBCs with finite kicking of duration $\tau_p = 10^{-2}$.

Figure 32: Investigation of the eigenvectors of the resonant DKRS. Parameters: $n_{max} = 30$, $\tau_{p,1/2} = 10^{-2}$, $k_1 = 0.5\pi$ and $k_2 = 0.5\pi$.
Here, we can see a very strong localization at the edge of the momenta basis. We can also see nicely, that under OBCs, the localization is not symmetric because of the underlying structure of the boundary conditions.

For a kicking strength of $k_2 = 2.5\pi$, there arise more edge states, as we would expect by the bulk-edge correspondence. Here, we can again show that the eigenvectors corresponding to those edge states localize at the edge of the momentum basis. Under finite kicking ($\tau_p = 10^{-2}$) and PBCs, there are four quasienergies that differ from the overall band structure. Figure 33d shows that those states are also localizing at the edge of the numerical box.

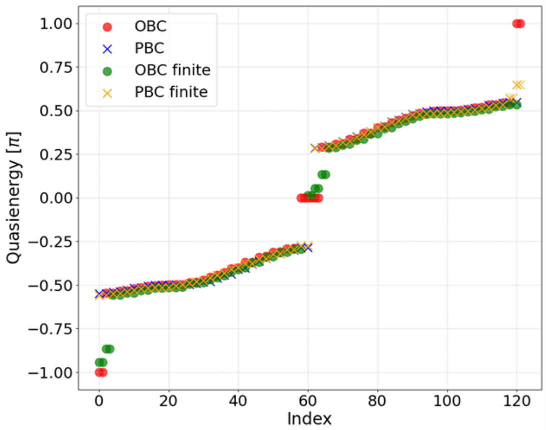

(a) Quasienergy spectrum of the resonant DKRS with parameters $n_{max} = 30$, $\tau_{p,1/2} = 10^{-2}$, $k_1 = 0.5\pi$ and $k_2 = 2.5\pi$.
We plot only every second quasienergy. Still, all "deviating" quasienergies are shown. We see ten edge states for open BCs (each under infinitesimal and finite kicking). For the combination of a finite kicking duration and PBCs, there are four quasienergies that take slightly different values than expected by the overall band structure.

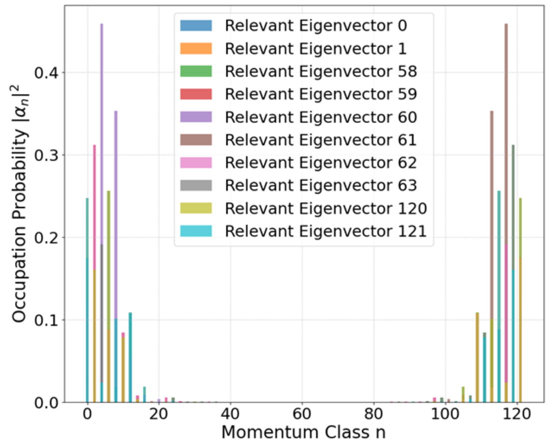

(b) Occupation probability distribution $|\alpha_n|^2$ against the momentum classes n for OBCs with infinitesimal kicking.

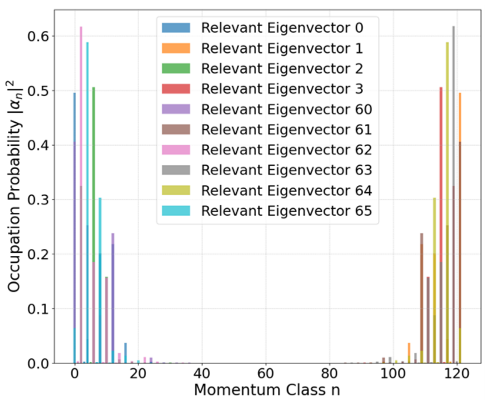

(c) Occupation probability distribution $|\alpha_n|^2$ against the momentum classes n for OBCs with finite kicking of $\tau_p = 10^{-2}$.

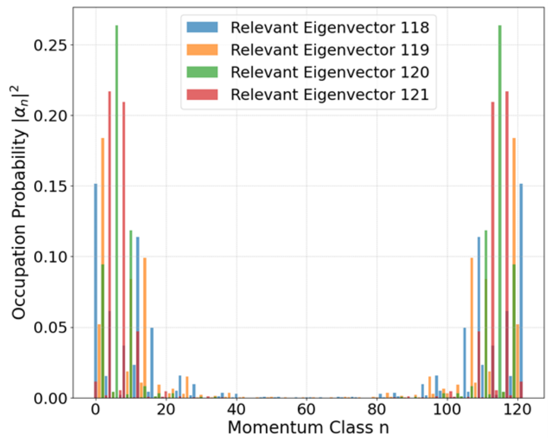

(d) Occupation probability distribution $|\alpha_n|^2$ against the momentum classes n for PBCs with finite kicking of duration $\tau_p = 10^{-2}$.

Figure 33: Investigation of the eigenvectors of the resonant DKRS. Parameters: $n_{max} = 30$, $\tau_{p,1/2} = 10^{-2}$, $k_1 = 0.5\pi$ and $k_2 = 2.5\pi$.
Again, all eigenvectors localize around the edge of the numerical box. Only for the combination of finite kicking duration and periodic boundary conditions, the occupation probability distribution compared to the case of OBCs. However, the corresponding quasienergies also do not differ that strongly from the expected structure in the case of PBC than for the OBC case.

C.4 Spectra against the Kicking Strength k_2 for a Free-Time Evolution over τ

For the DKRS, we again also studied the Floquet spectra for a free-time evolution over τ_i instead of $\tau_i - \tau_{p,i}$ (with $i = 1, 2$ corresponding to the kicks of strength k_1 and k_2, respectively).
Examining the spectra showed, in accordance to the QKR, that the quasienergy bands acquired curvature. The MCD did not change noteworthy under the change of the time period for the free-time evolution.
For the sake of completeness, we now want to show the quasienergy spectra against the kicking strength k_2 for the adjusted free-time evolution as well. However, the structures are cluttered in a way that we

cannot really draw conclusions from the figures.

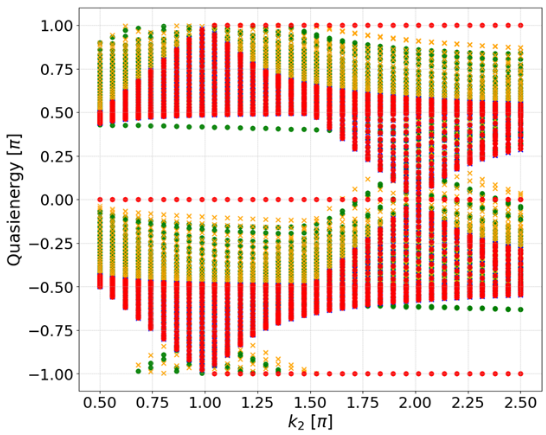

(a) Quasienergy spectrum against kicking strength k_2. The spectra under infinitesimal kicking stay the same, as expected. For a finite kicking duration of $\tau_{p,i} = 10^{-3}$, the degeneracy of the quasienergies at a kicking strength k_2 seems to be lifted: for each k_2, there a several different quasienergies.

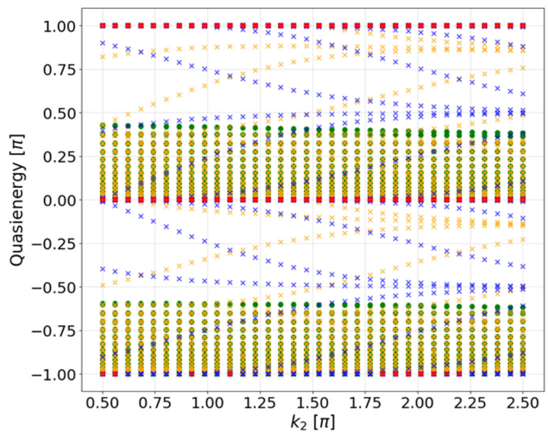

(b) Quasienergy spectrum against kicking strength k_2. Again, the spectra under infinitesimal kicking duration stay the same. The finite kicking duration $\tau_{p,i} = 10^{-3}$ leads to the reversal of the degeneracy of the quasienergies here as well.

Figure 34: Floquet spectra of the DKRS under a free-time evolution over τ_i against the kicking strength k_2. The chosen parameters are $n_{max} = 30$, $\tau_{p,i} = 10^{-3}$, $k_1 = 0.5\pi$. The color code follows that in Fig.s 19a and 20a.

The quasienergy spectra of the infinitesimally shortly kicked DKRS stay the same, as expected. The effect of the finite kicking duration in this regime seems to be the reversal of the degeneracy of the quasienergies.

D Project Work

In this thesis, we use our knowledge on the emergence of soft walls by finite kicking durations and their position in momentum space. The following excerpt summarizes the most important methods and insights of the project work (in German).

D.1 Grenzen im Phasenraum

Endliche Pulsdauern haben zur Folge, dass die Welle im Impulsraum reflektiert wird. Dieser Effekt ist rein klassisch und sorgt dafür, dass im Phasenraum "Impulsbarrieren" entstehen, die von der Welle nur im quantenmechanischen Bild durch Tunneln überwunden werden können.
Großer Teil des Projektpraktikums war es, die Lage dieser Impulsbarrieren zu bestimmen und untersuchen. Die verschiedenen verwendeten Ansätze werden im Folgenden erläutert.
Es ist zu beachten, dass die für Methoden 1 und 2 verwendete Formel (69) allein für den Fall $\tau = 4\pi$ Gültigkeit hat. Daher werden alle folgenden Rechnungen für Parameter $k = 1$ und $\tau = 4\pi$ durchgeführt.

D.1.1 Methoden der Bestimmung

Methode 1: Lage der Maxima der Wahrscheinlichkeitsverteilung Der erste Ansatz besteht darin, die Lage der Maxima der Wahrscheinlichkeitsverteilungen und ihre Abhängigkeit von der Kickanzahl t zu bestimmen. Theoretisch sollten sie folgender Relation folgen:

$$p_{max} \sim t \cdot k \cdot \frac{\pi}{2} \tag{69}$$

Diese Formel entnehmen wir dem Artikel *Nonlinearity* [2]. Diese Relation ist nur gültig für den Fall $\tau = 4\pi$. Langfristig möchten wir eine entsprechende Formel für andere Werte von τ finden. Diese lassen sich dann nicht mehr analytisch bestimmen, jedoch sollten sich Proportionalitäten aus numerischen Simulationen finden lassen.
Wir plotten die numerisch bestimmten p_{max} gegen den theoretischen Verlauf. Das t, bei dem die experimentellen Daten nicht mehr der theoretischen Vorhersage folgen, nutzen wir dann, um mithilfe der Formel p_L zu bestimmen. Als Proportionalitätsfaktor hat sich $a = 0.6$ als passend herausgestellt: $p_L \approx 0.6 \cdot t \cdot k \cdot \frac{\pi}{2}$.

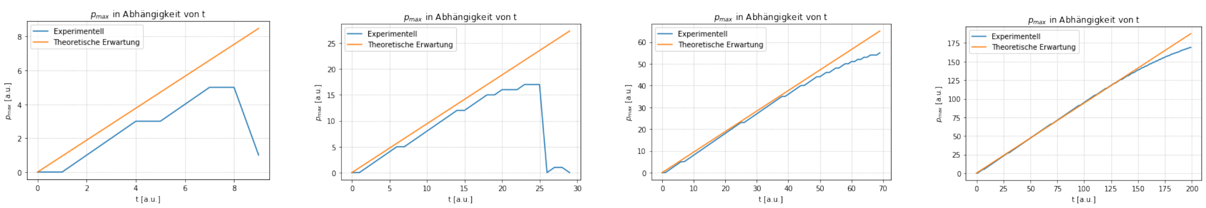

(a) $\tau_{pulse} = 10^{-1}$ (b) $\tau_{pulse} = 10^{-2}$ (c) $\tau_{pulse} = 10^{-3}$ (d) $\tau_{pulse} = 10^{-4}$

Figure 35: Bestimmung von p_L mithilfe der Plots p_{max} gegen t

Methode 2: Abweichung Energie - Idealkurve Die nächste Methode besteht darin, den idealen Verlauf der Energie nach Gl. (18) zu plotten. Dazu wird die numerisch ermittelte Energie $E(t)$ geplottet. Wir bestimmen dann das t, bei dem die Kurven beginnen, signifikant voneinander abzuweichen. Als Threshold für diese Abweichung verwenden wir eine Differenz der Werte von Idealkurve und numerischen Ergebnissen von $\frac{1}{50}$-tel der idealen Energie. Aus dem so bestimmten t_k lässt sich mithilfe der Formel (69) dann das maximale p bestimmen.

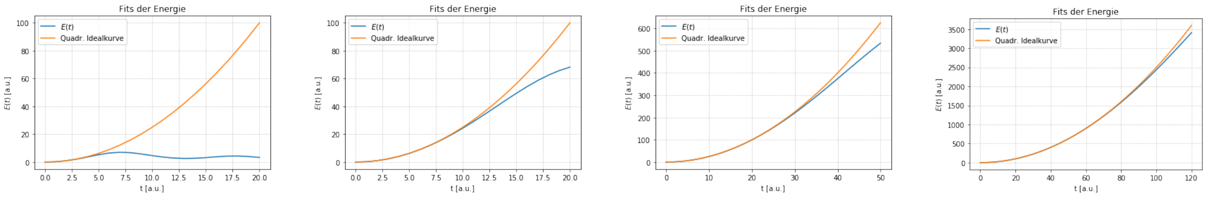

(a) $\tau_{pulse} = 10^{-1}$ (b) $\tau_{pulse} = 10^{-2}$ (c) $\tau_{pulse} = 10^{-3}$ (d) $\tau_{pulse} = 10^{-4}$

Figure 36: Bestimmung von p_L aus Abweichung der Energie $E(t)$ von der Idealkurve

Methode 3: Summierung über die Wahrscheinlichkeitsverteilung Ein erster Ansatz ist es, über die Wahrscheinlichkeitsverteilung zu summieren. Hier wird symmetrisch um $p = 0$ je ein Schritt in p-Richtung nach links und rechts (negative und positive Impulsklassen) gegangen und die zugehörige Wahrscheinlichkeit summiert. Der Gedanke ist hier, so lange die Wahrscheinlichkeiten auf zu summieren, bis eine gewisse Threshold-Wahrscheinlichkeit erreicht ist. Wir wählen hier einen Threshold von 99% der maximalen Wahrscheinlichkeit (also 0.99). Wird diese Schwelle erreicht, lässt man sich die letzte Impulsklasse p ausgeben, für die eine Wahrscheinlichkeit addiert wird. Anschaulich schaut man sich also an, bei welchem Impuls p 99% der Wahrscheinlichkeit erreicht wurde, das gekickte Teilchen im Bereich der Impulse $[-p, p]$ zu finden. Des Weiteren ist hier zu beachten, dass wir für jede Anzahl an Kicks t eine eigene Wahrscheinlichkeitsverteilung erhalten. Das bedeutet, dass bei festem p über alle $|\psi(p,t)|$ bei diesem p summiert werden muss und wir über t mitteln:

$$|\psi|^2_{sum} = \sum_{p,t} \frac{1}{t} \cdot |\psi(p,t)|^2 \tag{70}$$

Methode 4: Summe bis Energiemaximum Ganz analog zum Summieren über die Wahrscheinlichkeitsverteilung kann auch über die Energie summiert werden:

$$\bar{E} = \sum_{p} \frac{p^2}{2} |\psi_p|^2 \tag{71}$$

Die Idee ist hier dieselbe wie bei Methode 3 (Par. D.1.1), dass die Impulsklasse p, die die gekickten Teilchen erreichen können, bestimmt wird, bis die Energie bereits maximiert wird. Man trifft also die Annahme, dass die Impulsklassen oberhalb dieses p nicht mehr signifikant zur Energie beitragen, und daher die Teilchen bei p reflektiert worden sein müssen.
Wir mitteln hier nicht über die unterschiedlichen t, sondern bestimmen das Maximum der Energie und das zugehörige t_{max}, bei dem dieses Energiemaximum erreicht wird. Für t_{max} wird die Summe schließlich ausgewertet. Die Summe wird abgebrochen, sobald die Maximalenergie (minus ein kleiner Threshold) erreicht ist. Wir wählen als Threshold ein Hundertstel der Maximalenergie: $thresh. = \frac{1}{100} E_{max}$

Methode 5: k_{eff} Die Einführung der endlichen Pulsdauer kann auch so verstanden werden, dass mit steigendem Impuls p die Kickstärke k abnimmt. Wir definieren dann eine effektive Kickstärke k_{eff}, für die gilt

$$k_{eff} = k_{max} \cdot \frac{sin(\frac{p \cdot \tau_{pulse}}{2})}{\frac{p \cdot \tau_{pulse}}{2}} \tag{72}$$

Der Ansatz zur Bestimmung von p_L aus diesem k_{eff} besteht darin, dass wir das t_k bestimmen, bei dem die Energie von dem Idealverlauf signifikant abweicht. Dann fitten wir ab diesem t_k an die numerisch bestimmte Energie eine quadratische Kurve. Wir sagen also, dass wir erwarten, dass die Energie immer noch einen quadratischen Verlauf hat, wie in Gl. (18), jedoch jetzt statt mit k mit einem k_{eff}. Dieses k_{eff} lassen wir uns als Fit-Parameter der Kurve ausgeben.

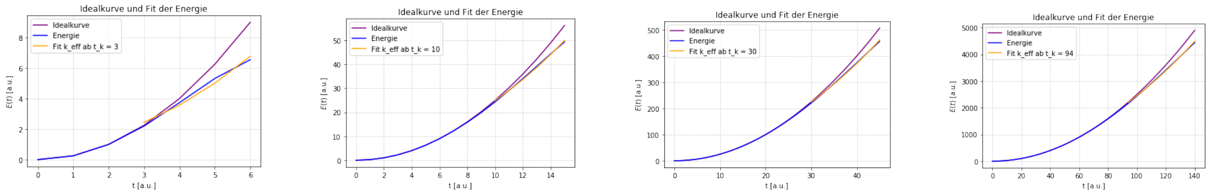

(a) $\tau_{pulse} = 10^{-1}$ (b) $\tau_{pulse} = 10^{-2}$ (c) $\tau_{pulse} = 10^{-3}$ (d) $\tau_{pulse} = 10^{-4}$

Figure 37: Bestimmung von k_{eff} mithilfe der Energieerwartung

Wir erhalten die folgenden k_{eff}:

Table 2: k_{eff} aus numerischer Bestimmung

τ_{pulse}	t_k	k_{eff}
10^{-1}	3	0.8
10^{-2}	10	0.896
10^{-3}	30	0.917
10^{-4}	94	0.922

Um nun aus diesen k_{eff} die p_L zu bestimmen, plotten wir den erwarteten Verlauf von k_{eff} (vgl. Gl. (72)) gegen den Impuls p. Der Impuls, bei dem das zuvor bestimmte k_{eff} erreicht wird, entspricht dann dem gesuchten p_L:

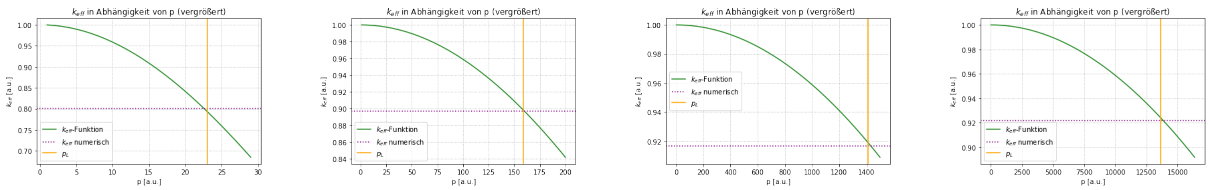

(a) $\tau_{pulse} = 10^{-1}$ (b) $\tau_{pulse} = 10^{-2}$ (c) $\tau_{pulse} = 10^{-3}$ (d) $\tau_{pulse} = 10^{-4}$

Figure 38: Bestimmung von p_L mithilfe von k_{eff}

D.1.2 Ergebnisse der p_L-Bestimmung & Diskussion der Methoden

Die Ergebnisse der Bestimmung der Impulsbarrieren p_L unter Anwendung der vorgestellten Methoden sind in der folgenden Tabelle zusammengefasst:

Table 3: p_L unter Bestimmung durch Methoden 1 bis 5

Methode	τ_{pulse}			
	10^{-1}	10^{-2}	10^{-3}	10^{-4}
1	5	16	48	150
2	3	9	28	89
3	5	18	59	193
4	6	19	59	184
5	23	159	1410	13648

Der Fehler der p_L ist i.A. auf max. 20% des bestimmten Wertes einzuschätzen. Zu diesem Fehler komme ich aufgrund der Betrachtung meiner Ergebnisse, wenn ich die aus eigener Einschätzung geschätzte Abweichung (Methoden 1 (Par. D.1.1) und 2 (Par. D.1.1)) oder gewählte Thresholds (Methoden 3 (Par. D.1.1) und 4 (Par. D.1.1)) leicht ändere und die Ergebnisse vergleiche.

References

[1] F. M. Izrailev. "Simple models of quantum chaos: Spectrum and eigenfunctions". In: *Phys. Rep. 196, 299* (1990). DOI: https://doi.org/10.1016/0370-1573(90)90067-C.

[2] S. Wimberger, I. Guarneri, and S. Fishman. "Quantum resonances and decoherence for δ-kicked atoms". In: *Nonlinearity 16, 1381* (2003). URL: https://iopscience.iop.org/article/10.1088/0951-7715/16/4/312/pdf.

[3] B. V. Chirikov, F. M. Izrailev, and D. L. Shepelyansky. "Quantum Chaos: Localization vs. Ergodicity". In: *Physica D 33, 77-88* (1988). DOI: https://doi.org/10.1016/S0167-2789(98)90011-2.

[4] M. Delvecchio, F. Petiziol, and S. Wimberger. "Resonant Quantum Kicked Rotor as A Continuous-Time Quantum Walk". In: *Condens. Matter, 5(1), 4* (2020). DOI: https://doi.org/10.3390/condmat5010004.

[5] J. Gong L. Zhou. "Floquet topological phases in a spin-1/2 double kicked rotor". In: *Phys. Rev. A 97, 063603* (2018). DOI: https://doi.org/10.1103/PhysRevA.97.063603.

[6] R. Blümel, S. Fishman, and U. Smilansky. "Excitation of molecular rotation by periodic microwave pulses. A testing ground for Anderson localization". In: *J. Chem. Phys. 84, 2604–2614* (1986). DOI: https://doi.org/10.1063/1.450330.

[7] M. S. Santhanam, S. Paul, and J. B. Kannan. "Quantum kicked rotor and its variants: Chaos, localization and beyond". In: *Physics Report 956, 1–87* (2022). DOI: https://doi.org/10.1016/j.physrep.2022.01.002.

[8] J. Gong D. Y. H. Ho. "Topological effects in chiral symmetric driven systems". In: *Phys. Rev. B 90, 195419* (2014). DOI: http://dx.doi.org/10.1103/PhysRevB.90.195419.

[9] J. Gong L. Zhou. "Recipe for creating an arbitrary number of Floquet chiral edge states". In: *Phys. Rev. B 97, 245430* (2018). DOI: https://doi.org/10.1103/PhysRevB.97.245430.

[10] S. Kitamura T. Oka. "Floquet Engineering of Quantum Materials". In: *Annu. Rev. Condens. Matter Phys. 10, 387* (2019). DOI: https://doi.org/10.1146/annurev-conmatphys-031218-013423.

[11] A. Eckardt. "Colloquium: Atomic quantum gases in periodically driven optical lattices". In: *Rev. Mod. Phys. 89.011004* (2017). DOI: http://dx.doi.org/10.1103/RevModPhys.89.011004.

[12] S. Wimberger. "Chaos and Localisation: Quantum Transport in Periodically Driven Atomic Systems". PhD thesis. LMU München: Fakultät für Physik, (2003). URL: http://nbn-resolving.de/urn:nbn:de:bvb:19-16877.

[13] A. Wagner. "Topology in 1D quantum walks". Bachelor Thesis. University of Heidelberg, (2018). URL: https://www.thphys.uni-heidelberg.de/~wimberger/ba_wagner.pdf.

[14] N. Bolik. "Topological phases and symmetries in 1D quantum walks". Bachelor Thesis. University of Heidelberg, (2022). URL: https://www.thphys.uni-heidelberg.de/~wimberger/ba_bolik.pdf.

[15] T. Kitagawa. "Topological phenomena in quantum walks: elementary introduction to the physics of topological phases". In: *Phys. Rev. A 82, 033429* (2018). DOI: https://doi.org/10.1103/PhysRevA.82.033429.

[16] S. Wimberger G. Summy. "Quantum random walk of a Bose-Einstein condensate in momentum space". In: *Phys. Rev. A 93, 023638* (2016). DOI: http://dx.doi.org/10.1103/PhysRevA.93.023638.

[17] S. Dadras et al. "Quantum Walk in Momentum Space with a Bose-Einstein Condensate". In: *Phys. Rev. Lett. 121, 070402* (2018). DOI: https://doi.org/10.1103/PhysRevLett.121.070402.

[18] J. Gong J. Wang. “Proposal of a cold-atom realization of quantum maps with Hofstadter’s butterfly spectrum”. In: *Phys. Rev. A 77, 031405(R)* (2008). DOI: http://dx.doi.org/10.1103/PhysRevA.77.031405.

[19] S. Wimberger N. Bolik. “Spontaneous-emission-induced ratchet in atom-optics kicked-rotor quantum walks”. In: *Phys. Rev. A 109, 063307* (2024). DOI: https://doi.org/10.1103/PhysRevA.109.063307.

[20] NumPy Developers. *NumPy Documentation: np.linalg.eig.* © Copyright 2008-2024, NumPy Developers. (2024). URL: https://numpy.org/doc/stable/reference/generated/numpy.linalg.eig.html (visited on 02/13/2025).

[21] SciPy Developers. *SciPy Documentation: sp.expm.* URL: https://docs.scipy.org/doc/scipy/reference/generated/scipy.linalg.expm.html (visited on 02/13/2025).

[22] S. W. Smith. *The Scientist and Engineer’s Guide to Digital Signal Processing.* Copyright © 1997-2011. California Technical Publishing, (2011). URL: https://www.dspguide.com/.

[23] A. Akhmerov et al. *Topology in Condensed Matter: Tying Quantum Knots.* By Topology course team, CC-BY-SA 4.0 (materials) & BSD (code). (2021). URL: https://topocondmat.org/index.html# (visited on 02/13/2025).

[24] R. Shinsei et al. “opological insulators and superconductors: tenfold way and dimensional hierarchy”. In: *New J. Phys. 12, 065010* (2010). DOI: https://doi.org/10.1088/1367-2630/12/6/065010.

[25] J. K. Asbóth, L. Oroszlány, and A. Pályi. “A Short Course on Topological Insulators”. In: *Lecture Notes in Physics, volume 919.* Springer, (2016).

[26] J. Shapiro. “The Bulk-Edge Correspondence in Three Simple Cases”. In: *Reviews in Mathematical Physics, Vol. 32, No. 03, 2030003* (2020). URL: https://arxiv.org/pdf/1710.10649.

[27] F. Cardano, A. D’Errico, A. Dauphin, et al. “Detection of Zakk phases and topological invariants in a chiral quantum walk of twisted photons”. In: *Nat. Commun. 8, 15516* (2017). DOI: https://doi.org/10.1038/ncomms15516.

[28] H. Obuse J. Asbóth. “Bulk-boundary correspondence for chiral symmetric quantum walks”. In: *Phys. Rev. B 88, 121406(R)* (2013). DOI: https://doi.org/10.1103/PhysRevB.88.121406.

[29] I. Sh. Averbukh J. Floß. “Edge states of periodically kicked quantum rotors”. In: *Phys. Rev. E 91, 052911* (2015). DOI: http://dx.doi.org/10.1103/PhysRevE.91.052911.

[30] V. Karle, A. Ghazaryan, and M. Lemeshko. “Topological Charges of Periodically Kicked Molecules”. In: *Phys. Rev. Lett. 130, 103202* (2023). DOI: https://doi.org/10.1103/PhysRevLett.130.103202.

[31] C. R. Harris et al. “Array programming with NumPy”. In: *Springer Science and Business Media LLC, Nature 585.7825* (2020). DOI: https://doi.org/10.1038/s41586-020-2649-2.

[32] P. Virtanen et al. “SciPy 1.0: Fundamental Algorithms for Scientific Computing in Python”. In: *Nature Methods* (2017). DOI: https://doi.org/10.1038/s41592-019-0686-2.

[33] J. D. Hunter. “Matplotlib: A 2D Graphics Environment”. In: *Computing in Science & Engineering 9.3* (2007). DOI: https://doi.org/10.1109/MCSE.2007.55.

Tools and Methods

- Python, using numpy [31], scipy [32] and matplotlib [33] among other libraries to determine the spectra and generate the plots in this thesis
- ChatGPT for researching plot settings in Python
- LaTeXfor PDF typesetting

Erklärung

Ich versichere, dass ich diese Arbeit selbstständig verfasst und keine anderen als die angegebenen Quellen und Hilfsmittel benutzt habe.

Heidelberg, den 20. Februar 2025,